Nonlinear Photonic Devices With Subwavelength Dimensions

by

Brian Adam Daniel

Submitted in Partial Fulfillment of the
Requirements for the Degree
Doctor of Philosophy

Supervised by

Govind P. Agrawal

The Institute of Optics
Arts, Sciences, and Engineering
Edmund A. Hajim School of Engineering and Applied Sciences
University of Rochester
Rochester, New York

2012

Curriculum Vitae

The author was born in Escondido, California in 1983. In 2007 he graduated from the University of California, San Diego with a B.S. in Engineering Physics. In the Fall of 2007 he enrolled in the Ph.D. program at the Institute of Optics. In the Summer of 2008 he joined the research group of Professor Govind Agrawal, where he has carried out his doctoral research on nonlinear photonic devices.

Publications

Brian A. Daniel and Govind P. Agrawal, "Dependence of dispersive and birefringence properties of silicon nanowires on waveguide dimensions," Opt. Lett. 35, 190-192 (2010)

Brian A. Daniel and Govind P. Agrawal, "Vectorial nonlinear propagation in silicon nanowire waveguides: polarization effects," J. Opt. Soc. Am. B 27, 956-965 (2010)

Brian A. Daniel, Drew N. Maywar, and Govind P. Agrawal, "Dynamic mode theory of optical resonators undergoing refractive index changes," J. Opt. Soc. Am. B 28, 2207-2215 (2011)

Brian A. Daniel, Drew N. Maywar, and Govind P. Agrawal, "Efficient adiabatic wavelength conversion in Gires–Tournois resonators," Opt. Lett. 36, 4155-4157 (2011)

Brian A. Daniel, Jonathan Y. Lee, Philippe M. Fauchet, and Govind P. Agrawal, "Observation of spectral and temporal polarization oscillations of optical pulses in a silicon nanowaveguide," Appl. Phys. Lett. 99, 201104 (2011)

Brian A. Daniel and Govind P. Agrawal, "Phase-switched all-optical flip-flops using two-input bistable resonators," IEEE Photon. Technol. Lett. 24, 479-481 (2012)

Acknowledgments

A number of people have contributed to making this thesis possible. Foremost among them is my adviser, Govind Agrawal. The development of my understanding of the field of photonics has come largely through him; through the discussions I've had with him, the books that he's written, and the courses I've taken with him. He has also been the strongest supporter of my research and that has given me heart in carrying it out. His advice has greatly improved the quality of my work and this thesis would not have been possible without him.

I'm also grateful to the members of my research group. Lianghong Yin helped me get oriented in the lab during my first Summer, and that proved very helpful when I began doing experiments on my own after she had graduated. I've learned a lot from Prashant Baveja about optical communications, and have had fruitful discussions with Yuzhe Xiao about optical resonators and wavelength conversion that contributed to my work in those areas. A number of visitors and postdocs have come through our group while I've been here, and have been good company as well as contributors to many insightful discussions that have helped shape my thinking. These include Sami Mumtaz, Arijit Bose, Néstor Crisóstomo, Laurentius (Oscar) Osapoetra, Alexandre Baron, and Hojoon Lee.

Professor Drew Maywar of the Rochester Institute of Technology gave me valuable feedback about my work on wavelength conversion in resonators that led to notable improvements in its quality.

A number of research groups and students enabled my experimental work by lending equipment. Foremost among them is Professor Fauchet's group. Jonathan Lee in particular was very helpful and I would not have been able to complete the

experiments on silicon waveguides without him lending and assisting with the necessary equipment. Yuhong Yao from Professor Knox's lab, as well as Haomin Yao and Jordan Leidner from Professor Marciante's, lent important pieces of equipment for extended periods of time during my experimental effort. A number of Professor Boyd's students also helped me in this way several times.

The quality of teaching at the Institute is exceptional in my opinion and I'm grateful to the Professors that I studied under for illuminating the field of optics for me. All of the staff have done an excellent job keeping the department running, and the work of Lissa Cotter in particular contributed to this thesis by helping with all of my paperwork and making sure that I kept receiving paychecks.

I'm grateful to the good taxpayers of this country for funding my research through the National Science Foundation, and to my adviser for securing that funding for me.

Avoiding starvation and freezing to death were both crucial to the completion of this thesis, and Jordan Leidner helped prevent them both by giving me rides to the grocery store and to school during my first year when I didn't have a car. In addition to Jordan, a number of other people have blessed me with their friendship over the course of my time here and I'm grateful to you all. Completing this thesis would have been much more difficult without you.

I'm grateful to my parents and my sisters for their love. My trips to visit them in San Diego have been the refreshment of my soul. This thesis would not have been realized without the support they've given me throughout my life.

Finally, more than anyone else, this thesis was enabled by Jesus Christ. Through Him the world was made such that it could be understood, and His love and grace have sustained me these past several years.

Abstract

A pair of synthetic methods are presented for describing nonlinear optical phenomena in photonic devices of any size scale and with any degree of refractive-index contrast.

The first method is a general description of nonlinear phenomena in guided-wave devices. By retaining all of the cartesian components of the field implicit assumptions about device dimensions and refractive-index contrast are not made. The method is applied to the study of nonlinear optical phenomena in silicon-on-insulator (SOI) waveguides. Contributions are found to the nonlinear propagation parameters that do not appear in traditional descriptions of nonlinear fiber optics, and are found to become significant as a result of the high index contrast of the SOI material system when device dimensions enter the subwavelength regime. An experimental study of nonlinear polarization effects in SOI waveguides is presented and the theoretical model is used to explain them.

The second method is a general description of nonlinear phenomena in optical resonators. The method makes no assumptions about device dimensions, refractive-index contrast, or the specific cavity structure. It is applied to understanding two different phenomena in resonators and to designing two different devices based on these phenomena. The first phenomenon is the influence of a dynamic refractive-index change on the optical field in a resonator. The resulting frequency shift of the field is proposed as a possible mechanism for implementing a wavelength conversion device, and device design criteria and theoretical performance capabilities are presented. The second phenomenon is the influence of the cross-phase modulation interaction of two resonator modes that results from the Kerr effect. The resulting bistability is proposed as a possible mechanism for implementing a phase-switched optical memory device, and device design criteria and theoretical performance capabilities are presented.

Table of Contents

List of Tables

List of Figures

Foreword

The work presented in this thesis benefited from the advice and assistance of several people, but is solely that of the author. The exception is the fabrication of the silicon waveguides used in the experiments of chapter 4, which was not performed by the author but by his collaborator.

1 Introduction

1.1 Historical overview

The field of photonics is concerned with using light for the transmission of information [1]. It became a major area of technological development with the advent of low-loss optical fiber, which was foreseen by Charles Kao and George Hockham in 1966 [2] and later demonstrated by researchers at Corning in 1970 [3]. Low-loss optical fiber offers a unique opportunity: the spatial confinement of light over long propagation distances. Today that advantage allows it to be used as the backbone of the global telecommunication network, which connects over 2 billion internet users and almost 6 billion mobile phones [4].

When light is confined to small spatial dimensions its intensity is enhanced. As a result propagation effects that depend on the intensity of the field (i.e. nonlinear effects) are also enhanced. This was realized early on in the field of fiber optics. Some of the first low-loss Corning fibers were employed by researchers at Bell Laboratories to demonstrate a wide variety of nonlinear optical effects, beginning with Raman amplification in 1972 [5]. Later work by this same group, led by Roger Stolen, demonstrated stimulated Brillouin scattering [6], parametric amplification [7], self-phase modulation [8] and the formation of optical solitons [9]. Thus the invention of low-loss optical fiber not only catalyzed the field of photonics as a whole, but also gave birth to the field of nonlinear photonics. As fiber optics has developed over the last 40 years, nonlinear effects have presented both a challenge and an opportunity. They pose a challenge because they can impair the transmission of a signal over long

distances. On the other hand, the zoo of nonlinear effects introduced by the third-order nonlinearity in silica alone has led to a wide variety of ideas for devices that perform ultrafast signal processing in the optical domain (not to mention applications in other fields) [10].

Even before the realization of optical fibers there existed the idea of creating optical circuits integrated on a single chip [11]. Since that time the field of integrated photonics has not grown as rapidly as the field of fiber optics, but it has grown steadily. Demand for integrated photonic circuits as signal processing devices in fiber communication networks, as well as for high-bandwidth communication in electronic microprocessors, has led to widespread development of such circuits in a number of different material systems. Photonic integrated circuits in indium phosphide and silica-on-silicon, as examples, are regularly manufactured and sold for use in contemporary communications systems [12, 13].

The silicon-on-insulator (SOI) material system is particularly promising for the implementation of photonic integrated circuits for two reasons. First, the infrastructure that has been developed for the microelectronics industry can readily be applied to the production of low-cost SOI-based photonic circuits. Second, such photonic circuits can be readily integrated with their electronic counterparts. Early work on silicon photonics was performed in the 1980s [14, 15] and since then the field has steadily gained momentum. In the last decade or so this steady research momentum has turned into a veritable avalanche as major players in the microprocessor industry such as Intel and IBM have taken up silicon photonics with vigor [16, 17].

One of the trends that can be observed in the field of integrated photonics in general, and silicon photonics in particular, is device miniaturization. The cross-sectional area of silicon waveguides used in experiments has gone from ~70 μm^2 to as small as 0.1 μm^2 [14, 18]. The resulting enhancement in intensity, as well as a large Kerr coefficient, have made nonlinear effects in silicon easily observable. A significant component of the research in silicon photonics over the last decade has been devoted to studying these nonlinear effects. These studies began in 2002 with the observation of self-phase modulation by a research group at the Chinese University of Hong Kong [19]. Soon after this Bahram Jalali's group at the University of California, Los Angeles demonstrated Raman amplification and lasing [20, 77], and a group working

at NTT in Japan reported the first observation of four-wave mixing [22]. These initial observations were followed by a torrent of theoretical and experimental studies of these effects as well as their potential applications for signal processing (see Refs. [23] and [24] for reviews of this work). One of the dominant themes in this body of research is the difficulty of leveraging nonlinear effects in silicon for practical application as a result of nonlinear losses from two-photon and free-carrier absorption mechanisms. A more recent trend explores alternative SOI-compatible materials such as silicon-polymer hybrid systems [25] and silicon nitride [26–28]. Thus the field of nonlinear photonics has grown to be concerned not only with effects that are observable in optical fibers, but in various kinds of integrated photonic circuits as well.

1.2 Theoretical methods

As the field of nonlinear photonics has grown to be concerned with a wider variety of material systems in increasingly smaller devices, the theoretical methodologies used in the field have evolved in concert. The majority of theoretical work is based on the nonlinear Schrödinger equation. The traditional approach to the nonlinear Schrödinger equation, which was developed for understanding nonlinear effects in silica fibers, is based on a number of simplifying assumptions [29]. These assumptions include the slowly-varying envelope approximation, the existence of only the fundamental spatial mode, and the scalar approximation. This last approximation can be understood by considering the nature of optical modes in a dielectric waveguide. Mathematically, the electric field of a mode can be written as

$$\mathbf{E}\left(x,y,z,t\right) = \mathbf{e}\left(x,y\right) e^{i(\beta z - \omega_0 t)} + \text{c.c.}, \tag{1.1}$$

where ω_0 is the optical frequency, β is the mode's wavevector, and c.c. denotes the complex conjugate. The spatial profile of the mode is described by the function $\mathbf{e}(x,y)$ which can have nonzero e_x, e_y and e_z components. The scalar approximation assumes the field is dominated by a single transverse cartesian component (for example the e_x component) so that it can be written in the form

$$\mathbf{e}\left(x,y\right) \approx \hat{\mathbf{x}} e_x. \tag{1.2}$$

It is the inapplicability of this scalar approximation to specific material systems that has served as the main impetus for revisiting the traditional approach to the nonlinear Schrödinger equation in the last decade.

The significance of a waveguide mode's longitudinal field component (e_z) depends primarily on two things: the size of the waveguide and the magnitude of the refractive-index contrast in the material system out of which it is made. Consider the well-known solutions for the fundamental modes of the infinite planar slab depicted in Fig. 1.1(b) [30, 31]. The transverse electric (TE) mode is entirely transverse so that e_z is identically zero everywhere. The vectorial composition of the transverse magnetic (TM) mode, by contrast, is highly sensitive to the waveguide height h. This is illustrated in Fig. 1.1(a) where the fractional composition of the TM mode that is longitudinal (f_z) versus waveguide height is shown for various material systems. The fraction f_z is defined as

$$f_z = \frac{\int_{-\infty}^{\infty} |e_z|^2 \, dy}{\int_{-\infty}^{\infty} |e_x|^2 + |e_y|^2 + |e_z|^2 \, dy}. \tag{1.3}$$

From Fig. 1.1(a) two insights can be drawn. First, the longitudinal field component is

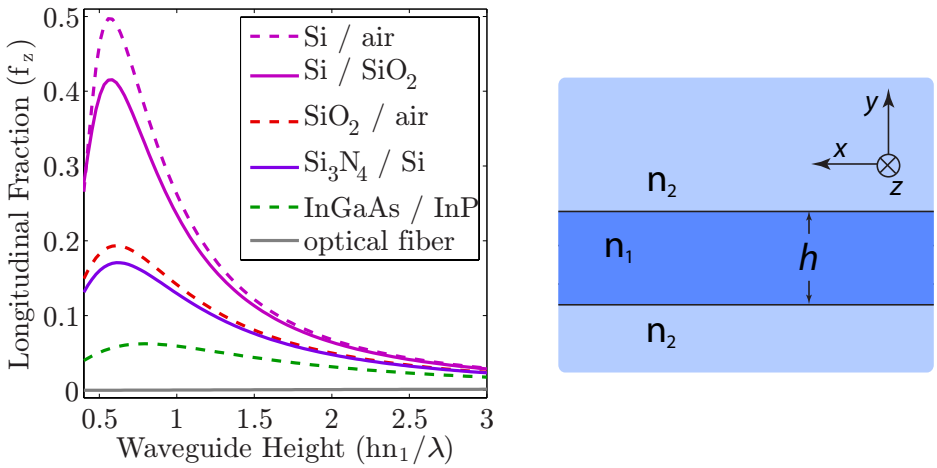

(a) (b)

Figure 1.1: (a) Fraction of the waveguide mode in the longitudinal (e_z) field component when various materials are used for the core/cladding; (b) schematic of the planar waveguide structure under consideration. n_1 and n_2 are the core and cladding refractive indices, respectively. See table 1.2 for the parameter values used in (a).

	n_1	n_2
Si / air	3.48	1
Si / SiO_2	3.48	1.44
SiO_2 / air	1.44	1
Si_3N_4 / SiO_2	1.99	1.44
InGaAs / InP	3.6	3.17
optical fiber	1.45	1.445

Table 1.1: Core/cladding refractive indices used for the calculation in Fig. 1.2. Values are taken at the 1.55 μm wavelength from Refs. [32–34].

only significant if the waveguide height is comparable to the wavelength of light inside the core material (λ/n_1). Second, the longitudinal field component is only significant if the refractive-index contrast is relatively large. The silicon/air and SOI material systems induce the largest longitudinal components of those considered as they have the largest refractive-index contrasts (see Table 1.2). For the smallest refractive-index contrast material system considered, which corresponds to optical fiber, the longitudinal field component is relatively unnoticeable.

A description of nonlinear effects in optical waveguides typically follows a perturbative approach that is similar to coupled-mode theory. Since coupled-mode formalisms that take into account the vectorial nature of the modes have been known since the birth of low-loss optical fiber [30, 35], the knowledge required to formulate a vectorial theory of nonlinear propagation has existed for at least 40 years. Such an approach was largely neglected (to the author's knowledge) in favor of the simpler scalar one until about 10 years ago. One of the earliest theoretical studies of Raman amplification in submicron silicon waveguides used a vectorial approach [36]. The purpose of the authors in doing so was to consider the possibility of Raman-induced crosstalk between TE and TM Stokes waves, which they found to be negligible. A later theoretical study of Raman amplification in submicron silicon waveguides by a group at Columbia University also considered the vectorial nature of the optical modes [37], and later applied this formalism to self and cross-phase modulation [39, 80]. In 2009 studies were first reported that carefully considered whether or not vectorial theories of nonlinear propagation were needed, and for what types of waveguides [40–42].

This work, lead by a group at the University of Adelaide in Australia, represents the first clearly reported understanding that vectorial theories are needed for waveguides in material systems with large refractive-index contrast and subwavelength structure. They also reported an experimental confirmation of this conclusion in a bismuth glass nanowire [43].

Growing interest in photonic crystal waveguides in large index contrast material systems such as SOI [44] have further complicated the application of traditional approaches. Prior theoretical methods for understanding nonlinear effects in periodic waveguides such as fiber Bragg gratings relied on perturbative techniques for incorporating not only the nonlinearity, but the periodic refractive index modulation as well (see for example Ref. [45]). The assumption of this approach breaks down when the refractive index modulation can no longer be treated perturbatively, as in SOI photonic crystals. For this reason recent efforts have been made to extend the vectorial approach to nonlinear propagation to incorporate photonic crystal waveguides, and have been successful at formulating the underlying equations [46, 47]. The equations themselves are complicated and unwieldy, however, and their implications remain an open question.

Also of growing interest in the past decade are nonlinear effects in optical microresonators. The trend in this research, as in studies of optical waveguides, is towards ever smaller devices. Mode volumes less than a cubic wavelength are now regularly acheived in photonic-crystal cavities [48]. Integrated resonators come in many different forms, some of which, such as whispering-gallery-mode and photonic-crystal-defect cavities, are not composed of waveguides. Thus, the nonlinear Schrödinger equation is not applicable, and an alternative modeling technique is needed. This has presented a problem since many of the theoretical studies of perturbative effects in resonators have been *ad hoc* and/or heuristic throughout the history of optics. A noteable exception to this was the application of Slater's modes from microwave theory [49] to understanding nonlinear effects in optical resonators formed using mirrors [50–52]. This approach, which incorporates the full-vectorial nature of optical modes, is nonetheless limited by its assumption that the cavity is bounded by mirrors, and is thus inapplicable to the kinds of dielectric resonators considered in contemporary integrated optics. One of the most sophisticated methodologies for studying

nonlinear effects in dielectric resonators has been developed by the research group of Oskar Painter at the California Institute of Technology [53–55]. Their theoretical formalism, which also incorporates the full vector nature of the optical field, has also been shown to reproduce experimental observations to a high degree of accuracy [54, 55]. The main downside of this approach is that it relies on mode-orthogonality conditions that are not necessarily applicable to all kinds of dielectric resonators.

1.3 Thesis objective

This thesis has two objectives. The first is to present a set of comprehensive theoretical methods for nonlinear photonics that are valid for devices of any size and fabricated in material systems with any degree of refractive-index contrast. This goal is primarily synthetic. Many of the equations presented have been derived elsewhere in the literature. The methods used to derive them, however, and the resulting extension of them to the range of devices discussed in this thesis, are both original contributions to the author's knowledge. The methods presented are analytic or semi-analytic in nature, and purely numerical methods (e.g. finite-difference time-domain calculations) will not be considered. The second goal of this thesis is to apply these theoretical methods to a variety of problems in contemporary integrated optics, as demonstrations of their usefulness and accuracy. Part of this second objective will be to clarify when it is that a more comprehensive vectorial method is needed as opposed to a simpler scalar one. The problems considered will also be related to experimental results whenever possible. In some cases these experimental results are obtained by the author and his collaborators and in other cases they are taken from the literature.

1.4 Thesis outline

This thesis is divided into two parts. The first part, encompassing chapters 2-4, deals with nonlinear photonics in guided-wave structures. The second part, encompassing chapters 5-7, deals with nonlinear photonics in resonators.

Chapter 2 presents a set of perturbative methods which can be used for modeling nonlinear optical phenomena in guided wave structures. Perturbative equations

are derived for traditional dielectric waveguides, and extensions of this method to incorporate photonic-crystal waveguides, anisotropic media, and magnetic media are presented.

Chapter 3 considers the application of the method presented in chapter 2 to nonlinear propagation in SOI waveguides. Numerical studies are performed for clarifying the influence of subwavelength waveguide dimensions on both linear propagation parameters such as group-velocity and polarization-mode dispersions, as well as nonlinear parameters describing the Kerr effect, two-photon absorption, and free-carrier nonlinearities.

Chapter 4 considers the propagation of arbitrarily polarized fields in SOI waveguides. Experimental observations of both linear and nonlinear changes in the state of polarization of optical pulses are presented, and the theory of chapter 3 is used to explain them.

Chapter 5 presents a perturbative method for modeling nonlinear optical phenomena in dielectric resonators. Extensions for incorporating both anisotropic and magnetic media are presented.

Chapter 6 applies the methodology of chapter 5 to the phenomenon known as 'adiabatic wavelength conversion.' The underlying equations describing the phenomenon are derived, and their predictions are compared with experimental results from the literature. They are then used to consider the device prospects for adiabatic wavelength conversion, and a possible path to application is charted.

Chapter 7 applies the methodology of chapter 5 to Kerr-induced coupling between two resonator modes. Two-beam bistability is discussed, and a phase-switched optical memory device is proposed.

Chapter 8 summarizes the results of this thesis and discusses relevant research directions that might be pursued as an extension of it.

2 Perturbative methods for nonlinear photonic waveguides

The most accurate classical description of optical fields is Maxwell's equations [56]. First published in 1861 [57], they can be written as a set of four vector equations for the electromagnetic field. In the case of optical fields (which have no static component), two of these equations are redundant. Because optical wavelengths are much larger than the distance between atoms in most materials, an appropriate averaging of the field can be performed over spatial dimensions that are large compared to this interatomic spacing and yet small compared to the structure of the optical field [58]. The resulting equations for the electric field $\mathbf{E}$ and magnetic field $\mathbf{H}$ are as follows:

$$\nabla \times \mathbf{E} = -\mu_0 \frac{\partial}{\partial t} (\mathbf{H} + \mathbf{M}), \tag{2.1}$$

$$\nabla \times \mathbf{H} = \frac{\partial}{\partial t} (\epsilon_0 \mathbf{E} + \mathbf{P}). \tag{2.2}$$

In these equations $\mathbf{M}$ and $\mathbf{P}$ are the magnetic and electric dipole-moment densities, respectively, and describe the influence that matter has on the optical field. For the majority of materials encountered in photonics $\mathbf{M} = 0$ and the material influence is described entirely by $\mathbf{P}$. For the study of nonlinear photonic phenomena the dipole moment density is written as a sum of two distinct parts,

$$\mathbf{P} = \mathbf{P}^L + \mathbf{P}^{NL}. \tag{2.3}$$

$\mathbf{P}^L$ is the dipole-moment density that depends linearly on the electric field, and $\mathbf{P}^{NL}$ has a nonlinear field dependence.

The majority of theoretical approaches to nonlinear photonics rely on the fact that, typically, $|\mathbf{P}^{NL}| \ll |\mathbf{P}^{L}|$. Solutions are found first under the assumption of a linear medium (i.e. one for which $\mathbf{P}^{NL} = 0$), and the nonlinear dipole-moment density is then treated as a perturbative influence on these linear solutions. Scalar theories, such as those that have dominated the field of nonlinear fiber optics, typically begin by first deriving the Helmholtz equation for the electric field from Eqs. (2.1) and (2.2) [23,29]. An assumption is made that decouples the cartesian components of the field, which are then expanded in terms of the guided mode solutions of the linear problem. Perturbative theories that do not neglect the coupling between cartesian components of the electric field (i.e. vectorial theories) typically begin with the Lorentz reciprocity theorem. This approach was used in 1972 to describe linear coupling in optical fibers [35], and has more recently been applied to the field of nonlinear photonics [37, 41, 42, 47].

In this chapter the vectorial perturbative theory is approached from a vector space formulation of Eqs. (2.1) and (2.2). This vector space formulation was used to understand optical waveguides as early as 1982 [59] and ultimately stems from microwave theory [60]. It has recently been used to shed light on a variety of linear phenomena such as polarization-mode dispersion and waveguide tapering [61–64]. Its main advantage is that it presents Maxwell's equations in a simple operator form that is very similar to the Schrödinger equation from quantum mechanics, allowing familiar mathematical techniques from that field to be applied to photonics. In section 2.1 an overview of this formulation is presented for the simplest case of isotropic dielectric waveguides. The nonlinear dipole-moment density is incorporated as a perturbative term in the equations and it is shown that the mathematical methodology of time-dependent perturbation theory can be applied to formulate a z-dependent perturbation theory for nonlinear waveguides. In section 2.2 the theory is extended to incorporate the possibility of anisotropic materials. In section 2.3 it is further extended to incorporate materials with a magnetic response. In section 2.4 it is extended to incorporate photonic crystal waveguides. Section 2.5 summarizes the results of this chapter.

2.1 Dielectric waveguides in isotropic media

2.1.1 A vector space formulation of Maxwell's equations

The linear part of the dipole-moment density in an isotropic medium is in general given by a convolution [65],

$$\mathbf{P}^L(\mathbf{r},t) = \epsilon_0 \int_{-\infty}^{t} R(\mathbf{r},t-\tau)\mathbf{E}(\mathbf{r},\tau)d\tau.$$

This expression becomes much simpler in the frequency domain,

$$\widetilde{\mathbf{P}}^L(\mathbf{r},\omega) = \epsilon_0\chi(\mathbf{r},\omega)\widetilde{\mathbf{E}}(\mathbf{r},\omega),$$

where the susceptibility $\chi(\omega) = \int_0^\infty R(t)\exp(i\omega t)dt$ is the Fourier transform of the material's impulse response. Equations (2.1) and (2.2) can then be written in the frequency domain as

$$\nabla \times \widetilde{\mathbf{E}} = i\omega\mu_0\widetilde{\mathbf{H}}, \tag{2.4}$$

$$\nabla \times \widetilde{\mathbf{H}} = -i\omega\epsilon_0\epsilon\widetilde{\mathbf{E}} - i\omega\widetilde{\mathbf{P}}^{NL}, \tag{2.5}$$

where $\epsilon(\mathbf{r},\omega) = 1 + \chi(\mathbf{r},\omega)$ is the dielectric permitivitty. Although Eqs. (2.4) and (2.5) describe the Fourier transforms of the real fields, they also apply to the transforms of the complex, analytic-signal representations of those fields. In general, the Fourier transform of a real function $\widetilde{f}(\omega)$ is related to the transform of its analytic signal representation $\widetilde{F}(\omega)$ by $\widetilde{F}(\omega) = 2\Theta(\omega)\widetilde{f}(\omega)$, where $\Theta(\omega)$ is the Heaviside step function [66]. In the following analysis we will consider the quantities in Eqs. (2.4) and (2.5) to be the transforms of the analytic-signal representations of the fields. In the case of optical waveguides ϵ depends only on the transverse coordinates x and y and has no dependence on the longitudinal coordinate z. As a result it becomes useful to make a distinction between the transverse and longitudinal components of the electric and magnetic fields. In general this distinction is made for some vector field $\mathbf{A}(\mathbf{r})$ as

$$\mathbf{A} = \mathbf{A}_T + \hat{\mathbf{z}}A_z.$$

It will also be useful to make a similar distinction for the ∇ operator,

$$\nabla = \nabla_T + \hat{\mathbf{z}}\frac{\partial}{\partial z},$$

which allows us to write the curl of the vector field $\mathbf{A}$ as

$$\nabla \times \mathbf{A} = \nabla_T \times \mathbf{A}_T + \frac{\partial}{\partial z}(\hat{\mathbf{z}} \times \mathbf{A}_T) + \nabla_T \times (\hat{\mathbf{z}} A_z). \tag{2.6}$$

The first term on the right hand side of Eq. (2.6) is purely longitudinal, whereas the second and third terms are purely transverse. Using Eq. (2.6), Maxwell's Eqs. (2.4) and (2.5) can be broken up into their transverse and longitudinal components. The result is a set of four equations,

$$\begin{aligned}
\frac{\partial}{\partial z}(\hat{\mathbf{z}} \times \widetilde{\mathbf{E}}_T) + \nabla_T \times (\hat{\mathbf{z}} \widetilde{\mathbf{E}}_z) &= i\omega\mu_0 \widetilde{\mathbf{H}}_T, & (2.7)\\
\nabla_T \times \widetilde{\mathbf{E}}_T &= i\omega\mu_0 \hat{\mathbf{z}} \widetilde{H}_z, & (2.8)\\
\frac{\partial}{\partial z}(\hat{\mathbf{z}} \times \widetilde{\mathbf{H}}_T) + \nabla_T \times (\hat{\mathbf{z}} \widetilde{\mathbf{H}}_z) &= -i\omega\epsilon_0\epsilon \widetilde{\mathbf{E}}_T - i\omega \widetilde{\mathbf{P}}_T^{NL}, & (2.9)\\
\nabla_T \times \widetilde{\mathbf{H}}_T &= -i\omega\epsilon_0\epsilon \hat{\mathbf{z}} \widetilde{E}_z - i\omega \hat{\mathbf{z}} P_z^{NL}. & (2.10)
\end{aligned}$$

By using Eqs. (2.8) and (2.10) to express the longitudinal components $\widetilde{H}_z$ and $\widetilde{E}_z$ in terms of the transverse fields $\widetilde{\mathbf{H}}_T$ and $\widetilde{\mathbf{E}}_T$, Eqs. (2.7) and (2.9) can be written purely in terms of these transverse fields. The result can be summarized in a single operator equation,

$$-i\frac{\partial}{\partial z}\hat{B}\,|\psi\rangle = \hat{A}\,|\psi\rangle + |V(z)\rangle\,. \tag{2.11}$$

In Eq. (2.11) the transverse fields are expressed as a single element of a general vector space,

$$|\psi\rangle = \begin{pmatrix} \sqrt{\epsilon_0}\,\widetilde{\mathbf{E}}_T \\ \sqrt{\mu_0}\,\widetilde{\mathbf{H}}_T \end{pmatrix}. \tag{2.12}$$

Equation (2.11) describes how the electromagnetic field will traverse this vector space as it propagates along the z direction. The operators $\hat{A}$ and $\hat{B}$ are given by [59, 60]

$$\hat{A} = \begin{pmatrix} \frac{\omega\epsilon}{c} - \frac{c}{\omega}\nabla_T \times \nabla_T \times & 0 \\ 0 & \frac{\omega}{c} - \frac{c}{\omega}\nabla_T \times \frac{1}{\epsilon}\nabla_T \times \end{pmatrix}, \quad \hat{B} = \begin{pmatrix} 0 & -\hat{\mathbf{z}} \times \\ \hat{\mathbf{z}} \times & 0 \end{pmatrix}. \tag{2.13}$$

$|V(z)\rangle$ is the perturbative term in Eq. (2.11) and results from the material nonlinearity. It is expressed as

$$|V(z)\rangle = \begin{pmatrix} \omega\sqrt{\mu_0}\,\widetilde{\mathbf{P}}_T^{NL} \\ -\frac{i}{\sqrt{\epsilon_0}}\nabla_T \times \left(\frac{1}{\epsilon}\hat{\mathbf{z}}\widetilde{P}_z^{NL}\right) \end{pmatrix}. \tag{2.14}$$

The vector space under consideration is additionally a complex inner-product space under the definition

$$\langle \psi_a | \psi_b \rangle = \frac{1}{4} \iint \left(\epsilon_0 \widetilde{\mathbf{E}}_T^{a*} \cdot \widetilde{\mathbf{E}}_T^{b} + \mu_0 \widetilde{\mathbf{H}}_T^{a*} \cdot \widetilde{\mathbf{H}}_T^{b} \right) dxdy. \tag{2.15}$$

The inner product defined by Eq. (2.15) has several important properties. Under its definition the quantity $\langle \psi | \hat{B} | \psi \rangle$ is directly proportional to the time-averaged power $(\overline{P})$ of the electromagnetic field flowing in the z direction,

$$\begin{aligned} \langle \psi | \hat{B} | \psi \rangle &= \frac{1}{2c} \iint \mathrm{Re} \left\{ \left(\widetilde{\mathbf{E}}_T \times \widetilde{\mathbf{H}}_T^{*} \right) \cdot \hat{\mathbf{z}} \right\} dxdy \\ &= \frac{\overline{P}}{c}. \end{aligned} \tag{2.16}$$

Most importantly for our purposes, under the definition (2.15) operators $\hat{A}$ and $\hat{B}$ are Hermitian. The proof of this result is provided in appendix A.

2.1.2 Waveguide modes as Hermitian eigenvectors

Note that in general the dielectric permitivitty ϵ can depend on the longitudinal coordinate, and as a result the operator $\hat{A}$ can be a function of z. For the specific case of traditional dielectric waveguides this is not the case and $\hat{A}$ is a constant operator. The modes of a waveguide can then be written as

$$|\psi_k\rangle = |\beta_k\rangle \, e^{i\beta_k z}, \tag{2.17}$$

where β_k is the propagation constant of mode $|\beta_k\rangle$, which is a solution of an eigenvalue problem,

$$\hat{A} \, |\beta_k\rangle = \beta_k \hat{B} \, |\beta_k\rangle \, . \tag{2.18}$$

Note that the eigenmodes $|\beta_k\rangle$ represent the transverse part of the electric and magnetic field mode profiles [$\mathbf{e}(x, y)$ and $\mathbf{h}(x, y)$, respectively],

$$|\beta_k\rangle = \begin{pmatrix} \sqrt{\epsilon_0} \, \mathbf{e}_T \\ \sqrt{\mu_0} \, \mathbf{h}_T \end{pmatrix}. \tag{2.19}$$

Because both $\hat{A}$ and $\hat{B}$ are Hermitian, the eigenmodes of Eq. (2.18) satisfy the usual properties of Hermitian eigenvectors [61],

$$\beta_k = \beta_k^*, \tag{2.20}$$

$$\left\langle \beta_k \middle| \hat{B} \middle| \beta_l \right\rangle = 0 \qquad \text{if } \beta_k \neq \beta_l. \tag{2.21}$$

Strictly speaking, it is only the guided modes that are confined in the transverse dimensions and therefore elements of the inner-product space. Thus we cannot immediately say that Eqs. (2.20) and (2.21) hold for either evanescently decaying or radiation modes. Note, however, that Eq. (2.21) is well defined and can be shown to be valid so long as at least one of the two modes is guided. Thus, guided modes are orthogonal not only to each other but to all other kinds of modes as well. It has also been argued that orthogonality condition (2.21) can be considered to hold between two radiation modes [59, 67].

2.1.3 z-dependent perturbation theory

The perturbative theory is formulated by assuming a specific form for the electromagnetic field, namely

$$|\psi(z)\rangle = \sum_m a_m(z,\omega)\,|\beta_m\rangle\,. \tag{2.22}$$

For the sake of simplicity we will consider the sum to be over only the guided modes, although an integral over the spectrum of radiation modes can also be incorporated in the field expansion [68]. Using the assumed field solution (2.22) in Maxwell's equation (2.11) yields

$$\sum_m -i\frac{\partial a_m}{\partial z}\hat{B}\,|\beta_m\rangle = \sum_m a_m\hat{A}\,|\beta_m\rangle + |V(z)\rangle \tag{2.23}$$

$$= \sum_m \beta_m a_m\hat{B}\,|\beta_m\rangle + |V(z)\rangle\,. \tag{2.24}$$

Taking the inner product of both sides with $\langle\beta_k|$ and using the orthogonality condition (2.21) leads to an equation for the amplitude of the k^{th} mode,

$$\frac{\partial a_k}{\partial z} = i\beta_k a_k + i\frac{\langle\beta_k|V(z)\rangle}{\left\langle\beta_k\middle|\hat{B}\middle|\beta_k\right\rangle}. \tag{2.25}$$

Note that in the absence of the perturbation the solution is $a_k(z) = a_k(0)\exp(i\beta_k z)$ as expected. Using Eq. (2.14) and the definition for the inner product (2.15), Eq. (2.25) is rewritten as

$$\frac{\partial a_k}{\partial z} = i\beta_k a_k + \frac{i\omega}{4N_k}\iint \mathbf{e}^{*(k)}\cdot\widetilde{\mathbf{P}}^{NL}\,dxdy, \tag{2.26}$$

where the normalization constant N_k corresponds to the mode power,

$$N_k = \frac{1}{2}\iint \mathrm{Re}\left\{\left(\mathbf{e}^{(k)}\times\mathbf{h}^{*(k)}\right)\cdot\hat{\mathbf{z}}\right\}dxdy. \tag{2.27}$$

In deriving Eq. (2.26) we have made use of the relation $\iint \mathbf{h}_T^{*(k)}\cdot\nabla_T\times\hat{\mathbf{z}}P_z^{NL}dxdy = \iint P_z^{NL}\hat{\mathbf{z}}\cdot\nabla_T\times\mathbf{h}_T^{*(k)}dxdy$, and the fact that the waveguide modes satisfy Eq. (2.10) for $P_z^{NL} = 0$.

2.1.4 Time-domain equations

So far the development of the perturbative theory has been entirely in the frequency domain. For the study of nonlinear phenomena it is more convenient to work in the time domain in the vast majority of cases. The electromagnetic field state can be converted to the time domain by an inverse Fourier transform,

$$|\psi(z,t)\rangle = \frac{1}{2\pi}\int_{-\infty}^{\infty}|\psi(z,\omega)\rangle\,e^{-i\omega t}d\omega. \tag{2.28}$$

This presents a problem since for the frequency domain field in Eq. (2.22) both the mode amplitudes a_m and the mode profiles $|\beta_m\rangle$ depend on frequency, so the integral is not easily evaluated. In most cases the frequency dependence of the mode profiles is weak compared to that of the mode amplitudes and can be neglected, which is assumed in the following analysis. Note that in some instances this assumption may need to be revisited, such as in broadband supercontinuum generation where the mode profile may change appreciably over the field's spectrum, or near the band edge of a photonic-crystal waveguide where it is highly dispersive [47].

While the mode expansion in equation (2.22) is over all of the distinct spatial modes at a given frequency, it can be considered to include distinct spectral modes as well. Two distinct spectral modes may share a common spatial mode but have different carrier frequencies and narrow enough spectra that they are non-overlapping in the frequency domain. The index m in Eq. (2.22) will be considered to run over

all distinct spatial and spectral modes. Because the amplitudes a_m are centered at optical frequencies and vary over distances comparable to an optical wavelength, it is convenient to define slowly varying amplitudes $\widetilde{A}_m$ by the relation

$$a_m(z,\omega) = \frac{1}{\sqrt{N_m}}\widetilde{A}_m(z,\omega-\omega_0^m)\,e^{i\beta_0^m z}, \tag{2.29}$$

where ω_0^m is the carrier frequency of the m^{th} wave and $\beta_0^m = \beta_m(\omega_0^m)$ is its wavevector. Using Eqs. (2.22), (2.28), and (2.29) the time domain field is written

$$|\psi(z,t)\rangle = \sum_m \frac{A_m(z,t)}{\sqrt{N_m}}\,|\beta_m(\omega_0^m)\rangle\,e^{i(\beta_0^m z-\omega_0^m t)}, \tag{2.30}$$

where A_m is the inverse Fourier transform of $\widetilde{A}_m$ and $|\beta_m(\omega_0^m)\rangle$ denotes the m^{th} mode's profile evaluated at its carrier frequency. The total optical power of the field can be calculated by taking a local time average of Eq. (2.16),

$$\begin{aligned}\overline{P} &= c\,\overline{\langle\psi(z,t)|\hat{B}|\psi(z,t)\rangle} \\ &= \sum_m |A_m(z,t)|^2\,. \end{aligned}\tag{2.31}$$

Thus, the mode amplitudes defined by Eq. (2.29) are convenient not only because they are slowly varying in space and time, but also because $|A_m|^2$ has pysical significance (it is the optical power in the m^{th} mode). The perturbative Eq. (2.26) can be recast using definition (2.29) for $A_m(z,\omega)$ as

$$\begin{aligned}\frac{\partial\widetilde{A}_k}{\partial z} &= i\left[\beta_k(\omega+\omega_0^k)-\beta_0^k\right]\widetilde{A}_k \\ &+ \frac{i}{4\sqrt{N_k}}(\omega+\omega_0^k)\iint \mathbf{e}^{*(k)}\cdot\widetilde{\mathbf{P}}^{NL}(\mathbf{r},\omega+\omega_0^k)e^{-i\beta_0^k z}\,dxdy. \end{aligned}\tag{2.32}$$

It will also be convenient to take a Taylor series expansion of the dispersion term,

$$\beta_k(\omega+\omega_0^k) = \sum_{n=0}^{\infty}\frac{\beta_n^k}{n!}\omega^n, \tag{2.33}$$

where $\beta_n^k = \partial^n\beta_k/\partial\omega^n|_{\omega=\omega_0^k}$. Using expansion (2.33) in Eq. (2.32) and converting to the time domain yields

$$\begin{aligned}\frac{\partial A_k}{\partial z} &= \left(\sum_{n=1}^{\infty} i^{n+1}\frac{\beta_n^k}{n!}\frac{\partial^n}{\partial t^n}\right)A_k \\ &+ \frac{i\omega_0^k}{4\sqrt{N_k}}\left(1+\frac{i}{\omega_0^k}\frac{\partial}{\partial t}\right)\iint \mathbf{e}^{*(k)}\cdot\mathbf{P}^{NL}(\mathbf{r},t)\,e^{-i\left(\beta_0^k z-\omega_0^k t\right)}\,dxdy. \end{aligned}\tag{2.34}$$

Equation (2.34) is the main result of this chapter. It is a rigorous time domain description of nonlinear phenomena occuring in optical waveguides, and is the theoretical basis for chapters 3 and 4. In the remainder of this chapter it is shown that similar equations can also be derived for the more general cases of waveguides composed of anisotropic and/or magnetic media, or which may have periodicity in the z direction (i.e. photonic-crystal waveguides).

2.2 Extension to anisotropic media

In the field of photonics there are some important material systems that employ anisotropic dielectric media (e.g. $LiNbO_3$). In addition, magneto-optical effects (used to make optical isolators) can be considered to result in an anisotropic electric susceptibility [69]. In these situations the linear response of the medium is given by

$$\widetilde{\mathbf{P}}^L = \epsilon_0 \overleftrightarrow{\boldsymbol{\chi}}(\mathbf{r},\omega)\widetilde{\mathbf{E}}(\mathbf{r},\omega), \tag{2.35}$$

where $\overleftrightarrow{\boldsymbol{\chi}}$ is a 3×3 matrix. Maxwell's Eqs. (2.1) and (2.2) then become

$$\nabla \times \widetilde{\mathbf{E}} = i\omega\mu_0\widetilde{\mathbf{H}}, \tag{2.36}$$

$$\nabla \times \widetilde{\mathbf{H}} = -i\omega\epsilon_0 \overleftrightarrow{\boldsymbol{\epsilon}}\widetilde{\mathbf{E}} - i\omega\widetilde{\mathbf{P}}^{NL}. \tag{2.37}$$

In Eq. (2.37) the dielectric permitivitty tensor is $\overleftrightarrow{\boldsymbol{\epsilon}} = \mathbf{I} + \overleftrightarrow{\boldsymbol{\chi}}$, where $\mathbf{I}$ is the identity matrix. For lossless media the dielectric permitivitty tensor is Hermitian [70], i.e.

$$\epsilon_{ij}^* = \epsilon_{ji}, \tag{2.38}$$

which will be assumed in the following analysis.

The analysis that leads to the operator formulation for anisotropic waveguides follows a similar path as for the isotropic case. In breaking up Maxwell's equations into transverse and longitudinal parts, Eqs. (2.4) and (2.5) remain unchanged. The other two equations are modified to account for the anisotropy,

$$\frac{\partial}{\partial z}(\hat{\mathbf{z}}\times\mathbf{H}_T) + \nabla_T \times (\hat{\mathbf{z}}H_z) = -i\omega\epsilon_0\left[\overleftrightarrow{\boldsymbol{\epsilon}}_{\boldsymbol{T}}\widetilde{\mathbf{E}}_T + \begin{pmatrix}\epsilon_{13}\\ \epsilon_{23}\end{pmatrix}\widetilde{E}_z\right] - i\omega\widetilde{\mathbf{P}}_T^{NL}, \tag{2.39}$$

$$\nabla_T \times \widetilde{\mathbf{H}} = -i\omega\epsilon_0 \hat{\mathbf{z}} \left[\epsilon_{33} \widetilde{E}_z + \begin{pmatrix} \epsilon_{31} & \epsilon_{32} \end{pmatrix} \widetilde{\mathbf{E}}_T \right] - i\omega \hat{\mathbf{z}} P_z^{NL}, \tag{2.40}$$

where

$$\overleftrightarrow{\boldsymbol{\epsilon}_T} = \begin{pmatrix} \epsilon_{11} & \epsilon_{12} \\ \epsilon_{21} & \epsilon_{22} \end{pmatrix}. \tag{2.41}$$

By solving Eqs. (2.8) and (2.40) for the longitudinal field components and using the resulting expressions in Eqs. (2.7) and (2.39) a pair of equations for the transverse fields is found and formulated as a single operator equation. The result is that Eq. (2.11) still holds, however the $\hat{A}$ operator and the perturbative term $|V(z)\rangle$ both take different forms. As described in appendix A, $\hat{A}$ can be written in terms of composite elements as

$$\hat{A} = \begin{pmatrix} \hat{A}_{11} & \hat{A}_{12} \\ \hat{A}_{21} & \hat{A}_{22} \end{pmatrix}. \tag{2.42}$$

For the isotropic case the off-diagonal elements are equal to zero, whereas for the anisotropic case this is no longer true. The elements are given by [59, 60]

$$\hat{A}_{11} = \frac{\omega}{c} \left[\overleftrightarrow{\boldsymbol{\epsilon}_T} - \frac{1}{\epsilon_{33}} \begin{pmatrix} \epsilon_{13}\epsilon_{31} & \epsilon_{13}\epsilon_{32} \\ \epsilon_{23}\epsilon_{31} & \epsilon_{23}\epsilon_{32} \end{pmatrix} \right] - \frac{c}{\omega} \nabla_T \times \nabla_T \times, \tag{2.43}$$

$$\hat{A}_{12} = \frac{i}{\epsilon_{33}} \begin{pmatrix} \epsilon_{13} \\ \epsilon_{23} \end{pmatrix} \hat{\mathbf{z}} \cdot \nabla_T \times, \tag{2.44}$$

$$\hat{A}_{21} = -i \nabla_T \times \hat{\mathbf{z}} \frac{1}{\epsilon_{33}} \begin{pmatrix} \epsilon_{31} & \epsilon_{32} \end{pmatrix}, \tag{2.45}$$

$$\hat{A}_{22} = \frac{\omega}{c} - \frac{c}{\omega} \nabla_T \times \frac{1}{\epsilon_{33}} \nabla_T \times . \tag{2.46}$$

Under the assumption of a Hermitian permitivitty tensor the $\hat{A}$ operator remains Hermitian. The proof of this result is provided in appendix A.

Because $\hat{A}$ is also Hermitian for the anisotropic case, the assumptions that led to Eq. (2.25) are still valid and hence (2.25) still applies. Its meaning, however, is slightly different since $|V(z)\rangle$ takes a slightly different form, namely

$$|V(z)\rangle = \begin{pmatrix} \omega\sqrt{\mu_0} \widetilde{\mathbf{P}}_T^{NL} - \omega\sqrt{\mu_0} \frac{1}{\epsilon_{33}} \begin{pmatrix} \epsilon_{13} \\ \epsilon_{23} \end{pmatrix} \widetilde{P}_z^{NL} \\ \\ -\frac{i}{\sqrt{\epsilon_0}} \nabla_T \times \left(\frac{1}{\epsilon_{33}} \hat{\mathbf{z}} \widetilde{P}_z^{NL} \right) \end{pmatrix}. \tag{2.47}$$

Eq. (2.47) differs from (2.14) by an anisotropic contribution and reduces to it in the case of a scalar ϵ, as expected. By again making use of the relation $\iint \mathbf{h}_T^{*(k)} \cdot \nabla_T \times \hat{\mathbf{z}} P_z^{NL} dxdy = \iint P_z^{NL} \hat{\mathbf{z}} \cdot \nabla_T \times \mathbf{h}_T^{*(k)} dxdy$, and the fact that the waveguide modes satisfy (2.40) for $P_z^{NL} = 0$, it can be shown that the terms depending on the off-diagonal tensor elements cancel out so that in the case of anisotropic media Eq. (2.25) reduces to

$$\frac{\partial a_k}{\partial z} = i\beta_k a_k + \frac{i\omega}{4N_k} \iint \mathbf{e}^{*(k)} \cdot \mathbf{P}^{NL} \, dxdy. \tag{2.48}$$

Thus, the exact same form of the perturbative equation for isotropic media (Eq. (2.26) holds in the anisotropic case. As a result Eq. (2.34) is also the appropriate time-domain description of nonlinear phenomena in optical waveguides composed of anisotropic materials.

2.3 Extension to magnetic media

Most materials used in the field of photonics are nonmagnetic. There are, however, some notable exceptions to this rule. In recent years artificially engineered 'metamaterials' that have a magnetic response have been developed in order to achieve negative refraction [71, 72]. In addition, it has recently been demonstrated that commonly used optical materials exhibit a significant nonlinear magnetic response at particular resonant frequencies [73]. In this chapter the perturbative theory is extended to incorporate a magnetic material response.

As for the electric dipole-moment density, a distinction is made between the linear and nonlinear contributions to the magnetic dipole-moment density,

$$\widetilde{\mathbf{M}} = \widetilde{\mathbf{M}}^L + \widetilde{\mathbf{M}}^{NL}. \tag{2.49}$$

It is assumed that the nonlinear contribution is weak enough to have only a perturbative effect on the propagation of the field. We will not necessarily make this assumption about the linear contribution, allowing it to take the form

$$\widetilde{\mathbf{M}}^L(\mathbf{r}, \omega) = \overleftrightarrow{\boldsymbol{\chi}}^M(\mathbf{r}, \omega) \widetilde{\mathbf{H}}(\mathbf{r}, \omega), \tag{2.50}$$

where $\overleftrightarrow{\boldsymbol{\chi}}^M$ is the magnetic susceptibility tensor. With this assumption Maxwell's Eqs. (2.1) and (2.2) become

$$\nabla \times \widetilde{\mathbf{E}} = i\omega\mu_0 \overleftrightarrow{\boldsymbol{\mu}} \widetilde{\mathbf{H}} + i\omega\mu_0 \widetilde{\mathbf{M}}^{NL}, \tag{2.51}$$

$$\nabla \times \widetilde{\mathbf{H}} = -i\omega\epsilon_0 \overleftrightarrow{\boldsymbol{\epsilon}} \widetilde{\mathbf{E}} - i\omega \widetilde{\mathbf{P}}^{NL}, \tag{2.52}$$

where $\overleftrightarrow{\boldsymbol{\mu}} = \mathbf{I} + \overleftrightarrow{\boldsymbol{\chi}}^M$ is the magnetic permeability tensor. Just as for the permitivitty, the permeability is assumed to be Hermitian,

$$\mu_{ij}^* = \mu_{ji}. \tag{2.53}$$

The analysis proceeds in the same manner as for the case of nonmagnetic media. In breaking Maxwell's equations into transverse and longitudinal parts it is found that Eqs. (2.39) and (2.40) result from Eq. (2.52), and that Eq. (2.51) becomes

$$\frac{\partial}{\partial z}\left(\hat{\mathbf{z}} \times \widetilde{\mathbf{E}}_T\right) + \nabla_T \times \left(\hat{\mathbf{z}}\widetilde{E}_z\right) = i\omega\mu_0 \left[\overleftrightarrow{\boldsymbol{\mu}_T} \widetilde{\mathbf{H}}_T + \begin{pmatrix} \mu_{13} \\ \mu_{23} \end{pmatrix} \widetilde{H}_z \right] + i\omega\mu_0 \widetilde{\mathbf{M}}_T^{NL}, \tag{2.54}$$

$$\nabla_T \times \widetilde{\mathbf{E}}_T = i\omega\mu_0 \hat{\mathbf{z}} \left[\begin{pmatrix} \mu_{31} & \mu_{32} \end{pmatrix} \widetilde{\mathbf{H}}_T + \mu_{33} \widetilde{H}_z \right] + i\omega\mu_0 \hat{\mathbf{z}} \widetilde{M}_z^{NL}. \tag{2.55}$$

By again solving Eqs. (2.40) and (2.55) for the longitudinal field components and using them in (2.39) and (2.54) Maxwell's equations for the transverse field components in anisotropic and magnetic media can also be cast in the form (2.11), except that $\hat{A}$ and $|V(z)\rangle$ are both different. $\hat{A}$ has component elements that are given by [59, 60]

$$\begin{aligned}
\hat{A}_{11} &= \frac{\omega}{c}\left[\overleftrightarrow{\boldsymbol{\epsilon}_T} - \frac{1}{\epsilon_{33}} \begin{pmatrix} \epsilon_{13}\epsilon_{31} & \epsilon_{13}\epsilon_{32} \\ \epsilon_{23}\epsilon_{31} & \epsilon_{23}\epsilon_{32} \end{pmatrix} \right] - \frac{c}{\omega} \nabla_T \times \frac{1}{\mu_{33}} \nabla_T \times, \\
\hat{A}_{12} &= \frac{i}{\epsilon_{33}} \begin{pmatrix} \epsilon_{13} \\ \epsilon_{23} \end{pmatrix} \hat{\mathbf{z}} \cdot \nabla_T \times + i \nabla_T \times \hat{\mathbf{z}} \frac{1}{\mu_{33}} \begin{pmatrix} \mu_{31} & \mu_{32} \end{pmatrix}, \\
\hat{A}_{21} &= -i \nabla_T \times \hat{\mathbf{z}} \frac{1}{\epsilon_{33}} \begin{pmatrix} \epsilon_{31} & \epsilon_{32} \end{pmatrix} - \frac{i}{\mu_{33}} \begin{pmatrix} \mu_{13} \\ \mu_{23} \end{pmatrix} \hat{\mathbf{z}} \cdot \nabla_T \times, \\
\hat{A}_{22} &= \frac{\omega}{c}\left[\overleftrightarrow{\boldsymbol{\mu}_T} - \frac{1}{\mu_{33}} \begin{pmatrix} \mu_{13}\mu_{31} & \mu_{13}\mu_{32} \\ \mu_{23}\mu_{31} & \mu_{23}\mu_{32} \end{pmatrix} \right] - \frac{c}{\omega} \nabla_T \times \frac{1}{\epsilon_{33}} \nabla_T \times .
\end{aligned} \tag{2.56}$$

It can be shown (see appendix A) that in this form $\hat{A}$ is Hermitian as well. Thus, the perturbative Eq. (2.25) applies. $|V(z)\rangle$ is given by

$$|V(z)\rangle = \begin{pmatrix} \omega\sqrt{\mu_0}\widetilde{\mathbf{P}}_T^{NL} - \omega\sqrt{\mu_0}\frac{1}{\epsilon_{33}}\begin{pmatrix}\epsilon_{13}\\ \epsilon_{23}\end{pmatrix}\widetilde{P}_z^{NL} + i\sqrt{\mu_0}\nabla_T \times \left(\frac{1}{\mu_{33}}\hat{\mathbf{z}}\widetilde{M}_z^{NL}\right) \\ \\ -\frac{i}{\sqrt{\epsilon_0}}\nabla_T \times \left(\frac{1}{\epsilon_{33}}\hat{\mathbf{z}}\widetilde{P}_z^{NL}\right) + \frac{\omega\sqrt{\mu_0}}{c}\widetilde{\mathbf{M}}_T^{NL} - \frac{\omega\sqrt{\mu_0}}{c}\frac{1}{\mu_{33}}\begin{pmatrix}\mu_{13}\\ \mu_{23}\end{pmatrix}\widetilde{M}_z^{NL} \end{pmatrix}. \tag{2.57}$$

Using this form for the perturbation, and Eqs. (2.40) and (2.55), Eq. (2.25) can be simplified to

$$\frac{\partial a_k}{\partial z} = i\beta_k a_k + \frac{i\omega}{4N_k}\iint \mathbf{e}^{*(k)}\cdot\widetilde{\mathbf{P}}^{NL}\,dxdy + \frac{i\omega\mu_0}{4N_k}\iint \mathbf{h}^{*(k)}\cdot\widetilde{\mathbf{M}}^{NL}\,dxdy. \tag{2.58}$$

The influence of the nonlinear magnetic dipole-moment density is therefore to add an additional term to the perturbative equation. Following the procedure of section 2.1.4 leads to the time domain version of this equation for the mode-power amplitude A_k,

$$\begin{aligned}\frac{\partial A_k}{\partial z} &= \left[\sum_{n=1}^{\infty} i^{n+1}\frac{\beta_n^k}{n!}\frac{\partial^n}{\partial t^n}\right]A_k \\ &+ \frac{i\omega_0^k}{4\sqrt{N_k}}\left(1+\frac{i}{\omega_0^k}\frac{\partial}{\partial t}\right)\iint\left[\mathbf{e}^{*(k)}\cdot\mathbf{P}^{NL} + \mu_0\mathbf{h}^{*(k)}\cdot\mathbf{M}^{NL}\right]e^{-i\left(\beta_0^k z-\omega_0^k t\right)}\,dxdy.\end{aligned} \tag{2.59}$$

2.4 Extension to photonic-crystal waveguides

The casting of Maxwell's equations into the form given by Eq. (2.11) made no assumptions about the type of structure under consideration or the inhomogeneous nature of its composition, but only on the kinds of materials used to make it. We were able to formulate the perturbative theory for traditional dielectric waveguides because, for that specific case, $\hat{A}$ was a constant (independent of z). In the case of photonic-crystal waveguides this is no longer true. In particular, the material properties are periodic

along the z direction with a period Λ. As a result the operator $\hat{A}$ is periodic with period Λ as well,

$$\hat{A}(z+\Lambda) = \hat{A}(z). \tag{2.60}$$

In this case there are still guided-mode solutions similar to the ones described by Eq. (2.17). These are referred to as Bloch modes and can be expressed as

$$|\psi_k\rangle = |\beta_k(z)\rangle\, e^{i\beta_k z}, \tag{2.61}$$

where $|\beta_k(z)\rangle$ is now a Bloch function that depends on z. More specifically, $|\beta_k(z)\rangle$ is periodic with period Λ [74],

$$|\beta_k(z+\Lambda)\rangle = |\beta_k(z)\rangle\,. \tag{2.62}$$

There are no necessary constraints on the propagation constants β_k, but by convention they are usually 'mapped' to the first Brillouin zone so that

$$-\frac{\pi}{\Lambda} < \beta_k \leq \frac{\pi}{\Lambda}, \tag{2.63}$$

which is assumed here as well. Because $|\beta_k\rangle$ depends on z the eigenvalue Eq. (2.18) that describes the modes of traditional waveguides no longer holds. The appropriate eigenvalue equation for Bloch modes is [63]

$$\beta_k \hat{B}\,|\beta_k\rangle = \hat{A}(z)\,|\beta_k\rangle + i\hat{B}\frac{\partial}{\partial z}\,|\beta_k\rangle\,. \tag{2.64}$$

Because Eq. (2.64) is not a traditional eigenvalue problem for Hermitian operators, it is not immediately obvious what properties the Bloch modes have. It turns out that they satisfy the orthogonality condition (2.21) for all z [75]. The simplest way to demonstrate this is by using the Lorentz reciprocity theorem. The Lorentz reciprocity theorem, which holds for all of the types of material systems considered so far in this chapter, follows directly from Maxwell's equations [68] and states that for any two solutions of the linear problem $\left(\widetilde{\mathbf{E}}_k, \widetilde{\mathbf{H}}_k \text{ and } \widetilde{\mathbf{E}}_l, \widetilde{\mathbf{H}}_l\right)$,

$$\nabla \cdot \left(\widetilde{\mathbf{E}}_k^* \times \widetilde{\mathbf{H}}_l + \widetilde{\mathbf{E}}_l \times \widetilde{\mathbf{H}}_k^*\right) = 0. \tag{2.65}$$

Note that by integrating over any volume in space V and applying Gauss's theorem, Eq. (2.65) becomes

$$\oiint_{\delta V} \left(\widetilde{\mathbf{E}}_k^* \times \widetilde{\mathbf{H}}_l + \widetilde{\mathbf{E}}_l \times \widetilde{\mathbf{H}}_k^*\right) \cdot d\mathbf{S} = 0, \tag{2.66}$$

where the surface integral is over the boundary of V.

Consider the application of Eq. (2.66) to two Bloch modes. The two solutions can be written in the form

$$\begin{aligned} \widetilde{\mathbf{E}}_k &= \mathbf{e}^{(k)}(\mathbf{r})e^{i\beta_k z}, \qquad \widetilde{\mathbf{E}}_l = \mathbf{e}^{(l)}(\mathbf{r})e^{i\beta_l z}, \\ \widetilde{\mathbf{H}}_k &= \mathbf{h}^{(k)}(\mathbf{r})e^{i\beta_k z}, \qquad \widetilde{\mathbf{H}}_l = \mathbf{h}^{(l)}(\mathbf{r})e^{i\beta_l z}. \end{aligned} \tag{2.67}$$

Here $\mathbf{e}^{(k)}$ and $\mathbf{h}^{(k)}$ are the Bloch mode profiles which are periodic so that, for example,

$$\mathbf{e}^{(k)}(x, y, z + \Lambda) = \mathbf{e}^{(k)}(x, y, z). \tag{2.68}$$

By choosing the volume V to be a rectangular box with faces along the planes $z = z_0$ and $z = z_0 + \Lambda$, and taking the limit as the extent of these two faces becomes infinite, Eq. (2.66) for the Bloch mode solutions (2.67) leads to the relation [75]

$$\left(e^{i(\beta_l - \beta_k)\Lambda} - 1\right) \iint_{-\infty}^{\infty} \left(\mathbf{e}^{*(k)} \times \mathbf{h}^{(l)} + \mathbf{e}^{(l)} \times \mathbf{h}^{*(k)}\right) \cdot \hat{\mathbf{z}}\, dxdy = 0, \tag{2.69}$$

which from Eq. (2.15) can be demonstrated to be equivalent to

$$\left(e^{i(\beta_l - \beta_k)\Lambda} - 1\right) \left\langle \beta_k \middle| \hat{B} \middle| \beta_l \right\rangle = 0. \tag{2.70}$$

Because we are assuming that the propagation constants are mapped to the first Brillouin zone (Eq. (2.63)), this implies the orthogonality condition

$$\left\langle \beta_k \middle| \hat{B} \middle| \beta_l \right\rangle = 0 \qquad \text{for } \beta_k \neq \beta_l. \tag{2.71}$$

2.4.1 z-dependent perturbation theory for photonic-crystal waveguides

The z-dependent perturbation theory must be derived for photonic-crystal waveguides in a slightly different way. The solution of Eq. (2.11) is assumed to be an expansion of the Bloch modes,

$$|\psi(z)\rangle = \sum_m a_m(z, \omega)\, |\beta_m(z)\rangle\,. \tag{2.72}$$

Using (2.72) in (2.11),

$$\begin{aligned} \sum_m -i\frac{\partial a_m}{\partial z}\hat{B}\,|\beta_m\rangle &= \sum_m a_m \left(\hat{A}\,|\beta_m\rangle + i\hat{B}\frac{\partial}{\partial z}\,|\beta_m\rangle\right) + |V(z)\rangle \\ &= \sum_m \beta_m a_m \hat{B}\,|\beta_m\rangle + |V(z)\rangle\,, \end{aligned} \tag{2.73}$$

where we've made use of the eigenvalue Eq. (2.64). Taking the inner product from the left with $\langle\beta_k|$ and using orthogonality condition (2.71) we arrive at the familiar perturbative equation,

$$\frac{\partial a_k}{\partial z} = i\beta_k a_k + i\frac{\langle\beta_k|V(z)\rangle}{\langle\beta_k|\hat{B}|\beta_k\rangle}, \tag{2.74}$$

which is identical in form to the one for traditional waveguides (2.25). The meaning is slightly different since the modes $|\beta_k\rangle$ are the Bloch modes that depend on z.

Note that the simplification of Eq. (2.74) to Eqs. (2.34) and (2.59) did not require that either the mode profiles or the nonlinear dipole moment densities be independent of z. We conclude that the perturbative Eqs. (2.34) and (2.59) can be generalized to the case of photonic-crystal waveguides for the various material systems considered in this chapter.

2.5 Summary

In this chapter a general form of the nonlinear Schrödinger equation was derived [Eq. (2.34)]. This equation is valid for waveguides with subwavelength dimensions since it takes into account the vectorial nature of the modes. It was shown that it applies not only to waveguides composed of isotropic materials, but to waveguides composed of anisotropic materials as well. In the case of magnetic materials a slightly modified form of the equation [Eq. (2.59)] was derived that takes into account the possibility of a nonlinear magnetic response. Finally, both Eqs. (2.34) and (2.59) were shown to apply to photonic-crystal waveguides, where the mode profiles that appear in the equations are the Bloch modes of the periodic structure.

3 Nonlinear propagation in silicon waveguides: the influence of subwavelength dimensions

The first study of nonlinear propagation of optical pulses through a silicon waveguide in the 1.55 μm wavelength regime was reported in 2002 [19]. Kerr-induced spectral broadening and two-photon absorption were clearly observed, and the intensity-dependent refractive index of silicon was determined to be about two orders of magnitude larger than that of silica. A later study [76] demonstrated that, in addition to the Kerr effect, a dynamic concentration of electron-hole pairs generated by two-photon absorption can modify the spectrum of optical pulses when their power levels are sufficiently high. Since then a number of experimental and theoretical studies have been performed to further clarify the nature of self-phase modulation in silicon waveguides [77–85]. Most of these studies have considered the case when only a single spatial mode of the waveguide is excited, such as occurs for incident pulses that are linearly polarized at the appropriate angle. Three exceptions are Refs. [83–85], two of which [84,85] are works by the author that contribute to this chapter and the next.

In this chapter a theory is formulated of nonlinear propagation of arbitrarily-polarized optical pulses through silicon waveguides. Special attention is paid to waveguides with subwavelength dimensions. In section 3.1 the governing equations are derived using the theoretical methodology of chapter 2. The vectorial nature of the modes is included in the theory and important parameters that determine how pulses propagate are derived. In section 3.2 the dependence of these parameters on waveguide dimensions is studied. Section 3.3 summarizes the conclusions drawn in

this chapter.

3.1 Governing equations

3.1.1 Nonlinear contributions

The theoretical development begins with Eq. (2.34). In the case of silicon waveguides the nonlinear dipole-moment density can be written as a sum of two distinct contributions,

$$\mathbf{P}^{NL}(\mathbf{r},t) = \mathbf{P}^{(3)}(\mathbf{r},t) + \mathbf{P}^{(fc)}(\mathbf{r},t), \tag{3.1}$$

where $\mathbf{P}^{(3)}$ results from the third-order susceptibility of silicon and describes the influence of the Kerr effect and two-photon absorption. $\mathbf{P}^{(fc)}$ describes changes in the refractive index and absorption coefficient resulting from free charge carriers generated by two-photon absorption. In some cases a third contribution to the nonlinear dipole-moment density from the Raman interaction should also be included [23,37]. In silicon the Raman resonance is <1 nm wide and spaced >100 nm away from a pump beam (in the 1.55 μm wavelength regime) and can therefore be neglected for fields of moderate spectral width, which will be considered here. In this case $\mathbf{P}^{(3)}$ can be written in terms of the third-order susceptibility tensor $\chi^{(3)}_{\mu\alpha\beta\gamma}$ and the electric field $\mathbf{E}$ as [65]

$$P^{(3)}_{\mu}(\mathbf{r},t) = \frac{3\varepsilon_0}{4}\sum_{\alpha,\beta,\gamma}\chi^{(3)}_{\mu\alpha\beta\gamma}\left(\omega_0;\omega_0,-\omega_0,\omega_0\right)\,E_{\alpha}(\mathbf{r},t)E^{*}_{\beta}(\mathbf{r},t)E_{\gamma}(\mathbf{r},t), \tag{3.2}$$

where the greek subscripts denote the cartesian components of the field and ω_0 is the central frequency of the optical pulse. In the case of silicon the components of the third-order susceptibility tensor can be written as [23, 86]

$$\chi^{(3)}_{\mu\alpha\beta\gamma} = \chi_c\left[\frac{\rho}{3}\left(\delta_{\mu\alpha}\delta_{\beta\gamma}+\delta_{\mu\beta}\delta_{\alpha\gamma}+\delta_{\mu\gamma}\delta_{\alpha\beta}\right)+\left(1-\rho\right)\sum_{q}R_{q\mu}R_{q\alpha}R_{q\beta}R_{q\gamma}\right], \tag{3.3}$$

where ρ is an anisotropy parameter. If ρ were equal to 1 then the susceptibility would have the same form as that of an isotropic medium [87]. This is not the case, however, and a measurement of $\rho \approx 1.27$ over a broad spectral range has been made [86]. In Eq. (3.3) the matrix elements $R_{\alpha\beta}$ belong to a rotation matrix that maps coordinates from the crystallographic system into the one used to describe the waveguide modes.

For cleaving convenience it is common to fabricate waveguides so that the direction of propagation (i.e. the z-axis) is along the crystallographic $[\bar{1}\ \bar{1}\ 0]$ direction, which is assumed in this chapter. The rotation matrix can then be expressed as

$$\begin{pmatrix} R_{11} & R_{12} & R_{13} \\ R_{21} & R_{22} & R_{23} \\ R_{31} & R_{32} & R_{33} \end{pmatrix} = \frac{1}{\sqrt{2}} \begin{pmatrix} 1 & 0 & -1 \\ -1 & 0 & -1 \\ 0 & \sqrt{2} & 0 \end{pmatrix}. \tag{3.4}$$

The coefficient χ_c in Eq. (3.3) is the element $\chi^{(3)}_{1111}$ in the crystallographic coordinate system and is given by [65, 87]

$$\chi_c = \frac{4}{3}\varepsilon_0 c n_0^2 n_2 (1 + ir), \qquad r = \frac{\beta_{TPA}}{2k_0 n_2}, \tag{3.5}$$

where n_2 is the intensity dependent refractive index and β_{TPA} is the two-photon absorption coefficient. Measurements of these parameters have been reported by a number of research groups and vary over a considerable range [19, 76, 79, 88, 89]. Many of these reported values are not more than estimates, however, with the two exceptions (in the author's opinion) being the z-scan measurements from Refs. [88,89]. Here we will use the values from Ref. [89] and take $n_2 = 2.5 \times 10^{-18}$ m^2/W and $\beta_{TPA} = 0.45$ cm/GW. With these values $r \approx 0.25$ in Eq. (3.5) at the 1.55 μm wavelength.

When free electron-hole pairs are generated in silicon the refractive index is reduced by the resulting plasma effect, and the absorption coefficient is enhanced. This change in refractive index Δn^{fc} and absorption coefficient $\Delta\alpha^{fc}$ leads to a free-carrier induced dipole-moment density,

$$\mathbf{P}^{(fc)}(\mathbf{r}, t) = 2\varepsilon_0 n_0 \left[\Delta n^{fc} + (i/2k_0)\Delta\alpha^{fc}\right] \mathbf{E}(\mathbf{r}, t). \tag{3.6}$$

For silicon these changes can be expressed in terms of the number density of free carriers $N(\mathbf{r}, t)$ generated at any point in the medium using a semi-empirical model [90]

$$\Delta\alpha^{fc} = \sigma_a N, \tag{3.7}$$

$$\Delta n^{fc} = -\sigma_n^e N - (\sigma_n^h N)^{4/5}, \tag{3.8}$$

where $\sigma_a = 14.5 \times 10^{-18}$ cm^2, $\sigma_n^e = 8.8 \times 10^{-22}$ cm^3, and $\sigma_n^h = 4.6 \times 10^{-22}$ cm^3.

3.1.2 Coupled TE and TM mode amplitude equations

A given waveguide may be able to support a large number of spatial modes that all must be taken into account for an accurate description. The number of modes supported by a given waveguide depends on its dimensions, and waveguides with dimensions smaller than or comparable to the effective wavelength in the core material typically support a small number of modes. Often only the fundamental TE and TM modes are supported, and in other cases a small number of higher-order modes may be supported in addition to these two. In experimental situations where a lens is used to focus the optical pulses into the waveguide from free space the relative excitation of these higher-order modes is relatively weak as a result of their asymmetric spatial structure [91]. Thus it is often the case that only the fundamental TE and TM modes need to be taken into account for an accurate theoretical description, which is the approach taken here. With this assumption the transverse part of the electric field is determined from Eqs. (2.30) and (2.19). The most accurate expression for the longitudinal electric field component would then be obtained from Eq. (2.10), which presents a complication because Eq. (2.10) contains a component of the perturbing dipole-moment density, $\widetilde{P}_z^{NL}$. However, since this term is perturbative in nature (and hence relatively weak) it can be neglected in the solution for E_z, leading to the overall electric field solution

$$\mathbf{E}(\mathbf{r},t) \approx \frac{A_1(z,t)}{\sqrt{N_1}}\mathbf{e}^{(1)}(x,y)\, e^{i\left(\beta_0^{(1)}z-\omega_0 t\right)} + \frac{A_2(z,t)}{\sqrt{N_2}}\mathbf{e}^{(2)}(x,y)\, e^{i\left(\beta_0^{(2)}z-\omega_0 t\right)}, \tag{3.9}$$

where 1 and 2 denote the fundamental TE and TM modes, respectively. The coupled nonlinear Schrödinger equations are then derived from Eq. (2.34), with the nonlinear dipole-moment density given by Eqs. (3.1), (3.2), and (3.6), and the electric field given by Eq. (3.9). The result is the following:

$$\frac{\partial A_k}{\partial z} = \left(\sum_{n=1}^{\infty} i^{n+1}\frac{\beta_n^{(k)}}{n!}\frac{\partial^n}{\partial t^n}\right)A_k + T_{3o}^k + T_{fc}^k, \tag{3.10}$$

where

$$T_{3o}^{k} = \sum_{lmn} \frac{3i\omega_0\varepsilon_0}{16(N_k N_l N_m N_n)^{1/2}} A_l A_m^* A_n \, e^{i\Delta\beta_{klmn}z} \times \sum_{\mu\alpha\beta\gamma} \iint \chi^{(3)}_{\mu\alpha\beta\gamma} e_\mu^{*(k)} e_\alpha^{(l)} e_\beta^{*(m)} e_\gamma^{(n)} \, dx\, dy, \tag{3.11}$$

$$T_{fc}^{k} = \sum_{l} i\frac{\omega_0\varepsilon_0 n_0}{2(N_k N_l)^{1/2}} A_l \, e^{i\left(\beta_0^{(l)} - \beta_0^{(k)}\right)z} \times \iint \left[\Delta n^{fc} + (i/2k_0)\Delta\alpha^{fc}\right] \mathbf{e}^{*(k)} \cdot \mathbf{e}^{(l)} \, dx\, dy. \tag{3.12}$$

The indices k, l, m, and n take on the values 1 and 2 for the two modes under consideration. The terms (3.11) and (3.12) can be greatly simplified in most practical situations. Since most silicon waveguides exhibit a large birefringence, only three of the eight terms in (3.11) typically need to be taken into account as the rest are not phase matched. Similarly, only the term for which $l = k$ in Eq. (3.12) coherently affects propagation in the presence of strong birefringence and the other can be dropped. Alternatively, even if the birefringence is weak many of the terms in the sums in (3.11) and (3.12) will evaluate to zero if the waveguide exhibits a reflection symmetry in either the x or y directions. In this case Eq. (3.10) for each of the two modes reduces to

$$\begin{aligned} \frac{\partial A_1}{\partial z} &= \left(\sum_{n=1}^{\infty} i^{n+1}\frac{\beta_n^{(1)}}{n!}\frac{\partial^n}{\partial t^n}\right) A_1 + i\gamma_{11}(1+ir)|A_1|^2 A_1 + i\gamma_{12}(1+ir)|A_2|^2 A_1 \\ &+ i\gamma_{12}'(1+ir)A_2^2 A_1^* e^{-2ik_0\Delta n z} + \left(ik_0\Delta n_1^{fc} - \frac{\Delta\alpha_1^{fc}}{2}\right) A_1 - \frac{\alpha_1}{2}A_1, \end{aligned} \tag{3.13}$$

$$\begin{aligned} \frac{\partial A_2}{\partial z} &= \left(\sum_{n=1}^{\infty} i^{n+1}\frac{\beta_n^{(2)}}{n!}\frac{\partial^n}{\partial t^n}\right) A_2 + i\gamma_{22}(1+ir)|A_2|^2 A_2 + i\gamma_{12}(1+ir)|A_1|^2 A_2 \\ &+ i\gamma_{12}'(1+ir)A_1^2 A_2^* e^{2ik_0\Delta n z} + \left(ik_0\Delta n_2^{fc} - \frac{\Delta\alpha_2^{fc}}{2}\right) A_2 - \frac{\alpha_2}{2}A_2. \end{aligned} \tag{3.14}$$

3.1.3 Nonlinear parameters

Third-order nonlinear parameters

The nonlinear (γ) parameters in Eqs. (3.13) and (3.14) are given by

$$\begin{aligned}\gamma_{11} &= \frac{n_0^2\Gamma_1^2}{\overline{n}_1^2\overline{a}_1}\eta_{11}k_0n_2, \qquad \gamma_{22} = \frac{n_0^2\Gamma_2^2}{\overline{n}_2^2\overline{a}_2}\eta_{22}k_0n_2,\\ \gamma_{12} &= \frac{2n_0^2\Gamma_1\Gamma_2\eta_{12}k_0n_2}{\overline{n}_1\overline{n}_2\left(\overline{a}_1\overline{a}_2\right)^{1/2}}, \quad \gamma_{12}^{'} = \frac{n_0^2\Gamma_1\Gamma_2\eta_{12}^{'}k_0n_2}{\overline{n}_1\overline{n}_2\left(\overline{a}_1\overline{a}_2\right)^{1/2}},\end{aligned} \tag{3.15}$$

where $k_0 = 2\pi/\lambda$ is the freespace wavevector, $\overline{n}_k$ is the effective index of mode k, and n_0 is the refractive index of silicon. The terms in Eqs. (3.15) measure properties of a waveguide mode or how it interacts with the material nonlinearity. The *effective mode area* is defined as

$$\overline{a}_k = \frac{\left(\iint |\mathbf{e}^{(k)}|^2 dxdy\right)^2}{\iint \left(|\mathbf{e}^{(k)}|^2\right)^2 dxdy}, \tag{3.16}$$

and quantifies the cross-sectional area of the mode. In the special case that the mode profiles are scalar quantites, or can be approximated as scalar quantities, the definition of the effective mode area in Eq. (3.16) reduces to the one commonly used in nonlinear fiber optics [29].

Γ_k is a unitless quantity that will be referred to as a *longitudinal enhancement factor*. It is defined as

$$\Gamma_k = \frac{\iint |\mathbf{e}^{(k)}|^2 dxdy}{\iint |\mathbf{e}_T^{(k)}|^2 + (\beta^{(k)})^{-1}\mathrm{Im}\left\{\mathbf{e}_T^{(k)} \cdot \nabla_T e_z^{k*}\right\} dxdy}. \tag{3.17}$$

For purely transverse fields $\Gamma_k = 1$. In the presence of a significant longitudinal field component Γ_k deviates from this value, and, as will be shown in section 3.2, exceeds 1. Thus, a strong longitudinal field component enhances the nonlinearity experienced by a mode. This conclusion will be revisted in section 3.1.4 where a physical explanation of this phenomenon is discussed.

The interaction of a given mode with the material nonlinearity is measured by the unitless parameters η_{lm}, which will be referred to as *nonlinear overlap factors*.

They are defined by overlap integrals of the waveguide modes with the third-order susceptibility tensor,

$$\eta_{lm} = \sum_{\mu\alpha\beta\gamma} \frac{\chi_c^{-1} \iint \chi^{(3)}_{\mu\alpha\beta\gamma} e^{*(l)}_{\mu} e^{(l)}_{\alpha} e^{*(m)}_{\beta} e^{(m)}_{\gamma} dxdy}{\left[\iint \left(|\mathbf{e}^{(l)}|^2\right)^2 dxdy \iint \left(|\mathbf{e}^{(m)}|^2\right)^2 dxdy \right]^{1/2}}, \tag{3.18}$$

$$\eta'_{12} = \sum_{\mu\alpha\beta\gamma} \frac{\chi_c^{-1} \iint \chi^{(3)}_{\mu\alpha\beta\gamma} e^{*(1)}_{\mu} e^{(2)}_{\alpha} e^{*(1)}_{\beta} e^{(2)}_{\gamma} dxdy}{\left[\iint \left(|\mathbf{e}^{(1)}|^2\right)^2 dxdy \iint \left(|\mathbf{e}^{(2)}|^2\right)^2 dxdy \right]^{1/2}}. \tag{3.19}$$

In optical fibers $\eta_{mm} \approx 1$, and $\eta_{12} \approx 1/3$.

Free-carrier parameters

The subscript on the quantities Δn_k^{fc} and $\Delta\alpha_k^{fc}$ indicate that they depend on the properties of the k^{th} mode, and are evaluated as overlap integrals with the free-carrier-induced changes in refractive index and absorption,

$$\Delta n_k^{fc} = \frac{n_0}{\overline{n}_k} \Gamma_k \frac{\iint \Delta n^{fc}(x,y) |\mathbf{e}^{(k)}|^2 dxdy}{\iint |\mathbf{e}^{(k)}|^2 dxdy}, \tag{3.20}$$

$$\Delta\alpha_k^{fc} = \frac{n_0}{\overline{n}_k} \Gamma_k \frac{\iint \Delta\alpha^{fc}(x,y) |\mathbf{e}^{(k)}|^2 dxdy}{\iint |\mathbf{e}^{(k)}|^2 dxdy}. \tag{3.21}$$

As indicated by the semi-empirical model of Eqs. (3.8), the free-carrier-induced changes are determined entirely by their number density $N(\mathbf{r}, t)$. In general N obeys the following equation at any location within the silicon region of the waveguide [92]:

$$\frac{\partial N}{\partial t} = G(\mathbf{r}, t) + D_\alpha \nabla^2 N - \frac{N}{\tau'_{fc}}. \tag{3.22}$$

In Eq. (3.22) G is the generation rate of electron-hole pairs that results from two-photon absorption, D_α is the ambipolar diffusion coefficient, and τ'_{fc} is the free-carrier lifetime of bulk silicon. Solving Eq. (3.22) is complicated by the fact that free carriers undergo much higher rates of recombination at the waveguide boundaries [93]. In order to circumvent this difficulty a simplifying assumption will be made in the analysis. The free-carrier density will be assumed to be spatially uniform throughout the silicon region and the enhanced recombination rate from the waveguide boundaries will be assumed to simply decrease the carrier lifetime. This assumption neglects

carrier diffusion, which causes the spatial profile of N to change in time, and hence contributes to temporal changes in the effective mode index [Eq. (3.20)]. The time period T_{diff} over which these diffusion-induced changes in effective index occur can be estimated by

$$T_{\text{diff}} = \frac{(\Delta x)^2}{16\ln(2)D_\alpha}, \tag{3.23}$$

where Δx is half of the smallest waveguide dimension (usually the waveguide height). Physically, T_{diff} is the time it takes for an electron-hole pair generated in the center of the waveguide to diffuse to the waveguide boundary. Eq. (3.23) was derived using the Gaussian impulse response of the diffusion equation [Eq. (3.22) without the generation and recombination terms]. Using $D_\alpha \approx 10$ cm^2/s from Ref. [94] and $\Delta x \approx 200$ nm gives an estimate of $T_{\text{diff}} \approx 3.6$ ps. Thus, for pulse widths that are comparable to 3.6 ps these diffusion-induced index changes may have an influence. Their contribution to the dynamic index change is expected to be negligible compared to the contributions from generation and recombination. A more detailed study is needed to verify how accurate this expectation is, but such a study will not be performed here. In this chapter the simplifying assumption will be taken as a reasonable approximation even for pulse widths comparable to T_{diff}. Its application leads to

$$\frac{dN}{dt} = G - \frac{N}{\tau_{fc}}, \tag{3.24}$$

where τ_{fc} is not the carrier lifetime of the bulk material but an effective lifetime for the waveguide that can be determined empirically. Typically τ_{fc} is ~1 ns. The generation rate from two-photon absorption is given by

$$G = \frac{r}{A_c\hbar\omega_0}\left(\gamma_{11}|A_1|^4 + \gamma_{22}|A_2|^4 + 2\gamma_{12}|A_1A_2|^2\right), \tag{3.25}$$

where A_c is the cross-sectional area of the waveguide (width × height). With the approximation that the free-carrier density is uniform in the silicon region, the effective changes in the modal index and absorption in Eqs. (3.20) and (3.21) reduce to

$$\Delta n_k^{fc} = \Pi_k \Delta n^{fc}, \tag{3.26}$$

$$\Delta \alpha_k^{fc} = \Pi_k \Delta \alpha^{fc}, \tag{3.27}$$

where the *index enhancement factor* Π_k depends on the properties of the mode,

$$\Pi_k = \Gamma_k \frac{n_0}{\overline{n}_k} \frac{\iint_{Si} |\mathbf{e}^{(k)}|^2 \, dxdy}{\iint |\mathbf{e}^{(k)}|^2 \, dxdy}, \tag{3.28}$$

and the integration in the numerator is over the silicon core. Taken together, Eqs. (3.8) and (3.24)-(3.28) provide a complete description of the influence of free carriers.

Note that the theory of this section has been developed entirely in terms of the electric field $\mathbf{e}(x, y)$. The magnetic field $\mathbf{h}(x, y)$ was eliminated from the equations by the relation

$$N_k = \frac{\beta_0^{(k)}}{2\omega_0\mu_0} \iint |\mathbf{e}_T^{(k)}|^2 + (\beta_0^{(k)})^{-1} \mathrm{Im}\left\{\mathbf{e}_T^{(k)} \cdot \nabla_T e_z^{*(k)}\right\} \, dxdy, \tag{3.29}$$

which can be derived by applying Eq. (2.7) to definition (2.27).

3.1.4 A physical explanation for longitudinal enhancement of nonlinearity

According to Eqs. (3.15) the presence of a significant longitudinal electric field component enhances the waveguide's nonlinearity via the longitudinal enhancement factor, Γ_k. It is not immediately obvious why this should be the case. Consider the following expression for the group velocity of the k^{th} mode ($v_g^k = 1/\beta_1^{(k)}$) [68, 95] :

$$v_g^k = \frac{\frac{1}{2} \iint \mathrm{Re}\left\{\left(\mathbf{e}_T^{(k)} \times \mathbf{h}_T^{*(k)}\right) \cdot \hat{\mathbf{z}}\right\} \, dxdy}{\frac{1}{4} \iint \mu_0 \left|\mathbf{h}^{(k)}\right|^2 + \epsilon_0 \epsilon \left|\mathbf{e}^{(k)}\right|^2 \, dxdy}. \tag{3.30}$$

The numerator of the right hand side of Eq. (3.30) is the optical power, and the denominator is the electromagnetic energy per unit distance. Equation (3.30) therefore states that the group velocity is equal to the velocity at which energy flows. Significant for our purposes is that the optical power depends only on the transverse field components whereas the energy density depends on all of the field components. An enhancement of the longitudinal electric field component therefore increases the energy density but has no effect on the optical power. Thus, enhancement of e_z is correlated with a reduction of the group velocity. Longitudinal enhancement of the nonlinearity can therefore be understood as a slow-light enhancement of nonlinearity, a phenomenon that was first noted for silicon waveguides in Ref. [37].

3.1.5 Comparison with other theories in the literature

In the case that only one mode is excited [e.g. if $A_2 = 0$ in Eqs. (3.13) and (3.14)] then a comparison can be made between the theoretical formalism developed here and other theories in the literature that also take into account the vectorial nature of the waveguide modes. Reference [37] presents such a theory for describing the Raman interaction between a pump wave and a Stokes wave, each propagating in a single spatial mode of a silicon waveguide. Their theory takes into account the Kerr effect, two-photon absorption, free carrier nonlinearities and the Raman interaction. In the special case where the Stokes wave is not present their theory can be shown to be in agreement with the one presented here. In Ref. [37] expressions for the nonlinear parameters are formulated in a different (but equivalent) way, and a demonstration of this equivalence requires theorems regarding waveguide modes that can be found, for example, in Ref. [68].

Another study of nonlinear propagation that takes into account the vectorial nature of waveguide modes is presented in Ref. [41]. The emphasis of that study was on glass waveguides and free-carrier effects were not taken into account. Expressions (3.15) agree with the nonlinear parameters derived in that work if we take $\rho = 1$ in Eq. (3.3). If we further make the scalar approximation Eqs. (3.15) reduce to the familiar expressions from nonlinear fiber optics [29].

3.2 Dependence of waveguide parameters on device dimensions

The theoretical model developed in section 3.1 clarifies the relevant parameters that determine how an optical field will propagate through a silicon waveguide. In this section we seek to understand how device geometry will influence propagation by studying how these parameters depend on waveguide dimensions, particularly in the subwavelength regime. In 3.2.1 the dependence of the dispersion parameters of the fundamental TE and TM modes on waveguide dimensions is studied, with an emphasis on dispersion engineering in the subwavelength regime. In 3.2.2 the dependence of nonlinear parameters on waveguide dimensions is considered.

The calculations presented in this section use the numerical method of Ref. [96] for determining the propagation constants ($\beta^{(k)}$) as well as the vectorial mode profiles [$\mathbf{e}^{(k)}(x,y)$]. By calculating the propagation constants at multiple wavelengths and numerically differentiating, the dispersion parameters $\beta_n^{(k)}$ are determined. The mode profiles are used to numerically calculate the various nonlinear parameters discussed in section 3.1. The numerical technique of Ref. [96] is a finite-difference method, meaning that it partitions the cross-sectional geometry of the waveguide into a number of rectangular regions over a finite calculation window. In the calculations the numerical step size in the waveguide core ranges from 3-20 nm, depending on the waveguide dimensions considered. The step size is increased on the outside edge of the cladding region in order to increase the size of the calculation window. The resulting window ranges in size from 6.3-42 μm, depending on the waveguide geometry. One of the downsides of the numerical technique is that it does not provide any rigorous criteria for whether or not a given mode exists. However, if the area of the calculation window is much larger than the effective mode area calculated from Eq. (3.16) and the effective index is larger than the cladding index, it can be concluded that the mode found by the numerical technique really exists.

Rectangular silicon waveguides are considered here as depicted in Fig. 3.1. It is common in experiments to employ either waveguides that are exposed to air on top [102], or which are surrounded on all sides by silica [101], but we will consider only the latter since they are less sensitive to environmental influence and therefore more likely to be used in future applications. The results obtained, however, apply qualitatively to other geometries as well. The material dispersion of silicon and silica are both taken into account using Sellmeier relations from Ref. [32].

3.2.1 Dispersion parameters

Dispersion parameters play an important role in nonlinear processes in silicon waveguides, particularly for those involving widely separated frequencies such as four-wave mixing and supercontinuum generation [97–99]. It was noted as early as 2004 that when cylindrical silicon wires have subwavelength dimensions both the group index ($n_g = c/v_g = c\beta_1$) and group-velocity dispersion parameter (β_2) take on large values and depend strongly on the wire diameter [100]. Some early studies of dispersion

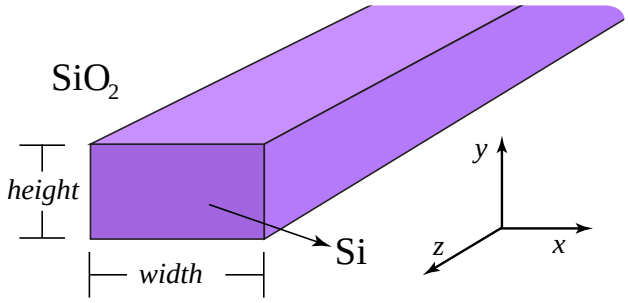

Figure 3.1: Schematic of the waveguide geometry. The silicon core is surrounded on all sides by silica. The TE and TM modes have dominant polarization components along the x and y directions, respectively.

engineering in rectangular silicon waveguides also noticed this strong dependence of dispersion parameters in the subwavelength regime [101, 102], although not much attention was paid to this phenomenon as the focus of these studies was either obtaining anomalous dispersion in the 1.55 μm wavelength regime [101, 103] or developing experimental techniques for measuring these parameters [101, 102, 104, 105]. A work by the author [106] studied this phenomenon in more detail for rectangular waveguides and contributes to this section.

Polarization-mode dispersion

Figure 3.2(a) plots the group index of the TM mode n_g^{TM} versus waveguide width and height for a free-space wavelength of 1550 nm. The group index of the TM mode depends strongly on the waveguide height but only weakly on its width. For a relatively large height $n_g^{TM} \approx 3.7$, but as the height is reduced to the effective wavelength inside the core material ($\lambda/n_0 \approx 440$ nm) it begins to increase dramatically. When the height approaches 300 nm the group index peaks at about 4.5 and then decreases significantly with further reduction. The results in Fig. 3.2(a) are in good agreement with the experimental measurements of group index reported in Refs. [101, 105].

Note that, as a result of an inherent symmetry in the device, the dependence of the group index of the TE mode is identical to the plot of Fig. 3.2(a) when the waveguide width and height are interchanged. Excepting the special case of perfectly square

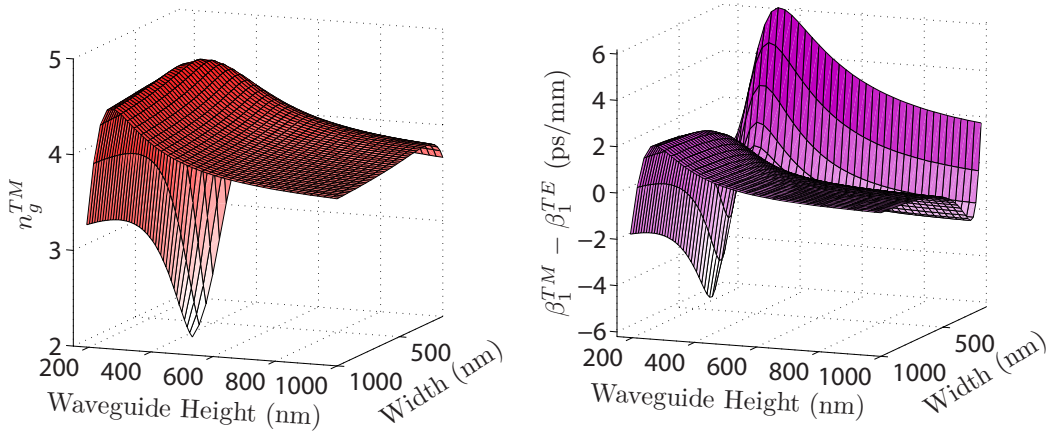

(a) (b)

Figure 3.2: Dependence of (a) the group index of the TM mode and (b) The differential group delay between the TE and TM modes on waveguide dimensions at the 1550 nm wavelength.

waveguides, this implies that the fundamental TE and TM modes will propagate at different speeds. This phenomenon is known as polarization-mode dispersion (PMD). PMD is characterized by the differential group delay (DGD), which is defined as $\beta_1^{TM} - \beta_1^{TE}$ and is the temporal walk-off per unit distance between the TE and TM modes. The DGD is plotted in Fig. 3.2(b) versus waveguide width and height. Note that, as expected, it is identically zero for square waveguides of any dimension. For non-square rectangular waveguides (most commonly employed) it is relatively small when dimensions are larger than λ/n_0. This situation is changed as, for example, the waveguide height is reduced below λ/n_0 and reaches a local maximum larger than 2 ps/mm when the height is near 300 nm. Further reduction of the waveguide height causes the DGD to drop dramatically back to zero and then to negative values. Perhaps most striking about this behavior from an experimental point of view is that the DGD can become practically significant since typical pulse widths used are of the order of 1 ps and typical waveguide lengths are of the order of 1 mm. As a result, the DGD of waveguides with subwavelength dimensions can induce dramatic changes in the polarization properties of optical pulses. This will be studied in more detail in chapter 4.

Group-velocity dispersion

The higher order dispersion parameters (β_n, where $n \geq 2$) can be collectively referred to as group-velocity dispersion (GVD) parameters. Of these, β_2 has the most influence on the optical field. Figures 3.3(a) and 3.3(b) plot β_2 for the fundamental TE and TM modes (β_2^{TE} and β_2^{TM}, respectively) versus waveguide width and height at a free-space wavelength of 1550 nm. The results are in good agreement with the measured values reported in Ref. [101]. For waveguides with dimensions > 800 nm the GVD is relatively small and normal ($\beta_2 > 0$) for both modes. As the waveguide width is reduced below 800 nm the dispersion of the TE mode becomes anomalous ($\beta_2^{TE} < 0$) and remains relatively small until the width approaches λ/n_0. For waveguide widths < 300 nm the dispersion becomes both normal and extremely large, and values of β_2^{TE} as high as 25 ps^2/m can be reached. Note that, as expected, the dependence of β_2^{TM} on waveguide height is identical to the dependence of β_2^{TE} on waveguide width.

The propagation of femtosecond pulses in silicon waveguides is highly sensitive to whether $\beta_2 > 0$ or $\beta_2 < 0$, and soliton-like behavior can be observed in the latter case [99, 107]. Other kinds of nonlinear phenomena, such as four-wave mixing and supercontinuum generation, are highly sensitive to having one or more dispersion parameters extremely small or zero [97–99]. For these reasons it is useful to consider

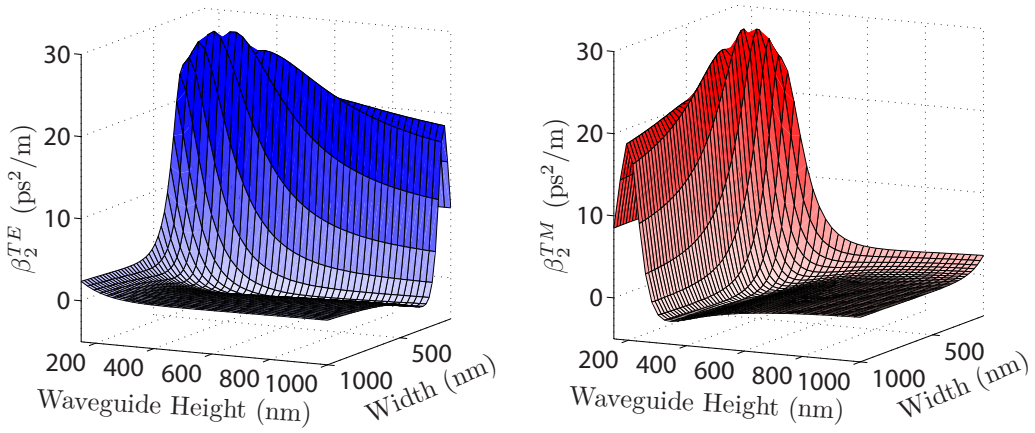

(a) (b)

Figure 3.3: Group-velocity dispersion parameters of (a) the TE and (b) the TM modes versus waveguide dimensions (λ = 1550 nm).

the waveguide geometries for which dispersion parameters are equal to zero. Figure 3.4(a) shows contours in the width-height plane along which β_2^{TE}, β_3^{TE}, or β_4^{TE} vanish. The tongue-shaped contour (solid line) represents the geometries for which $\beta_2^{TE} = 0$. Inside of this region the GVD is anomalous, and outside of this region it is normal. Dashed and dashed-dotted curves similarly delineate the regions above which $\beta_3^{TE} > 0$ and $\beta_4^{TE} < 0$, respectively.

The bandwidth of devices based on four-wave mixing does not depend on β_3, but depends primarily on the values of β_2 and β_4 [29]. For maximizing the bandwidth, the values of both of these parameters should be near to zero. Figure 3.4(a) demonstrates that a single waveguide geometry exists that meets this requirement, namely one with a width ≈ 710 nm and a height ≈ 265 nm. This explains the results of Ref. [97]. In that study, four different waveguide geometries were used in a four-wave mixing experiment with a pump wavelength at 1550 nm. The effective bandwidth observed in the TE mode correlated with how close the device geometry was to the optimal one indicated by Fig. 3.4(a). The waveguide geometry closest to this optimal one had a width of 650 nm and a height of 300 nm and exhibited the largest bandwidth of those studied in the experiment. This same research group later realized that such an optimal

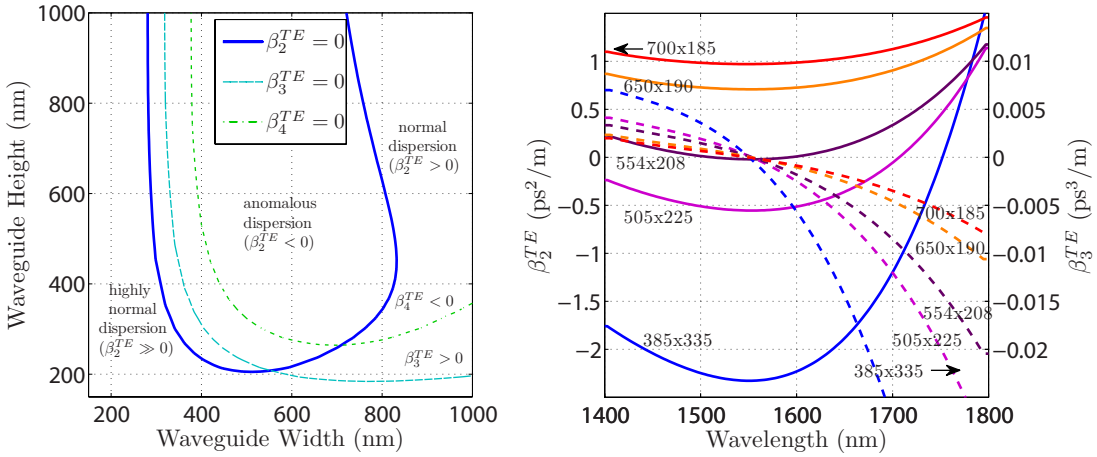

Figure 3.4: (a) Contours in the (*width*, *height*) plane along which various dispersion parameters vanish for the TE mode at the 1550 nm wavelength. (b) Dispersion curves for various waveguide geometries which lie along the $\beta_3^{TE} = 0$ contour in (a).

geometry exists, and reported frequency conversion over two-thirds of an octave by using it [98]. The device they used had a width of 700 nm and a height of 300 nm, which is different from the one indicated by Fig. 3.4(a) because their waveguide was slightly ribbed and not perfectly rectangular.

Another interesting geometry is the one with a width of 504 nm and a height of 208 nm. For this geometry β_2^{TE} and β_3^{TE} simultaneously vanish, indicating that β_2^{TE} is near zero over a broad spectral region centered at 1550 nm. This is shown in Fig. 3.4(b) where β_2^{TE} is plotted for this geometry over a range of wavelengths, indicating that it is vanishingly small over a spectral region at least 100 nm wide. Also plotted in Fig. 3.4(b) is β_2^{TE} for a number of other 'dispersion-flattened geometries' lying along the $\beta_3^{TE} = 0$ contour. The waveguide can be engineered to have a range of either normal or anomalous nominal values over a broad spectral region centered at 1550 nm. Similar designs can be found for other spectral regions by reproducing a $\beta_3^{TE} = 0$ contour like the one of Fig. 3.4(a) at the desired wavelength.

3.2.2 Nonlinear parameters

Third-order nonlinearity

In section 3.2.1 it was found that the dispersion parameters of a mode depend strongly on the waveguide dimension that is parallel to its primary polarization direction but only weakly on the orthogonal dimension. By contrast, the overall nonlinear (γ) parameter depends only weakly on the dimension along which it is polarized and strongly on the orthogonal one. This is evident in Fig. 3.5 where the nonlinear parameters for the fundamental TE (γ_{11}) and TM (γ_{22}) modes of the waveguide depicted in Fig. 3.1 are plotted versus width and height. As can be seen from Fig. 3.5(a), γ_{11} depends strongly on the waveguide height but only weakly on its width. Because of an inherent symmetry the dependence of γ_{22} in Fig. 3.5(b) is qualitatively similar except that the roles of width and height are reversed. Note that, as a result of nonlinear anisotropy, this is only a qualitative similarity and there are quantitative differences.

The underlying reason why the nonlinear parameters depend on waveguide dimensions as they do is the polarization dependence of modal confinement. Conceptually, the confinement of a mode to the core depends strongly on the waveguide dimension

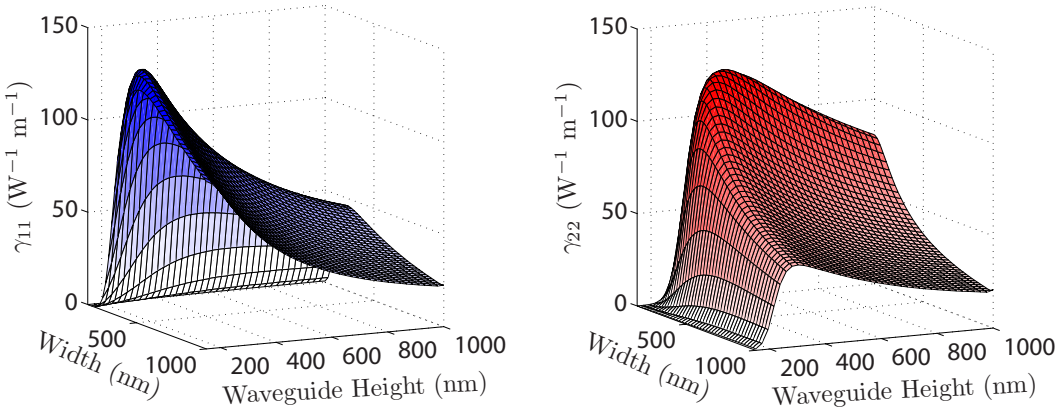

(a) (b)

Figure 3.5: Overall nonlinear parameters of (a) the TE and (b) the TM modes versus waveguide dimensions (λ = 1550 nm).

along which it is polarized. This is evident from Fig. 3.6(a) where the effective mode areas of the TE and TM modes are plotted versus waveguide height for a fixed width of 500 nm. The effective area of the TE mode (dashed curve) scales proportionately with the waveguide height (and hence to the cross-sectional waveguide area). The effective area of the TM mode, however, only exhibits this behavior for waveguide heights $\gtrsim \lambda/n_0$. As the waveguide height is reduced below λ/n_0 the effective area begins to increase as it looses its confinement to the core and evanesces into the cladding.

Other parameters in Eqs. (3.15) that are directly related to modal confinement are the nonlinear overlap factors (η_{lm}). A mode that is tightly confined to the core material will have a nonlinear overlap factor ≈ 1. To the extent that a mode evanesces into the silica cladding its overlap factor will be reduced from 1 since the nonlinearity of silica is about two orders of magnitude weaker than that of silicon. Figure 3.6(b) shows this to be the case. Here the η parameters are plotted versus waveguide height for the fixed width of 500 nm. For a height $\gtrsim \lambda/n_0$ both η_{11} and η_{22} are close to 1. As the height is reduced below λ/n_0, η_{22} begins to decrease rapidly and becomes as small as ~0.2 when the waveguide height approaches a value at which the TM mode can no longer be considered to exist (at $\sim \lambda/2n_0$). η_{11}, by contrast, remains relatively close to 1 as the TE mode is tightly confined to the core even for subwavelength waveguide

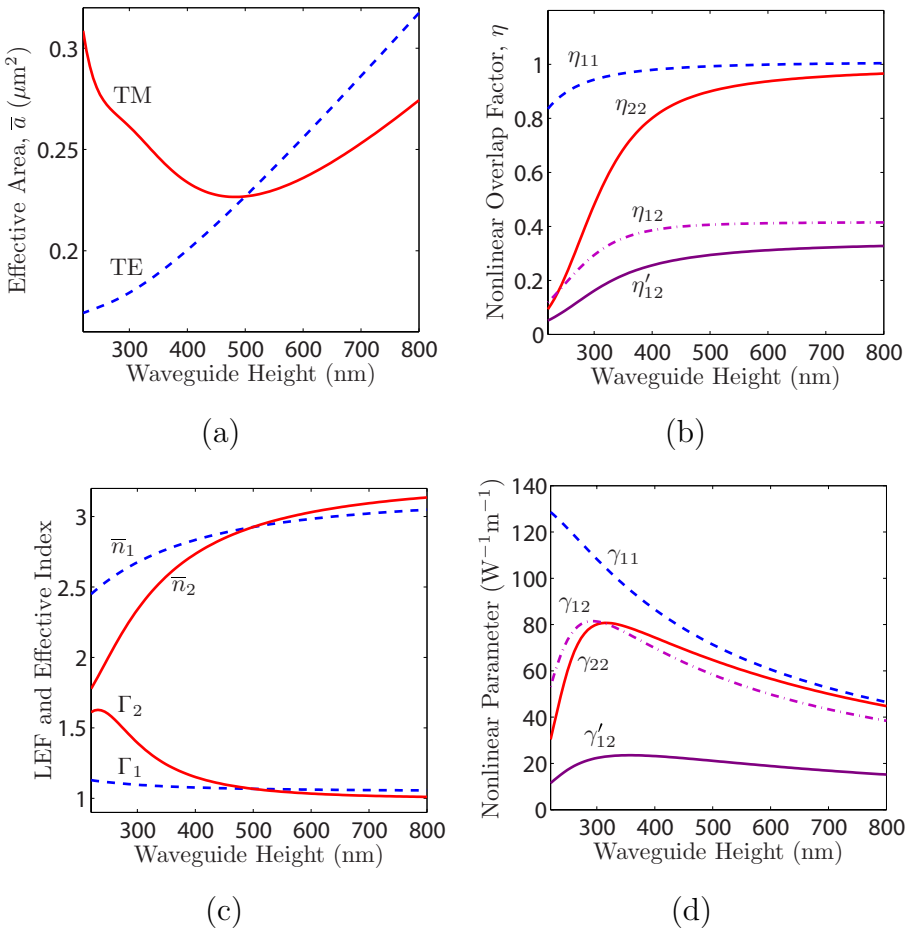

Figure 3.6: Various parameters contributing to the overall nonlinear (γ) parameters versus waveguide height when the width is fixed at 500 nm. (a) The effective mode areas of Eq. (3.16) for the TE and TM modes; (b) the nonlinear overlap factors of Eqs. (3.19); (c) The longitudinal enhancement factors of Eq. (3.17) and the effective mode indices; (d) The overall nonlinear parameters given by Eqs. (3.15). All of these plots are at the 1550 nm wavelength.

heights. Notice that, even when the waveguide is square (height = 500 nm), η_{11} is larger than η_{22} by about 15 % as a result of the nonlinear anisotropy of silicon [86].

Whereas $\overline{a}_2$ and η_{22} both act to reduce the TM mode's nonlinearity for subwavelength heights, the longitudinal enhancement factor Γ_2 and effective mode index $\overline{n}_2$ both act to enhance it. These are plotted in Fig. 3.6(c) for both the TE and TM modes. When the waveguide height $\gtrsim \lambda/n_0$ both of the longitudinal enhancement

factors (Γ_1 and Γ_2) are ≈ 1. As the waveguide height is reduced to the subwavelength regime, Γ_2 increases as a result of an enhanced longitudinal field component. Figure 3.6(c) indicates that this enhancement can be by as much as 60 %. Also indicated by Fig. 3.6(c) is that the TM mode's effective index $\overline{n}_2$ begins to drop off rapidly when the height $< \lambda/n_0$. Physically, when the TM mode evanesces into the cladding it has a greater degree of overlap with the lower-index material in the waveguide (silica in this case), causing a reduction in its effective index. Since the nonlinear parameter γ_{22} is directly proportional to $1/\overline{n}_2^2$ and Γ_2^2 both of these parameters enhance it in the subwavelength regime.

Since, in the subwavelength regime, the effective mode area and nonlinear overlap factor both act to reduce the nonlinearity whereas the longitudinal enhancement factor and effective index both act to enhance it, their overall influence is determined by their cumulative effect. Figure 3.6(d) shows the overall dependence of the nonlinear parameters on waveguide height. As the waveguide height is reduced below λ/n_0, γ_{22} initially continues to increase as a result of an increasing longitudinal enhancement factor and decreasing effective mode index. When the height reaches about 300 nm the evanescence of the mode into the cladding becomes the dominant effect and ultimately reduces the nonlinear parameter. The TE mode's nonlinear parameter, γ_{11}, monotonically increases throughout this reduction as a result of its tight confinement to the silicon core and decreasing effective area.

Free-carrier nonlinearity

The influence of free carriers that have been generated by two-photon absorption also depends on waveguide dimensions. According to Eqs. (3.26)-(3.28) this influence can be characterized by the index enhancement factor, Π_k, which is plotted in Fig. 3.7 versus waveguide height for the TE and TM modes. For heights > 300 nm, the proportionality constants are relatively independent of waveguide dimensions and approximately equal for the two modes. When the waveguide height is reduced to < 300 nm, the TM mode's index enhancement factor begins to drop off dramatically as it evanesces into the cladding and overlaps only weakly with the free carriers concentrated in the core. The implication of this is that, for subwavelength heights, free carriers change not only the refractive index but also the waveguide birefringence.

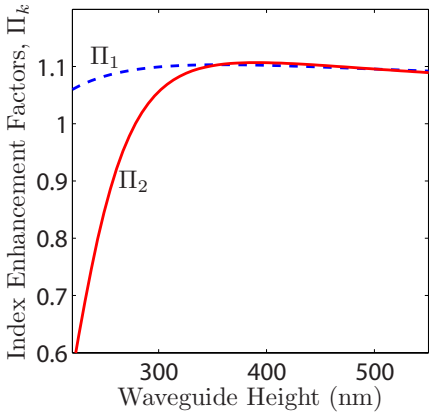

Figure 3.7: Free-carrier index enhancement factors of Eq. (3.28) for the TE and TM modes versus waveguide height for a fixed width of 500 nm at the 1550 nm wavelength.

This change in birefringence is given by $(\Pi_1 - \Pi_2)\,\Delta n^{fc}$ and can be as much as 30% of the overall change in refractive index according to Fig. 3.7.

3.3 Summary

In this chapter a comprehensive theory of nonlinear propagation in silicon waveguides was developed, which incorporates the polarization dependence of the optical field by describing the coupling that can occur between the TE and TM modes and is valid for waveguides with subwavelength dimensions since it takes into account their vectorial nature. The Kerr effect, two-photon absorption, and free-carrier nonlinearities are included, as well as linear effects such as PMD and GVD. It was found that propagation parameters have a dramatic dependence on waveguide dimensions in the subwavelength regime. Linear parameters describing PMD and GVD were found to be highly sensitive to the waveguide dimension along which a mode is dominantly polarized, but only weakly dependent on the orthogonal dimension. The dependence of a mode's overall nonlinear parameter (γ) was found to be opposite to that of its linear parameters, being sensitive to the waveguide dimension orthogonal to its polarization direction but exhibiting a relatively weak dependence on the parallel dimension. By studying the individual factors contributing to the overall nonlinear parameters independently it was found that they each, like the linear parameters, depend strongly on

the parallel dimension and weakly on the orthogonal one. Because they have a competing influence on the mode's overall nonlinear parameter this strong dependence of the modal properties on the parallel dimension is veiled when only the γ parameters are considered.

4 Nonlinear propagation in silicon waveguides: polarization effects

Polarization effects were largely ignored in studies of nonlinear optics in silicon waveguides until 2009 [108]. At that time it was realized that if a probe beam is made to propagate in both the TE and TM modes, rather than in only a single spatial mode, then a linearly polarized pump beam can modulate its polarization state through cross-phase modulation. When combined with an analyzer at the waveguide output this configuration becomes an all-optical switch. This concept was later demonstrated experimentally [91], and also analyzed in more detail theoretically [109, 110]. Studies of self-phase modulation incorporating the polarization properties of the field in silicon waveguides [83–85] as well as bulk silicon [110, 111] have also been reported recently. Of these two were works of the author [84,85] and contribute to this chapter.

This chapter presents an experimental and theoretical study of polarization effects related to self-phase modulation in silicon waveguides. In chapter 3 it was determined that waveguides having a dimension smaller than the effective wavelength (λ/n_0) can have significantly different properties than their larger counterparts. In particular, when only one dimension is smaller than λ/n_0, both the linear and nonlinear properties can become significantly different between the TE and TM modes. This can lead to significant PMD, as well as significantly different GVD, Kerr nonlinearity, and free-carrier nonlinearity. For the geometries considered in this chapter it is the influence of a strong waveguide-induced PMD which will have the most impact on self-phase modulation. In section 4.1 the experimental setup is described. Section 4.2 presents a study of the combined influence of PMD and self-phase modulation on the spectral properties of optical pulses in silicon waveguides. Section 4.3 considers the

influence of PMD on the temporal properties of an optical pulse undergoing self-phase modulation.

4.1 Experimental setup

The silicon waveguides used in the experiments are designed to have a width of 600 nm and a height of 400 nm. They're fabricated from a 400 nm thick layer of silicon resting on a 3 μm thick layer of silicon dioxide, and are left exposed to air on top (the inset of Fig. 4.1 shows the device geometry). They were patterned using electron-beam lithography and cut using reactive-ion etching, and their input and output facets are equipped with inverse-taper polymer mode converters for improved coupling efficiency. The waveguides are from the same chip used in Ref. [91] and further details of their fabrication can be found there. The propagation losses were estimated as 10±2 dB/cm for both the TE and TM modes [91]. Two different waveguides were used in the experiments, having lengths of 3 mm and 8 mm. The overall fiber-to-fiber insertion loss was measured for each of the waveguides for both the TE and TM modes. The measured values are reported in Table 4.1. The values in the table show no clear trend. The overall insertion loss of the 8 mm waveguide is roughly comparable to that of the 3 mm waveguide, even though it is expected to have higher propagation losses. In the case of the 3 mm waveguide the TE mode exhibits the greater insertion loss, but for the the 8 mm waveguide it is the TM mode that exhibits the greater loss. The most likely reason for these variations is that the input coupling efficiency (from the fiber to the waveguide), as well as the output coupling efficiency (back into the fiber), are both sensitive to minor variations in the fabricated inverse-taper polymer couplers. As a result, neither the input coupling efficiency nor the output coupling efficiency of either waveguide is precisely known.

	TE	TM
3 mm waveguide	16.2 dB	15.6 dB
8 mm waveguide	15.5 dB	17.7 dB

Table 4.1: Overall fiber-to-fiber insertion losses of the waveguides used in the experiments. The waveguides have the same transverse dimensions but different lengths.

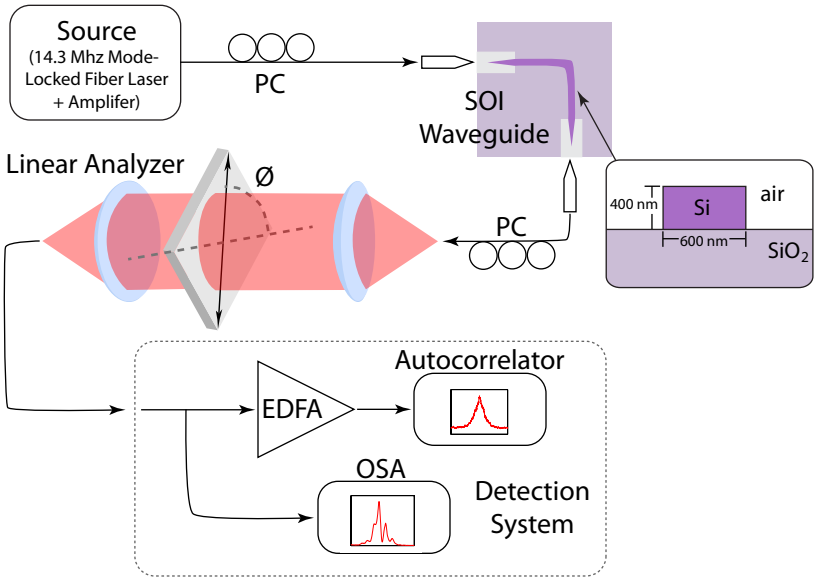

Figure 4.1: The experimental setup. pulses from a mode-locked laser are coupled into a silicon waveguide. The output pulses are passed through a rotatable linear analyzer, which isolates either the TE mode ($\phi = 0$), the TM mode ($\phi = \pi/2$), or some combination of the two, depending on its orientation. The inset shows the transverse geometry of the waveguides.

Figure 4.1 shows a schematic of the experimental setup. The source of optical pulses is a mode-locked, erbium-doped fiber laser operating at a 14.3 MHz repetition rate at the 1560 nm wavelength. Details about the source and its construction are provided in appendix B. The pulses from the laser have a temporal width of ~2.7 ps (full-width at half maximum) and a peak power of ~50 W. They are passed through a fiber-based polarization controller (PC) to adjust their polarization at the waveguide input. They're coupled into the waveguide using a lensed tapered fiber, and then coupled from the waveguide output back into fiber using a second lensed tapered fiber. They are then passed through a second PC before being coupled into free space, passed through a rotatable linear analyzer, and coupled back into fiber again. This second PC is adjusted so that when the analyzer is oriented at an angle $\phi = 0$ the output from the TE mode is passed and the output from the TM mode is extinguished, whereas the opposite occurs for an angle $\phi = \pi/2$. The properties of the pulses after the analyzer are measured by both an optical spectrum analyzer (OSA) and by an autocorrelator.

Before autocorrelation it is necessary to amplify them using an erbium-doped fiber amplifier (EDFA). In the experiment there was no indication that higher-order modes were being excited in the waveguide and the transmission is believed to be dominated by the fundamental TE and TM modes.

The polarization state of the pulses depends on the relative phase between the TE and TM modes. This relative phase varies rapidly along the length of the waveguide as a result of its large birefringence. The weakly-birefringent PC after the waveguide makes an additional contribution to the relative phase before the pulses pass through the analyzer. When the analyzer is oriented at $\phi = 0$ or $\phi = \pi/2$ the relative phase has no bearing on the measured spectrum or autocorrelation. For other analyzer orientations this is not the case. If, for instance, the analyzer is oriented at $\phi = \pm\pi/4$ then any oscillations in this relative phase (i.e. polarization oscillations) induced by the waveguide will manifest as oscillations in the measured intensity profile after the analyzer.

Control experiment

Before any changes in the spectral or temporal properties of the pulses can be attributed to the silicon waveguides it should be verified that the rest of the experimental setup (PC's, lensed fibers, analyzer, etc.) is not the cause of these changes. A control experiment was performed for this purpose. In the control experiment the waveguide was removed and the two lensed fibers were aligned so that light coupled directly from one to the other with an insertion loss comparable to when the waveguide is present (it was about ~13 dB in the control experiment). Figure 4.2(a) shows the spectrum of the source before and after it had been transmitted through the control arrangement (denoted by A and B, respectively). The transmission spectrum through the control arrangement is an exact replica of the source spectrum (it has been scaled to be the same magnitude in the figure), indicating a complete absence of nonlinear effects from the optical fiber, the PCs, the lensed fibers, and the analyzer.

Figure 4.2(b) shows an autocorrelation measurement of the source both before and after passing through the control arrangement (A and B, respectively). The pulses appear to have been temporally broadened by the control arrangement, but this appearence is deceptive. Because A was directly measured from the high-power

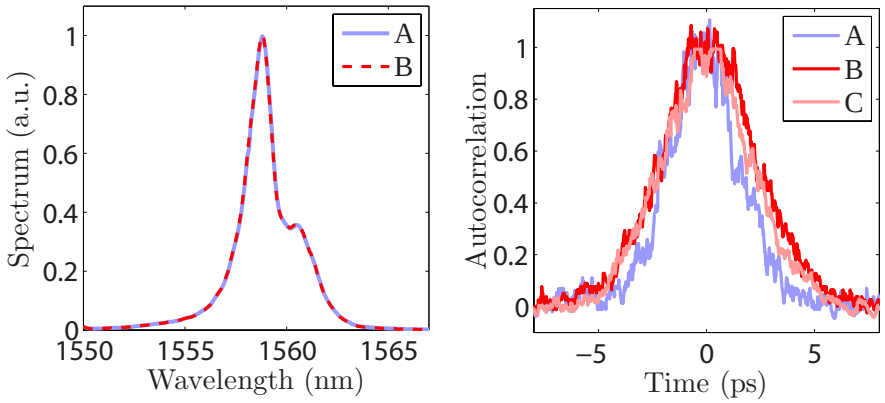

(a) (b)

Figure 4.2: The results of a control experiment. 'A' indicates the pulses from the mode-locked laser source. 'B' indicates the same pulses after having been passed through the experimental setup, but without the silicon waveguide. 'C' indicates the source pulses after being attenuated and subsequently amplified by the EDFA shown in Fig. 4.1. (a) and (b) show the spectra and autocorrelations, respectively.

source pulses, the EDFA was not used before the autocorrelator in that case. In B, however, significant loss imposed by the control arrangement necessitated the use of the EDFA. A third measurement was made in which the source was attenuated and then passed through the EDFA before autocorrelation, which is shown as C in Fig. 4.2(b). C clearly shows that the EDFA is the primary cause for the temporal broadening shown in B. B is, however, slightly broader than C, indicating some minor dispersion in the control arrangement.

Theoretical model of the source

The experimental results will be modeled by solving Eqs. (3.13) and (3.14) for the TE and TM modes in the waveguide. This is done by using the symmetric split-step method [29], which requires a specification of the TE and TM pulse amplitudes at the waveguide input [$A_1(0,t)$ and $A_2(0,t)$, respectively]. These are related to the source pulses $A_{in}(t)$ by

$$A_1(0,t) = \sqrt{\zeta_1}A_{in}(t), \tag{4.1}$$

$$A_2(0,t) = \sqrt{\zeta_2}A_{in}(t)e^{i\delta}, \tag{4.2}$$

where ζ_k is the fraction of power coupled into mode k and δ is the relative phase between the modes. ζ_k is determined by both the mode's insertion loss and the polarization state of the input pulse, whereas δ is determined entirely by the polarization state. The model used for $A_{in}(t)$ assumes a Gaussian intensity profile, but allows for the possibility of self-phase modulation induced chirp from an internal amplifier (see appendix B). Thus the input field is given by

$$A_{in}(t) = \sqrt{P_0}\, e^{-\frac{1}{2}(t/T_0)^2 + i\phi_m |A_{in}|^2/P_0}, \tag{4.3}$$

where P_0 is the peak power, T_0 is the pulse duration, and ϕ_m is the maximum nonlinear phase shift [29]. Figures 4.3(a) and 4.3(b) compare the actual spectrum and autocorrelation of the input pulses with those of a pulse given by Eq. (4.3) when T_0 = 1.6 ps and ϕ_m = 2. The relative good agreement suggests that this is a sufficient model for the purposes of this chapter. The feature on the red side of the measured pulse spectrum in Fig. 4.3(a) is likely due to asymmetric spectral gain from the internal amplifier, and will not be taken into account in the theory.

For a waveguide of length L, the autocorrelations and spectra measured after the analyzer are modeled by the amplitudes $A_1(L,t)$ and $A_2(L,t)$ for the TE and TM modes, respectively. When the analyzer orientation is adjusted to $\phi = \pm\pi/4$, the fields

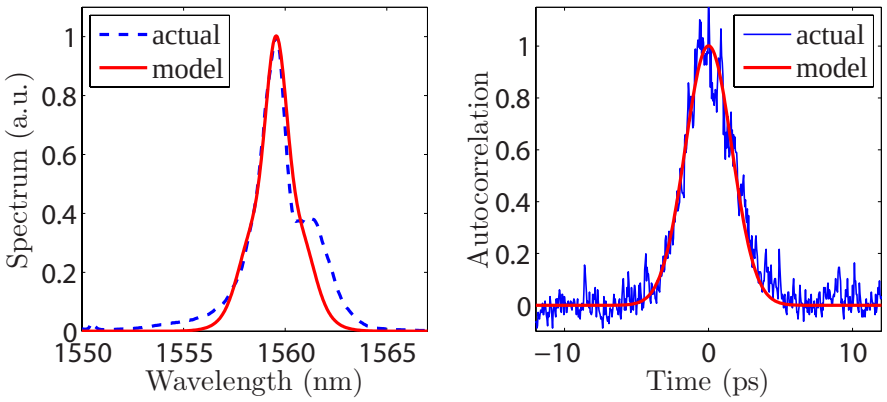

Figure 4.3: Comparison of the model of the source expressed in Eq. (4.3) with the measured (a) spectrum and (b) autocorrelation.

after the analyzer are related to the TE and TM fields by

$$A_{\pm\pi/4} = \frac{1}{\sqrt{2}}\left(A_2\, e^{i\delta'} \pm A_1\right), \tag{4.4}$$

where the relative phase δ' can be used as a fitting parameter.

4.2 Self-phase modulation and spectral polarization oscillations

8 mm waveguide measurements

Figure 4.4(a) shows the spectrum at the output of the 8 mm waveguide when the input pulses are polarized to excite only the TE mode. In the figure the spectra denoted by 'TE' and 'TM' correspond to analyzer orientations $\phi = 0$ and $\phi = \pi/2$, respectively. The TE spectrum is significantly broadened as compared with that of the input pulses in Fig. 4.3(a) and shows a multipeak structure that is characteristic of self-phase modulation. This multipeak structure is caused by spectral interference, which occurs when the same frequency component exists at multiple distinct times within a pulse [29]. In silicon waveguides the Kerr effect acts to chirp the pulse and broaden its spectrum in a fashion that is more or less symmetric (depending on the pulse shape), whereas free carriers created by two-photon absorption impose a definitive blue shift [82]. The broadened spectrum of Fig. 4.4(a) appears almost symmetric, but does exhibit a subtle blue shift. This is evident from the bluest peak near 1558 nm being slightly higher and broader than the reddest peak at 1562 nm.

Figure 4.4(b) shows how the measured spectrum changes when the analyzer orientation is adjusted to $\phi = \pm\pi/4$. Both spectra are replicas of the TE spectrum in Fig. 4.4(a), except that their peak values are lower. This is expected since, in the absence of a TM pulse, the fields in the $\pm\pi/4$ polarization states at the analyzer are simply related to the TM field as $A_{\pm\pi/4} = \pm A_1/\sqrt{2}$, as indicated by Eq. (4.3).

Figures 4.4(c) and 4.4(d) show the output spectra in each of the four analyzer orientations when the input pulse polarization is adjusted to excite both the TE and TM modes in the waveguide. In Fig. 4.4(c) both the TE and TM spectra exhibit the characteristic multipeak structure of self-phase modulation. The TM spectrum

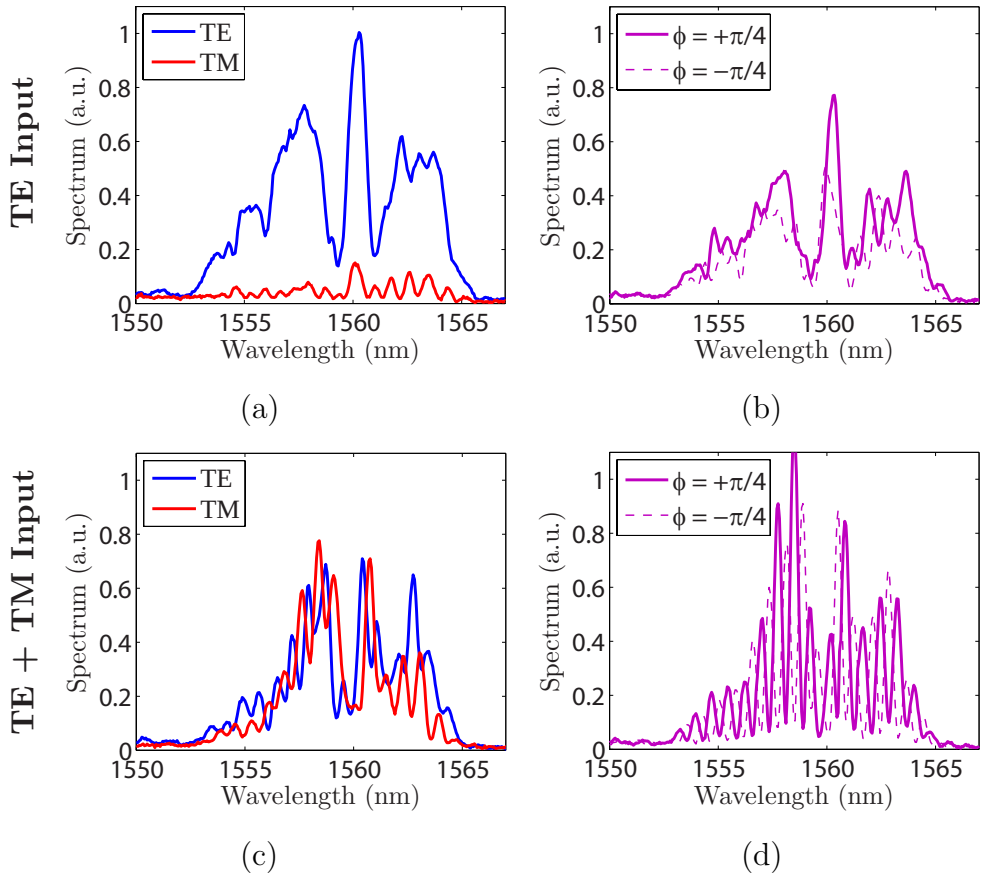

Figure 4.4: Measured output spectra of the 8 mm waveguide for two different input polarizations. (a) and (b) show the output spectra in each of the four analyzer orientations when the input polarization is adjusted to excite only the TE mode. (c) and (d) show the output spectra when the input polarization is adjusted to excite both the TE and TM modes.

exhibits a slightly stronger blue shift. This is understood to result from the asymmetry of Kerr-induced cross-phase modulation effects between the two modes in the presence of PMD. Since the TM mode propagates more slowly, the cross phase modulation of the TM pulse by the TE imposes a blue chirp, whereas the cross-phase modulation of the TE pulse by the TM imposes a red chirp [29]. The spectral fringes overlaying the TE and TM spectra are an experimental artifact, and likely result from an imperfect mapping of the polarization state at the waveguide output to the analyzer.

The remarkable feature of the $\phi = \pm\pi/4$ spectra in Fig. 4.4(d) is the interference

pattern. This pattern indicates that the pulse is oscillating between $\pm\pi/4$ polarization states across its spectrum. The physical origin of these spectral polarization oscillations is the strong PMD in the waveguide that occurs as a result of its subwavelength height. This PMD causes the TM pulse to be temporally delayed from the TE pulse by a time T_d in the waveguide. When the analyzer is oriented in either of the $\pm\pi/4$ polarization states it outputs pulses from both the TE and TM modes. Since these pulses are co-polarized after the analyzer, they add coherently as indicated by Eq. (4.4). The resulting spectral intensity is effectively multiplied by a factor $\cos^2(\omega T_d/2)$, where $\omega = 2\pi c/\lambda$ is the angular frequency of light. The time delay T_d can be estimated from the period of the interference pattern $\Delta\lambda_p$ by

$$T_d = \frac{\lambda_0^2}{c\Delta\lambda_p}. \tag{4.5}$$

In Fig. 4.4(d) $\Delta\lambda_p \approx 0.76$ nm, indicating a TM–TE pulse delay of 10.5 ps in the waveguide. The differential group delay (T_d/L) is therefore ≈ 1.3 ps/mm. This value is slightly larger than the theoretical value of 0.95 ps/mm that is calculated using the finite-difference method of Ref. [96]. The discrepancy is likely due to the actual waveguide geometry being slightly different from its design. As indicated by Fig. 3.2(b), the differential group delay is sensitive to small variations in the waveguide geometry in the subwavelength regime.

The value of T_d deduced from the period of the spectral interference pattern is confirmed by the autocorrelation measurement shown in Fig. 4.5. In the figure autocorrelation traces are shown for three different values of the analyzer orientation. When the analyzer is oriented to isolate either the TE or TM modes it appears very similar to the autocorrelation trace of the input pulses in Fig. 4.2(b). When the orientation is adjusted to $\phi = -\pi/4$ the trace develops a distinctive three-peak structure, which is indicative of two peaks in the pulse intensity. These two intensity peaks are temporally separated by the same duration as the separation of the dominant peak in the center of the autocorrelation with either of the two side lobes. The autocorrelation indicates that this separation is ~10 ps, which agrees with the spectral data.

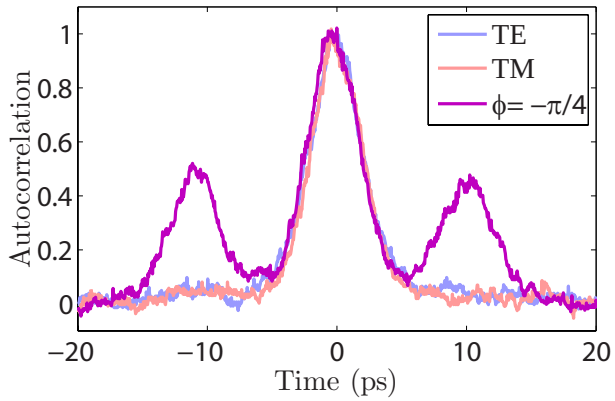

Figure 4.5: Autocorrelation traces after the 8 mm waveguide for each of three analyzer orientations when the input polarization is adjusted to excite both the TE and TM modes.

Theoretical modeling

Most of the parameters used in the theoretical model are calculated as was done in chapter 3, and are recorded in Table 4.2. For the differential group delay ($\beta_1^{TM} - \beta_1^{TE}$) the experimentally derived value of 1.3 ps/mm is used rather than the numerical one. As discussed in section 4.1 the input-coupling efficiency from the fiber to the waveguide is not precisely known for either mode, and will be used as a fitting parameter. For the sake of simplicity it will also be assumed that the TE and TM modes are equally excited in the waveguide, even though this is likely not the case in the experiment.

Figure 4.6 shows the results of the calculation for an input coupling loss of 1.5 dB. This loss is lower than expected, and the reason for this apparent discrepancy is not known. The results of the calculation are in qualitative agreement with the experimental spectra of Fig. 4.4. In particular, the three-peak structure of the TE

γ_{11}, γ_{22}, γ_{12}	79, 66, 61 $W^{-1}m^{-1}$
β_2^{TE}, β_2^{TM}	-1.4, -3.5 ps^2/m
Π_1, Π_2	1.1, 1.1
τ_{fc}	1 ns

Table 4.2: Parameter values used in the solution of Eqs. (3.13) and (3.14).

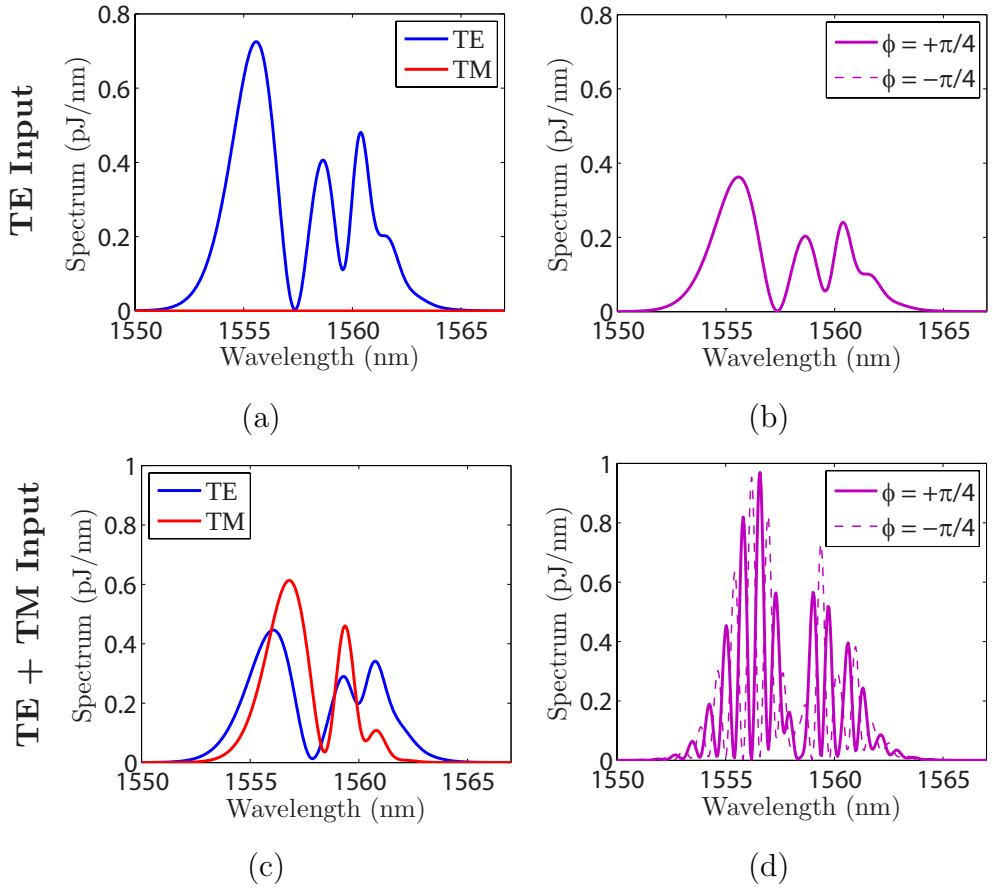

Figure 4.6: Modeling results for the measurements shown in Fig. 4.4.

spectrum in Fig. 4.6(a) and of the TE and TM spectra in Fig. 4.6(c) agree with the basic features of the experimental results. The theoretical TE spectrum in Fig. 4.6(a) is notably more blue shifted than the experimental one in Fig. 4.4(a). Moreover, its central peak is the lowest of the three in contrast to Fig. 4.4(a) where it is the highest. The agreement is better in the case of a mixed-polarization input, yet the theoretical spectra of Fig. 4.6(c) are also more blue-shifted than the experimental spectra of Fig. 4.4(c). Part of the reason for this may be the red feature in the input pulse spectrum in Fig. 4.3(a), which is not taken into account in the theory.

It can be concluded that the theoretical model reproduces the experimental results qualitatively, but that they are not in close quantitative agreement. The reason for this is primarily a result of a lack of precise knowledge of the experimental scenario. Many unknown quantities are assumed or approximated in the theoretical model,

such as the input pulse shape, the input-coupling losses for the two modes, and the values of n_2 and β_{TPA} (which are not well agreed upon as discussed in chapter 3). Thus, the results of this comparison do not necessarily reflect on the validity of the theoretical model.

4.3 Self-phase modulation and temporal polarization oscillations

At the output of the 8 mm waveguide pulses were seen to have undergone dramatic spectral oscillations in their state of polarization. In the time domain each pulse split into two distinct pulses that completely separated from one another, each having a linear and orthogonal state of polarization (as is evident from Fig. 4.5). In this section we explore what happens to the temporal properties of pulses when the two orthogonal polarization components do not completely separate from one another. This is done by repeating the experiment of section 4.2 with a shorter waveguide.

3 mm waveguide measurements

Figure 4.7 shows the output spectra of the pulses from a 3 mm waveguide in each of four analyzer orientations when the input polarization is adjusted to excite both the TE and TM modes. Figure 4.7(a) shows the output spectra from each mode, which exhibit a multipeak structure characteristic of self-phase modulation. Figure 4.7(a) closely resembles the output spectra from the 8 mm waveguide in Fig. 4.4(c). This similarity is expected since most of the nonlinearity occurs at the beginning of the waveguide in the presence of the high propagation losses. Because the 3 mm waveguide output measurement in Fig. 4.7(a) is cleaner, the asymmetry between the TE and TM spectra is more evident. As discussed earlier, this asymmetry results from cross-phase modulation between the TE and TM pulses that enhances the blue shift of the TM pulse but reduces the blue shift of the TE pulse.

The measured output spectra when the analyzer is oriented at $\phi = \pm\pi/4$ is shown in Fig. 4.7(b) and exhibit the spectral polarization oscillations that result from PMD. The period of oscillation is larger than in the case of the 8 mm waveguide since the

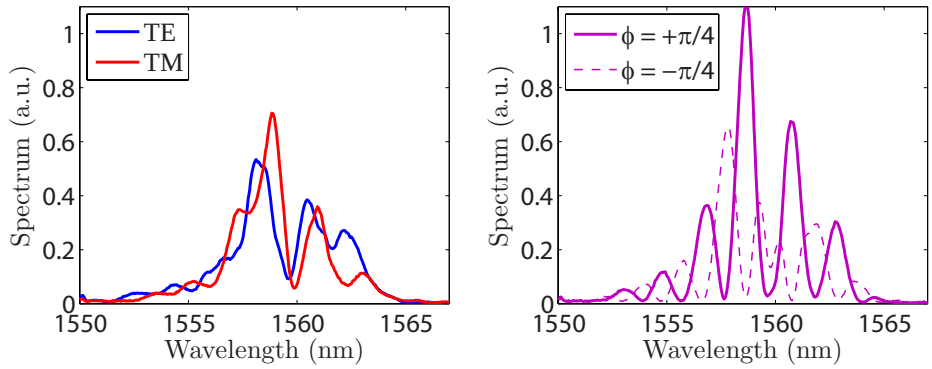

(a) (b)

Figure 4.7: Measured output spectra from the 3 mm waveguide when the input polarization is adjusted to excite both the TE and TM modes.

temporal separation between the two modes is shorter. The ~1.9 nm period indicates an overall temporal separation $T_d \approx 4.2$ ps. For the 3 mm waveguide the differential group delay is therefore ~1.4 ps/mm, which is close to the 1.3 ps/mm measurement from the 8 mm waveguide.

The most remarkable difference between the 3 mm and 8 mm waveguides occurs in the time domain. Figure 4.8 shows autocorrelation traces of output pulses from the 3 mm waveguide for three different orientations of the analyzer. When the analyzer isolates either the TE or TM modes the trace is similar to that of the input pulses in Fig. 4.2(b). The TE pulse's trace is slightly broader than that of the TM, presumably as a result of its slightly broader spectrum [Fig. 4.7(a)] and GVD in the EDFA before autocorrelation. When the analyzer is oriented at $\phi = +\pi/4$, however, the trace looks very different. Not only does it exhibit the expected broadening from PMD, but it additionally exhibits significant internal structure. At least nine distinguishable peaks can be seen in the trace, which is indicative of five distinct peaks in the pulse's intensity profile. The pulse is therefore oscillating between $+\pi/4$ and $-\pi/4$ linear polarization states across its temporal duration.

In contrast to the spectral polarization oscillations the temporal polarization oscillations are nonlinear in nature. The inset of Fig. 4.8 shows the autocorrelation trace for $\phi = +\pi/4$ when the input coupling to the waveguide is slightly misaligned so that the transmitted power drops by 3 dB. The significant internal structure of

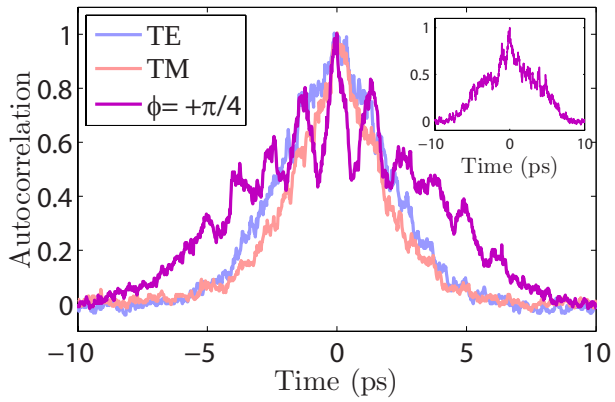

Figure 4.8: Autocorrelation traces after the 3 mm waveguide when the input polarization is adjusted to excite both the TE and TM modes. The inset shows the autocorrelation trace for $\phi = +\pi/4$ when the power is reduced by misaligning the input fiber.

the trace virtually disappears in this case. It should be noted that the measurement shown in the inset is noisier as a result of the lower signal power. This noise could partially explain the disappearence of the internal structure but it is not significant enough to explain it completely.

Theoretical modeling

The theoretical model of chapter 3 clarifies the origin of the temporal polarization oscillations. The input coupling loss (from the fiber to the waveguide) is not known for certain and is used as a fitting parameter in the simulations, as was done in section 4.2. The best fit is found for an input coupling loss of 1 dB, which is lower than expected. The reason for this apparent discrepancy is unknown. Regardless, the simulations can be used for a qualitative description of the experiment if not a precise quantitative one. The rest of the parameters are reported in Table 4.2, except for the differential group delay for which the experimentally derived value of 1.4 ps/mm is used. For simplicity it is assumed that the input-coupling efficiency is the same for the TE and TM modes so that they are equally excited at the waveguide input, and that they both have propagation losses of 10 dB/cm [91].

Figure 4.9 shows the simulated output spectra for each of the four analyzer ori-

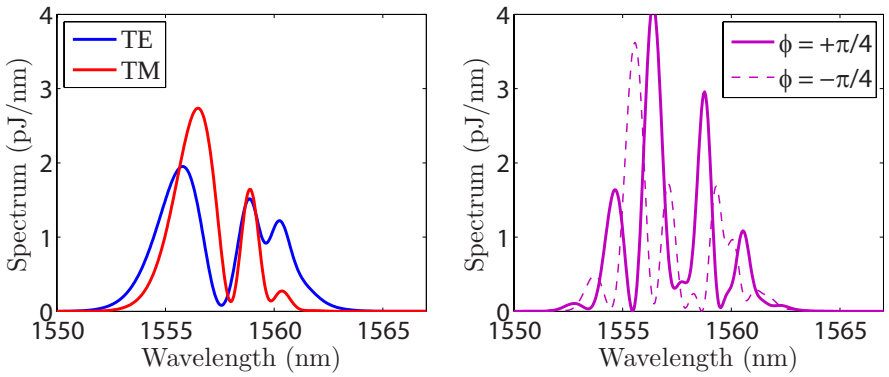

Figure 4.9: Modeling results for the measurements shown in Fig. 4.7.

entations. The qualitative features of the TE and TM spectra in Fig. 4.9(a) closely resemble those observed in the experiment [Fig. 4.7(a)]. Quantitatively, they exhibit a notably stronger blue shift (by about 2 nm). As suggested in section 4.2, this may result from the feature on the red side of the input spectrum [Fig. 4.3(a)], which is not taken into account in the simulations.

Figure 4.10 shows the time dependence of the TE and TM phase profiles at the waveguide output, and provides an explanation for the polarization oscillations. The TE phase (blue dashed line) increases from 0 to just over 1 radian in the leading edge of the pulse. This results from both Kerr-induced self-phase modulation of the TE pulse by itself as well as cross-phase modulation of the TE pulse by the TM pulse. Notice that this initial increase induces a red-chirp that does not exist in the TM phase profile, explaining the presence of a stronger red component in the TE spectrum. The subsequent reduction of the TE phase to less than -3π radians results from a free-charge-carrier density that is generated by two-photon absorption and builds up over the pulse duration, decreasing the refractive index.

The phase profile of the TM pulse (red dashed-dotted curve) is different in two ways, both of which are related to PMD. First, it is flat in its leading edge and exhibits no initial increase. One reason for this is that Kerr-induced cross-phase modulation of the TM pulse by the TE acts to create a decreasing phase profile that can flatten out the increasing phase profile resulting from self-phase modulation of the TM pulse by itself [29]. This happens because the TM pulse travels more slowly than the TE.

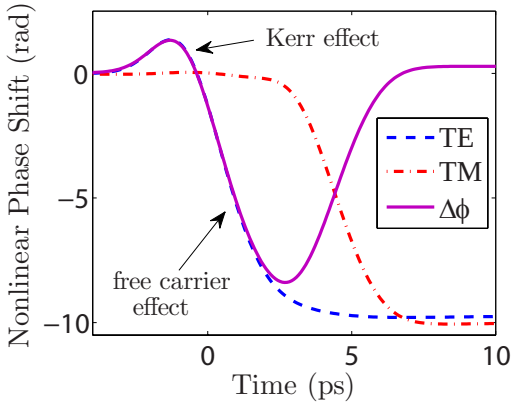

Figure 4.10: Simulated time dependence of the nonlinear phase shift in the TE mode (blue dashed curve), the TM mode (red dashed-dotted cuve), and their difference (purple solid curve).

Additionally, free carriers generated by the TE pulse act to uniformly reduce the phase of the TM, which counterbalances the Kerr effect.

The second difference observable in the TM phase profile is the one responsible for the polarization oscillations. The dramatic phase reduction caused by free carriers occurs ~4 ps later for the TM pulse than for the TE. Physically, the free carrier phase shifts occur mostly at the waveguide input where two-photon absorption is strongest, and are subsequently delayed from one another in the waveguide because of the PMD. The result is that the relative phase between the TE and TM modes, $\Delta\phi$ (purple solid line), drops to almost -3π in the center of the pulse and then rises up again to zero. This is sufficient to cause the pulse to vary between $+\pi/4$ and $-\pi/4$ linear polarization states ~6 times across its temporal duration. Despite this dramatic relative phase shift, Fig. 4.11(a) indicates that the effects of the waveguide alone are not sufficient to account for the degree of polarization oscillation observed in the experiment. Shown in the figure is the time-domain behavior of the pulse intensity immediately after the analyzer for each of the four orientations. The intensity profile of the $\phi = +\pi/4$ orientation shows only two peaks as a result of the weak temporal overlap of the TE and TM pulses in the time domain.

The simulations indicate that the temporal polarization oscillations are enhanced by GVD in the EDFA immediately before autocorrelation. Physically, this can be

understood as follows: as the influence of the analyzer and GVD are both linear, they are independent of order. Thus, the observed autocorrelation would be the same if the pulses had been amplified first and then passed through the analyzer before autocorrelation, rather than in the order it was done in the experiment. In this physically equivalent scenario, we can imagine the influence of GVD in the amplifier to be broadening the temporal duration of both the TE and TM pulses from the waveguide output, enhancing their temporal overlap. This enhanced temporal overlap, combined with the dramatic relative phase shifts between the modes created in the waveguide, leads to the dramatic temporal polarization oscillations observed in the experiment. This is shown more clearly in Figs. 4.11(b) and 4.11(c), which show the temporal intensity profiles of the pulses after having experienced dispersions of $\beta_2 L$ = 0.2 ps^2 and 0.4 ps^2, respectively, where L is the propagation length of the amplifier and β_2 is its GVD parameter. The simulations verify the intuitive explanation, indicating as many as 4 temporal intensity peaks, which is close to the 5 indicated by the autocorrelation in Fig. 4.8. The values of $\beta_2 L$ were not chosen arbitrarily, but were based on an estimate of the dispersion of 0.2 ps^2, obtained by comparing the temporal width

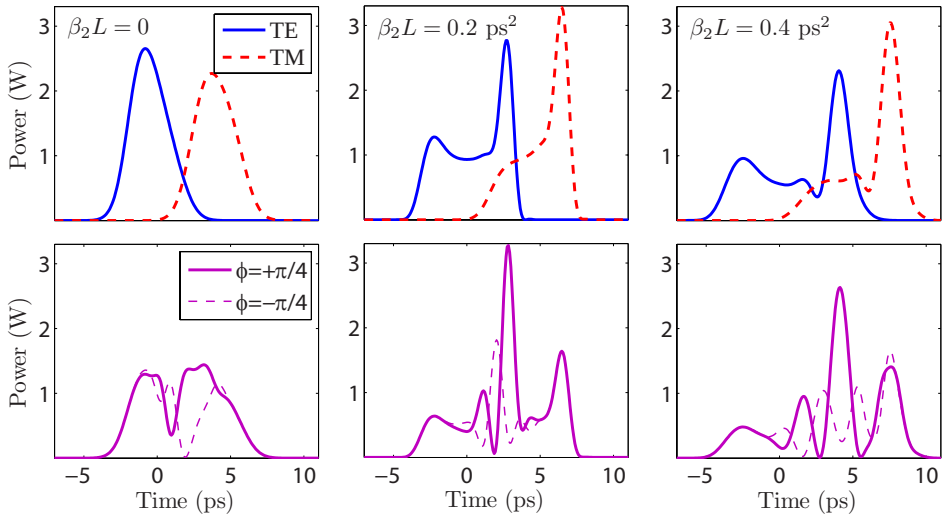

Figure 4.11: Simulated pulse power before autocorrelation for values of the EDFA's dispersion parameter $\beta_2 L$ of (a) 0, (b) 0.2 ps^2, and (c) 0.4 ps^2, indicating its influence in the autocorrelation measurement of Fig. 4.8.

of the source-pulse autocorrelation before and after the EDFA (shown in Fig. 4.2(b)). Effects such as asymmetric spectral gain and self-phase modulation occurring in the EDFA were not taken into account, so this was only a rough estimate.

4.4 Summary

This chapter has presented an experimental and theoretical study of nonlinear polarization effects in silicon waveguides that have a subwavelength dimension. The waveguides considered here exhibited significant PMD as a result of a subwavelength waveguide height ($< \lambda/n_0$). This PMD couples with self-phase modulation to induce dramatic changes in the spectral and temporal properties of optical pulses. The pulse spectra were seen to not only broaden as a result of self-phase modulation, but to exhibit polarization oscillations as a result of the temporal walk off between TE and TM modes from PMD. In the time domain the nonlinear phase modulations were seen to combine with this temporal walk-off to create temporal polarization oscillations as well. The theoretical methodology of chapter 3 was used to explain the observed phenomena. While the theoretical simulations were powerful in explaining the qualitative features of the experimental results, they did not supply a precise quantitative one. However, because of a lack of exact knowledge about a number of features in the experimental scenario (input pulse properties, coupling efficiencies, etc.), this does not necessarily reflect on the validity of the theoretical model.

5 Perturbative methods for nonlinear photonic resonators

Optical resonators have been critical to the field of photonics since the invention of the laser. They are widely studied in the subfield of nonlinear photonics as a result of the enhancement in intensity (and hence nonlinearity) that they provide. In on-chip microresonators, for example, phenomena such as parametric oscillation [112–114], Raman lasing [115–117], and all-optical switching [119, 120, 141] have been explored over the last decade.

A general theory of nonlinear optical interactions in dielectric resonators has been developed and applied by Oskar Painter's group at the California Institute of Technology [53–55]. The theory describes the optical field by a system of first-order differential equations for the amplitudes of the cavity modes. The time development of the amplitudes is influenced not only by linear effects such as coupling to an input field and resonator loss, but also by nonlinear effects incorporated through a general perturbing dipole-moment density, $\mathbf{P}^{NL}$. The equations are obtained from the Helmholtz equation, are reduced to first order by making use of the slowly-varying envelope approximation, and employ a specific mode-orthogonality condition.

An alternative theory describing perturbative effects in resonant cavities casts Maxwell's equations in an operator form [121]. A change in dielectric permitivitty $\Delta\epsilon$ is incorporated using a time-dependent perturbation theory that describes its influence on the mode amplitudes. This method is rigorous in the sense that it employs few assumptions, but it is less general than the approach of Refs. [53–55] since it only applies to perturbations in the dielectric permitivitty. A third approach was developed in Ref. [122], which is a work of the author and contributes content to

this chapter.

In this chapter the general equations of Refs. [53–55] are derived by using a more rigorous methodology, similar to the one developed in Ref. [121]. The slowly-varying envelope approximation is not made, and an exact mode-orthogonality condition is derived that applies to all kinds of dielectric resonators, since no assumptions are made about the structure of the cavity. Since the perturbing dipole-moment density $\mathbf{P}^{NL}$ can in principle incorporate linear effects such as gain in addition to nonlinearity, the theoretical methodology presented here can be widely applied in the field of resonator optics. In section 5.1 the theory is developed for the simplest case of resonators constructed of isotropic media. Sections 5.2 and 5.3 extend the theory to resonators formed using anisotropic and magnetic media, respectively. Section 5.4 summarizes the results of this chapter.

5.1 Dielectric resonators in isotropic media

The optical field in a resonator is described by Maxwell's Eqs. (2.1) and (2.2). In a material system composed of isotropic and nonmagnetic media these equations reduce to

$$\nabla \times \mathbf{E} = -\mu_0 \frac{\partial \mathbf{H}}{\partial t}, \tag{5.1}$$

$$\nabla \times \mathbf{H} = \epsilon_0 \epsilon(\mathbf{r}) \frac{\partial \mathbf{E}}{\partial t} + \frac{\partial \mathbf{P}^{NL}}{\partial t}. \tag{5.2}$$

In the following analysis, the field quantities in Eqs. (5.1) and (5.2) are considered to be the complex, analytical-signal representations of their real counterparts [66]. The structure of the cavity is described by the dielectric permitivitty $\epsilon(\mathbf{r})$. The permitivitty is assumed to be real and independent of frequency. The phenomena of material absorption and dispersion can, however, be included as linear contributions to the perturbing dipole-moment density $\mathbf{P}^{NL}$.

5.1.1 A vector space formulation of Maxwell's equations

It was shown in Ref. [123] that, in the absence of the perturbation, Eqs. (5.1) and (5.2) can be cast in an operator form analagous to the Schrödinger equation,

$$i\frac{\partial}{\partial t}\left|\psi\right\rangle = \hat{M}\left|\psi\right\rangle + \left|V(t)\right\rangle. \tag{5.3}$$

Equation (5.3) describes how a state $|\psi\rangle$ traverses a vector space in time. The vector space is the set of all pairs of square-integrable fields, and the state represents the electromagnetic field,

$$\left|\psi\right\rangle = \begin{pmatrix} \sqrt{\epsilon_0}\,\mathbf{E} \\ \sqrt{\mu_0}\,\mathbf{H} \end{pmatrix}. \tag{5.4}$$

The operator $\hat{M}$ that drives the time evolution is given by

$$\hat{M} = \begin{pmatrix} 0 & i\frac{c}{\epsilon}\nabla\times \\ -ic\nabla\times & 0 \end{pmatrix}. \tag{5.5}$$

In the presence of optical nonlinearity the time evolution of the field is additionally influenced by the perturbation $|V(t)\rangle$, which is given as

$$\left|V(t)\right\rangle = \begin{pmatrix} \frac{-i}{\epsilon\sqrt{\epsilon_0}}\frac{\partial \mathbf{P}^{NL}}{\partial t} \\ 0 \end{pmatrix}. \tag{5.6}$$

The vector space under consideration is an inner-product space under the definition

$$\left\langle\psi_a|\psi_b\right\rangle = \frac{1}{4}\int \left(\epsilon_0\epsilon(\mathbf{r})\mathbf{E}_a^*\cdot\mathbf{E}_b + \mu_0\mathbf{H}_a^*\cdot\mathbf{H}_b\right)d^3\mathbf{r}. \tag{5.7}$$

Note that $\langle\psi|\psi\rangle$ is the energy stored in the optical field. As shown in appendix C, the operator $\hat{M}$ is Hermitian under this definition of the inner product. Thus, the eigenstates of $\hat{M}$ have real eigenvalues ω_k [124],

$$\hat{M}\left|\omega_k\right\rangle = \omega_k\left|\omega_k\right\rangle. \tag{5.8}$$

The cavity modes are such eigenstates. In the absence of the perturbative term (i.e. when $|V(t)\rangle = 0$) they form a discrete set of solutions to Eq. (5.3) that oscillate at their eigenfrequencies, $|\psi_k(t)\rangle = e^{-i\omega_k t}\,|\omega_k\rangle$. In the analysis that follows it is assumed that solutions for the modes of the cavity are already known. Their electric and

magnetic field profiles will be denoted by $\mathbf{e}_k(\mathbf{r})$ and $\mathbf{h}_k(\mathbf{r})$ so that the eigenstates are expressed as

$$|\omega_k\rangle = \begin{pmatrix} \sqrt{\epsilon_0}\,\mathbf{e}_k \\ \sqrt{\mu_0}\,\mathbf{h}_k \end{pmatrix}. \tag{5.9}$$

Because $\hat{M}$ is a Hermitian operator, modes having different resonance frequencies are orthogonal,

$$\langle\omega_k|\omega_m\rangle = N_m\delta_{km}. \tag{5.10}$$

In the case of two or more cavity modes that have the same resonance frequency, the well known Grahm-Schmidt process can be used to find an orthogonal basis set so that Eq. (5.10) can be considered to apply between all of the cavity modes. By using the fact that, for monochromatic solutions of Maxwell's equations, the electric energy in the field is equal to the magnetic energy, the normalization constant N_m can be expressed in terms of the electric field only,

$$N_m = \frac{1}{2}\int \varepsilon_0\epsilon(\mathbf{r})|\mathbf{e}_m|^2 d^3\mathbf{r}. \tag{5.11}$$

5.1.2 Time-dependent perturbation theory

A solution for the electromagnetic field in the presence of a nonzero $|V(t)\rangle$ is found by applying a time-dependent perturbation theory, such as is often done in quantum mechanics. In reality the field will include not only a portion that is confined to the cavity but also a portion that is radiated away as a result of scattering. In the case of relatively high-Q cavities, however, we can assume that the field is dominated by the resonantly enhanced cavity modes and that the scattered field is negligible in comparison. Thus, the solution is assumed to be a sum over this discrete set of modes,

$$|\psi(t)\rangle = \sum_m \frac{a_m(t)}{\sqrt{N_m}}\,|\omega_m\rangle\,, \tag{5.12}$$

where $a_m(t)$ is the amplitude of mode m at time t. The normalization constant N_m is included so that $|a_m(t)|^2$ represents the energy stored in mode m. By using solution (5.12) in Maxwell's Eq. (5.3), taking the inner product of both sides with $\langle\omega_k|$, and

using the mode-orthogonality condition (5.10) we arrive at a differential equation for the k^{th} mode amplitude,

$$\frac{da_k}{dt} = -i\omega_k a_k - \frac{i}{\sqrt{N_k}} \langle \omega_k | V(t) \rangle . \tag{5.13}$$

By using definitions (5.6) and (5.9) this last equation can be written

$$\frac{da_k}{dt} = -i\omega_k a_k - \frac{1}{4\sqrt{N_k}} \int \mathbf{e}_k^* \cdot \frac{\partial \mathbf{P}^{NL}}{\partial t} \, d^3\mathbf{r}. \tag{5.14}$$

There are two fundamental phenomena that must be taken into account in order for the theory to be general: resonator losses and coupling to an input field. Both of these can, in principle, be incorporated as linear contributions to the perturbing dipole-moment density $\mathbf{P}^{NL}$. Such an approach, however, is usually too complicated to be useful. A phenomenological approach to incorporating these two phenomena is described in appendix D and leads to the addition of two terms to Eq. (5.14),

$$\frac{da_k}{dt} = -i\omega_k a_k - \frac{1}{2\tau_{ph}^k} a_k + \kappa_k A_{in}(t) - \frac{1}{4\sqrt{N_k}} \int \mathbf{e}_k^* \cdot \frac{\partial \mathbf{P}^{NL}}{\partial t} \, d^3\mathbf{r}. \tag{5.15}$$

In Eq. (5.15), τ_{ph} is the photon lifetime of the cavity and $A_{in}(t)$ is the input field, normalized so that $|A_{in}(t)|^2$ is the optical power. The coupling coefficient $\kappa_k = \sqrt{T_k/\tau_r}$, where τ_r is the round-trip time of a photon in the resonator and T_k is the input-coupling efficiency [125]. For example, if the input field were coupled to the resonator through a mirror, T_k would be the transmissivity of that mirror.

Equation (5.15) will be referred to as the dynamic mode-amplitude equation. It is the main result of this chapter. In sections 5.2 and 5.3 its applicability is extended to include resonators composed of both anisotropic and magnetic media, but before that the important issue of coupling to output fields is addressed.

5.1.3 Output field relations

The theory of this chapter has been developed around the mode-energy amplitudes, $a_k(t)$. Although $|a_k(t)|^2$ represents a physical quantity (the optical energy stored in the cavity), it is not directly measurable. What are measurable are the output fields to which the cavity is coupled. There is always at least one output field, a reality that

is not only a necessary result of coupling to an input field but that is also desirable for using resonators as devices. In most cases a resonator couples to either 1 or 2 output fields, although more are possible. We will assume that there are not more than 2, although the equations developed here can be extended to cases where there are more than 2 as well.

The first output field will be referred to as the 'reflected' field and denoted by A_r. The distinguishing characteristic of the reflected field is that it has contributions from the field coupling out of the cavity and from a fraction of the input field that never coupled into the cavity in the first place (i.e. reflected from the coupler). The reflected output field always exists when the cavity is coupled to an input. Although there are exotic cases where there are multiple reflected fields, we will assume the most common case for which there is only one. In cases where there is a second output field it will be referred to as the 'transmitted' field and denoted by A_t. This field has no direct contribution from the input but is entirely the result of what is indirectly transmitted through the cavity. The complex field amplitudes $A_r(t)$ and $A_t(t)$ are chosen to be power amplitudes, meaning that $|A_r(t)|^2$ and $|A_t(t)|^2$ represent the optical power in each of the two output ports.

It was shown by Haus using energy-conservation considerations that in the case of a single mode (for example the k^{th} mode) the appropriate expressions for the reflected and transmitted fields are [125]

$$A_r(t) = -A_{in}(t) + \kappa_k a_k(t), \tag{5.16}$$

$$A_t(t) = \kappa_k^t a_k(t). \tag{5.17}$$

In Eq. (5.16) the output-coupling coefficient κ_k is the same as the input-coupling coefficient in Eq. (5.15). In Eq. (5.17) the coupling coefficient κ_k^t can differ if the resonator is asymmetric (meaning that the two output couplers are not identical). These equations are easily generalized to cases where multiple modes of the cavity are excited,

$$A_r(t) = -A_{in}(t) + \sum_k \kappa_k a_k(t), \tag{5.18}$$

$$A_t(t) = \sum_k \kappa_k^t a_k(t). \tag{5.19}$$

Coupling to output fields is one source of resonator loss that contributes to the photon lifetime. The other source is intrinsic resonator loss, which results from material absorption and scattering. As discussed in more detail in appendix D, the photon lifetime can be considered to have independent contributions from intrinsic losses and from each of the output couplers,

$$\frac{1}{\tau_{ph}^{k}} = \frac{1}{\tau_{ph}^{k,i}} + \frac{1}{\tau_{ph}^{k,r}} + \frac{1}{\tau_{ph}^{k,t}}, \tag{5.20}$$

where $\tau_{ph}^{k,i}$ is the intrinsic photon lifetime of the resonator and $\tau_{ph}^{k,r}$ and $\tau_{ph}^{k,t}$ represent contributions from coupling to the reflected field and the transmitted field, respectively. These last two lifetimes are related to the coupling coefficients in the following way [125]:

$$\kappa_k = \left(\tau_{ph}^{k,r}\right)^{-1/2}, \tag{5.21}$$

$$\kappa_k^t = \left(\tau_{ph}^{k,t}\right)^{-1/2}. \tag{5.22}$$

Equations (5.18) and (5.19) for the output fields, when combined with relations (5.20), (5.21), and (5.22) for the loss contributions, form a complete description of coupling to two output fields of the resonator. They are not only applicable to resonators composed of isotropic materials, but to resonators composed of anisotropic and/or magnetic materials as well, which are considered next.

5.2 Extension to anisotropic media

In the case of anisotropic media the dielectric permitivitty is a tensor. Maxwell's equations then become

$$\nabla \times \mathbf{E} = -\mu_0 \frac{\partial \mathbf{H}}{\partial t}, \tag{5.23}$$

$$\nabla \times \mathbf{H} = \epsilon_0 \overleftrightarrow{\epsilon}(\mathbf{r}) \frac{\partial \mathbf{E}}{\partial t} + \frac{\partial \mathbf{P}^{NL}}{\partial t}. \tag{5.24}$$

As in the case of isotropic media the permitivitty $\overleftrightarrow{\epsilon}$ will be considered to be independent of frequency. It will also be assumed that the materials are lossless, implying that the permitivitty is a Hermitian matrix, i.e.

$$\epsilon_{ij} = \epsilon_{ji}^{*}. \tag{5.25}$$

Material loss and dispersion can be added in as linear contributions to $\mathbf{P}^{NL}$ if necessary.

As in the case of isotropic media, Maxwell's Eqs. (5.23) and (5.24) can be cast in the operator form of Eq. (5.3). The operator $\hat{M}$ and perturbation $|V(t)\rangle$ are both modified,

$$\hat{M} = \begin{pmatrix} 0 & ic\overleftrightarrow{\boldsymbol{\epsilon}}^{-1}\nabla\times \\ -ic\nabla\times & 0 \end{pmatrix}, \qquad |V(t)\rangle = \begin{pmatrix} \frac{-i}{\sqrt{\epsilon_0}}\overleftrightarrow{\boldsymbol{\epsilon}}^{-1}\frac{\partial \mathbf{P}}{\partial t}^{NL} \\ 0 \end{pmatrix}. \tag{5.26}$$

Additionally, the inner product defined by Eq. (5.7) is no longer valid. In order that $\langle\psi|\psi\rangle$ maintains its meaning as the optical energy, the inner product for anisotropic media will be defined as follows:

$$\langle\psi_a|\psi_b\rangle = \frac{1}{4}\int \left(\epsilon_0 \mathbf{E}_a^* \cdot \overleftrightarrow{\boldsymbol{\epsilon}}\mathbf{E}_b + \mu_0 \mathbf{H}_a^* \cdot \mathbf{H}_b\right) d^3\mathbf{r}. \tag{5.27}$$

As proved in appendix C, the operator $\hat{M}$ given by Eq. (5.26) is Hermitian under this inner product. As a result the time-dependent perturbation theory of section 5.1.2 still applies and Eq. (5.13) holds for anisotropic media as well. Applying the definitions for $|V(t)\rangle$ in Eq. (5.26) and the inner product in Eq. (5.27) to Eq. (5.13), and incorporating resonator loss and coupling using the phenomenological method of appendix D yields

$$\frac{da_k}{dt} = -i\omega_k a_k - \frac{1}{2\tau_{ph}^k}a_k + \kappa_k A_{in}(t) - \frac{1}{4\sqrt{N_k}}\int \mathbf{e}_k^* \cdot \frac{\partial \mathbf{P}}{\partial t}^{NL} d^3\mathbf{r}. \tag{5.28}$$

Thus, the dynamic mode-amplitude equation for anisotropic media is expressed in exactly the same form as for isotropic media.

5.3 Extension to magnetic media

The most general case is that of a resonator composed of media that are both anisotropic and magnetic. In this case Maxwell's equations become

$$\nabla \times \mathbf{E} = -\mu_0 \overleftrightarrow{\boldsymbol{\mu}}(\mathbf{r})\frac{\partial \mathbf{H}}{\partial t} - \mu_0 \frac{\partial \mathbf{M}}{\partial t}^{NL}, \tag{5.29}$$

$$\nabla \times \mathbf{H} = \epsilon_0 \overleftrightarrow{\boldsymbol{\epsilon}}(\mathbf{r})\frac{\partial \mathbf{E}}{\partial t} + \frac{\partial \mathbf{P}}{\partial t}^{NL}, \tag{5.30}$$

where $\mathbf{M}^{NL}$ is the perturbing magnetic dipole-moment density that is over and above the linear magnetic response of the medium. The linear magnetic response is described by the magnetic permeability tensor $\overleftrightarrow{\boldsymbol{\mu}}$, which is assumed to be independent of frequency. Just as for the permitivitty tensor, the permeability is assumed to be Hermitian, i.e.

$$\mu_{ij} = \mu_{ji}^{*}. \tag{5.31}$$

Maxwell's Eqs. (5.29) and (5.30) can again be written in the operator form of Eq. (5.3), where

$$\hat{M} = \begin{pmatrix} 0 & ic\overleftrightarrow{\boldsymbol{\epsilon}}^{-1}\nabla\times \\ -ic\overleftrightarrow{\boldsymbol{\mu}}^{-1}\nabla\times & 0 \end{pmatrix}, \qquad |V(t)\rangle = \begin{pmatrix} \frac{-i}{\sqrt{\epsilon_0}}\overleftrightarrow{\boldsymbol{\epsilon}}^{-1}\frac{\partial \mathbf{P}}{\partial t}^{NL} \\ -i\sqrt{\mu_0}\overleftrightarrow{\boldsymbol{\mu}}^{-1}\frac{\partial \mathbf{M}}{\partial t}^{NL} \end{pmatrix}. \tag{5.32}$$

The inner product is redefined to maintain its physical significance,

$$\langle \psi_a | \psi_b \rangle = \frac{1}{4}\int \left(\epsilon_0 \mathbf{E}_a^{*}\cdot\overleftrightarrow{\boldsymbol{\epsilon}}\mathbf{E}_b + \mu_0 \mathbf{H}_a^{*}\cdot\overleftrightarrow{\boldsymbol{\mu}}\mathbf{H}_b\right) d^3\mathbf{r}. \tag{5.33}$$

Under this definition for the inner product, the operator $\hat{M}$ of Eq. (5.32) is Hermitian, as proved in appendix C. Thus, the time-dependent perturbation theory of section 5.1.2 applies and Eq. (5.13) holds. Using Eqs. (5.32) and (5.33), Eq. (5.13) reduces to

$$\begin{aligned} \frac{da_k}{dt} &= -i\omega_k a_k - \frac{1}{2\tau_{ph}^{k}}a_k + \kappa_k A_{in}(t) \\ &- \frac{1}{4\sqrt{N_k}}\int \left(\mathbf{e}_k^{*}\cdot\frac{\partial \mathbf{P}}{\partial t}^{NL} + \mu_0 \mathbf{h}_k^{*}\cdot\frac{\partial \mathbf{M}}{\partial t}^{NL}\right) d^3\mathbf{r}. \end{aligned} \tag{5.34}$$

Thus, the dynamic mode-amplitude equation for magnetic media takes a similar form as for nonmagnetic media, except that it has an additional contribution from the perturbing magnetic dipole-moment density.

5.4 Summary

In this chapter the dynamic mode-amplitude equation [Eq. (5.15)] was derived, which describes the dynamics of the optical field in a dielectric resonator in the presence of material nonlinearity. This equation is valid for any type of dielectric resonator since no assumption was made regarding the structure of the cavity. Moreover, it applies

to cavities with subwavelength dimensions since the vectorial nature of the resonator modes was taken into account. It was shown that it applies not only to resonators composed of isotropic materials, but to resonators composed of anisotropic materials as well. In the case of magnetic materials a slightly modified form of the equation [Eq. (5.34)] was derived that takes into account the possibility of a nonlinear magnetic response.

6 Dynamic refractive-index changes in optical resonators

Perhaps the simplest kind of perturbation to an optical resonator is a change in its refractive index, which can be induced by some external means such as an electro-optic effect or a nonlinear optical effect. Such perturbations have recently been investigated by a number of research groups. This work began with a 2005 study of dynamic refractive-index changes in coupled resonator structures, which was concerned with the possibility of stopping and storing light [126]. Soon after, Notomi and Mitsugi used finite-difference time-domain numerical simulations to consider the simplest case of a single cavity, concluding that if the refractive index were changed while light was trapped inside then the frequency of that light would shift in concert with the cavity's resonance frequency [127]. They dubbed this process 'adiabatic wavelength conversion' (AWC). It was demonstrated experimentally in 2007 by Preble et al. in a silicon microring resonator [128]. In that experiment a probe pulse was used to resonantly excite a cavity mode. While the probe pulse was trapped in the resonator, a pump pulse at the 415 nm wavelength (absorbed by silicon) illuminated the cavity to create electron-hole pairs, decreasing the refractive index. The observed result was a blue shift in the transmission spectrum, agreeing with the prediction of Notomi and Mitsugi that the frequency of the optical field would change as $\Delta\omega = -\omega_0 \Delta n / n_0$, where ω_0 and n_0 are the frequency of the field and refractive index of the cavity before the perturbation, respectively, and Δn is the index change. Experimental observations of AWC were later reported by a number of other research groups using similar pump-probe arrangements [129–131]. The first electro-optic implementation of AWC was reported in 2010 by Tanabe et al. [132].

A phenomenon related to AWC was also observed by Notomi and Mitsugi in their numerical simulations [127]. They reported that if the refractive-index change in the cavity is not spatially uniform, then it can couple the light from a resonantly excited cavity mode into neighboring modes. This process, which will be referred to in this chapter as dynamic mode coupling, was observed experimentally in 2008 by Dong et al. [121]. Their experiment used the same pump-probe arrangement in a silicon resonator that was employed in Ref. [128] (these experiments were performed by the same group). It was slightly different in that a much larger resonator was used so that the electron-hole pairs were generated in only a fraction of the cavity. As a result the index change was spatially nonuniform. They observed the transition of optical energy from a resonantly excited mode into as many as 15 of the mode's nearest spectral neighbors.

The earliest theoretical studies of these phenomena were performed using finite-difference time-domain numerical simulations, and clarified the basic features of both AWC and dynamic mode coupling [127,133,134]. A coupled-mode approach was outlined in Ref. [121] for understanding the conditions under which dynamic mode coupling occurs, and which also describes AWC. This approach was originally developed for describing similar phenomena in photonic-crystal waveguides and has also been used for that purpose [135,136]. A linear-system approach was also developed by Xiao et al. that gives considerable insight into the underlying physics of AWC [137, 138]. This last approach was the first analytical or semi-analytical theory incorporating all of the relevant effects, including resonator losses and coupling to an external input field. Another theory was developed in Refs. [122,139], which are works of the author and contribute to this chapter.

In this chapter the theoretical methodology of chapter 5 is applied to both AWC and dynamic mode coupling. In section 6.1 the governing equations are derived. In section 6.2 the equations are interpreted and their predictions are compared with experimental results from the literature. In section 6.3 they are applied to determine the design features of a resonator that would be necessary for using AWC in a reconfigurable wavelength conversion device.

6.1 Governing equations

In the presence of dynamic refractive-index changes, the overall dielectric permitivitty of the cavity ϵ' can be written

$$\epsilon'(\mathbf{r},t) = \epsilon(\mathbf{r}) + \Delta\epsilon(\mathbf{r},t), \tag{6.1}$$

where $\epsilon(\mathbf{r})$ describes the structure of the resonator, and the time-dependent perturbation is represented by $\Delta\epsilon(\mathbf{r},t)$. The result of this change in permitivitty is that, in the presence of an electric field, a perturbing dipole-moment density is induced. Using the expression for the electric field in the cavity implied by Eq. (5.12), this perturbing dipole-moment density $\mathbf{P}^{NL}$ is expressed as

$$\begin{aligned}\mathbf{P}^{NL}(\mathbf{r},t) &= \epsilon_0\Delta\epsilon(\mathbf{r},t)\,\mathbf{E}(\mathbf{r},t) \\ &= \epsilon_0\Delta\epsilon(\mathbf{r},t)\sum_m \frac{a_m(t)}{\sqrt{N_m}}\mathbf{e}_m(\mathbf{r}).\end{aligned} \tag{6.2}$$

Note that even though the perturbation is denoted by $\mathbf{P}^{NL}$ it is technically only referred to as a nonlinear response if $\Delta\epsilon$ itself depends on the strength of the optical field. This is often the case but not always. Either way Eq. (6.2) is valid.

The governing mode-amplitude equations are obtained by substituting the expression for $\mathbf{P}^{NL}$ from Eq. (6.2) into Eq. (5.15). The result is a system of coupled differential equations,

$$\frac{da_k}{dt} = -i\omega_k a_k - \frac{1}{2\tau_{ph}^k}a_k + \kappa_k A_{in}(t) - \sum_m\left(\frac{d\Gamma_{km}}{dt}a_m + \Gamma_{km}\frac{da_m}{dt}\right), \tag{6.3}$$

where the terms Γ_{km} are elements of a dynamic coupling matrix and are given by

$$\Gamma_{km}(t) = \frac{\int \Delta\epsilon(\mathbf{r},t)\mathbf{e}_k^*(\mathbf{r})\cdot\mathbf{e}_m(\mathbf{r})\,d^3\mathbf{r}}{\left(4\int\epsilon(\mathbf{r})|\mathbf{e}_k(\mathbf{r})|^2\,d^3\mathbf{r}\int\epsilon(\mathbf{r})|\mathbf{e}_m(\mathbf{r})|^2\,d^3\mathbf{r}\right)^{1/2}}. \tag{6.4}$$

The influence of the externally-induced refractive-index change is described entirely by this time-dependent coupling matrix.

In many situations Eq. (6.3) can be simplified. If the approximation $da_m/dt \approx -i\omega_m a_m$ is made on the right hand side, and if we assume that refractive-index changes occur on a time scale much longer than an optical period so that $|d\Gamma_{km}/dt| \ll |\omega_m\Gamma_{km}|$, then Eq. (6.3) becomes

$$\frac{da_k}{dt} = -i\omega_k a_k - \frac{1}{2\tau_{ph}^k}a_k + \kappa_k A_{in}(t) + \sum_m i\Gamma_{km}\omega_m a_m. \tag{6.5}$$

It can be shown that the mode-coupling terms in the sum in Eq. (6.5) are equivalent to the ones derived in Ref. [135] using an alternative approach, which was also used by Dong et al. in Ref. [121].

6.2 Interpretation and comparison with experiments

6.2.1 Adiabatic wavelength conversion

Whereas dynamic mode coupling only occurs under specific conditions, AWC always occurs in the presence of refractive-index changes. This latter process is described by the diagonal elements of the coupling matrix (6.4), Γ_{kk}. In other words, the terms for which $m = k$ in the sum of Eq. (6.3) are responsible for AWC. To see this more clearly, consider the case when only a single mode (e.g. the q^{th} mode) is appreciably excited in the cavity. The set (6.3) can be reduced to a single equation,

$$(1+\Gamma)\frac{da_q}{dt} = -i\omega_q a_q - \left(\frac{1}{2\tau_{ph}^q} + \frac{d\Gamma}{dt}\right)a_q + \kappa_q A_{in}(t), \tag{6.6}$$

where $\Gamma = \Gamma_{qq}$ is given by

$$\Gamma(t) = \frac{\int \Delta\epsilon(\mathbf{r},t)|\mathbf{e}_q|^2 d^3\mathbf{r}}{2\int \epsilon(\mathbf{r})|\mathbf{e}_q|^2 d^3\mathbf{r}}. \tag{6.7}$$

Interpretation of equation (6.6)

Consider the behavior of the mode when it is excited by an input field that suddenly turns off at $t = 0$. In this case, for $t > 0$, Eq. (6.6) becomes

$$\frac{da_q}{dt} = -i\omega_q'(t)a_q - \gamma(t)a_q, \tag{6.8}$$

where

$$\omega_q'(t) = \frac{\omega_q}{1+\Gamma(t)}, \quad \gamma(t) = \left(\frac{1}{2\tau_{ph}^q} + \frac{d\Gamma}{dt}\right)\frac{1}{1+\Gamma(t)}. \tag{6.9}$$

The meaning of Eq. (6.8) is clear. It implies that the optical field will oscillate at the frequency ω_q' and decay at a rate γ, both of which depend on the index change

through Γ. By considering that $\Gamma \ll 1$, the oscillation frequency can be approximated as

$$\omega_q' \approx \omega_q \left(1 - \Gamma\right). \tag{6.10}$$

If a cavity with steady-state refractive index n_0 undergoes a spatially-uniform index change $\Delta n(t)$, then the expression for Γ in Eq. (6.7) can be approximated by $\Gamma(t) \approx \Delta n(t)/n_0$. In this case the change in oscillation frequency of the field in Eq. (6.10) can be expressed as

$$\Delta\omega = -\omega_0 \Delta n / n_0. \tag{6.11}$$

This expression for the frequency shift has been known since the first theoretical studies of AWC [126, 127], and has also been verified experimentally [128].

Equation (6.9) indicates that not only the frequency, but also the photon lifetime will be modified by the index change. As a result the energy stored in the cavity will not simply decay exponentially for $t > 0$, as would be the case in the absence of the index change. The energy as a function of time can be calculated as follows:

$$\begin{aligned}
U(t) &= \frac{1}{4}\int \left[\epsilon_0 \epsilon'(\mathbf{r},t)\left|\mathbf{E}\right|^2 + \mu_0 \left|\mathbf{H}\right|^2\right] d^3\mathbf{r} \\
&= \frac{1}{4}\int \left[\epsilon_0 \left(\epsilon + \Delta\epsilon\right)\left|\mathbf{E}\right|^2 + \mu_0 \left|\mathbf{H}\right|^2\right] d^3\mathbf{r} \\
&= \frac{|a_q|^2}{4N_q}\int \left[\epsilon_0 \left(\epsilon + \Delta\epsilon\right)\left|\mathbf{e}_q\right|^2 + \mu_0 \left|\mathbf{h}_q\right|^2\right] d^3\mathbf{r} \\
&= \left[1 + \frac{\int \Delta\epsilon |\mathbf{e}_q|^2 \, d^3\mathbf{r}}{2\int \epsilon |\mathbf{e}_q|^2 \, d^3\mathbf{r}}\right] |a_q|^2 \\
&= \left[1 + \Gamma(t)\right] |a_q|^2,
\end{aligned} \tag{6.12}$$

where definitions (6.1) and (6.7) have been used, as well as the expression for the electromagnetic field (5.12), the equality of the electric and magnetic energies of the unperturbed mode, and Eq. (5.11). This expression, when combined with the dynamic

amplitude Eq. (6.8), yields a differential equation for the mode energy,

$$\begin{aligned}\frac{dU}{dt} &= \frac{d\Gamma}{dt}|a_q|^2 + (1+\Gamma)\frac{d|a_q|^2}{dt} \\ &= \frac{d\Gamma}{dt}|a_q|^2 - 2\gamma(1+\Gamma)|a_q|^2 \\ &= -\left(\frac{d\Gamma}{dt} + \frac{1}{\tau_{ph}}\right)|a_q|^2 \\ &= -\frac{U d\Gamma/dt}{1+\Gamma(t)} - \frac{U}{\tau_{ph}^q(1+\Gamma)}. \end{aligned} \tag{6.13}$$

If we assume that $\Gamma(0) = 0$ and $U(0) = U_0$, then the solution to Eq. (6.13) is

$$U(t) = \frac{U_0}{1+\Gamma(t)}\exp\left[-\frac{1}{\tau_{ph}^q}\int_0^t \frac{dt'}{1+\Gamma(t')}\right]. \tag{6.14}$$

Clearly the electromagnetic energy stored in the cavity is not a conserved quantity. One reason for this is resonator loss, which is described by the photon lifetime in the exponential term. Equation (6.14) indicates that there is another cause of changes to the energy in addition to resonator loss. To see this more clearly, consider a time scale much shorter than the photon lifetime so that resonator losses can be neglected. In this case the exponential term in Eq. (6.14) can be replaced with 1. The energy is still not conserved because of the factor $1+\Gamma$ in the denominator, which is solely a result of changes in the refractive index. These intrinsic changes to the mode energy were first observed by Notomi and Mitsugi in Ref. [127] using numerical simulations. They observed that, while the optical energy is not conserved during AWC, the number of photons in the cavity is. The number of photons stored in the cavity as a function of time $N_p(t)$ can be calculated by using solution (6.14) and Eq. (6.9) for the photon frequency,

$$N_p(t) = U(t)/\hbar\omega_q'(t) = U_0/\hbar\omega_q. \tag{6.15}$$

Thus, the theory of this chapter indicates that the photon number is indeed the conserved quantity, in agreement with the numerical simulations.

Comparison with experiments

In order to test the theoretical model quantitatively its predictions are compared with the experimental results reported in Ref. [128]. In that experiment a silicon

ring resonator was employed as depicted in Fig. 6.1. An 18 ps input pulse (A_{in}) at the 1564 nm wavelength was resonantly coupled into the cavity. While the input pulse was trapped inside the ring a 100 fs pump pulse at the 415 nm wavelength was focused onto the resonator from above using a microscope objective. Silicon strongly absorbs light at this wavelength, and the pump pulse generated electron-hole pairs that decreased the refractive index of the cavity. The focused spot size of the pump pulse was ~10 μm, which was larger than the 6 μm diameter of the ring so that the index change was spatially uniform.

The change in refractive index is described by the semi-empirical model developed by Soref and Bennett [90]. According to this model, the index change in silicon at the 1.55 μm wavelength resulting from a free-carrier density N is given by

$$\Delta n = -\sigma_n^e N - \left(\sigma_n^h N\right)^{4/5} + i\frac{\sigma_a}{2k_0}N, \tag{6.16}$$

where $\sigma_n^e = 8.8 \times 10^{-22}$ cm^3, $\sigma_n^h = 4.6 \times 10^{-22}$ cm^3, $\sigma_a = 14.5 \times 10^{-18}$ cm^2, and $k_0 = 2\pi/\lambda$. Note that in this case Δn is complex because the generated electron-hole pairs absorb light at this wavelength. The carrier density, which is assumed to be uniform throughout the resonator, obeys the rate equation

$$\frac{dN}{dt} = \frac{\xi P_p(t)}{V_{cav}\hbar\omega_p} - \frac{N}{\tau_{fc}}. \tag{6.17}$$

Here $P_p(t)$ is the optical power of the pump pulse, ω_p is its frequency, ξ is the fraction of the pump pulse absorbed by the resonator, V_{cav} is the volume of the cavity, and τ_{fc} is the effective free-carrier lifetime. τ_{fc} is effectively infinite for our purposes since the dynamics of the probe pulse occur on a much shorter time scale.

Figure 6.1: Schematic of the silicon ring resonator used in the experiments of Ref. [128].

In the experiment measurements were taken of the transmitted field (A_t in Fig. 6.1), which is related to the mode amplitude a_q by Eq. (5.17). Both the pump and probe pulses are assumed to be Gaussian in shape and the probe pulse is additionally assumed to be free of chirp. All of the parameters necessary for modeling the experiment are taken or inferred from statements made in Ref. [128], and are recorded in table 6.1. For the majority of the simulations not a single fitting parameter was used.

Figure 6.2 compares the predictions of the model with two experimentally measured transmission spectra from Ref. [128]. In Figs. 6.2(a) and 6.2(b) the pump pulse energy was reported as being 0.419 pJ and 1.38 pJ, respectively. The spectra are normalized to the peak of the transmission spectrum in the absence of a pump pulse, allowing for quantitative comparison with the theoretical model. In both measurements there is, in addtion to the original spectral peak at a detuning of 0 nm, a second blue-shifted one. The wavelength shift from the lower pump-pulse energy, which generates fewer electron-hole pairs and induces a smaller change in the refractive index, is smaller than the wavelength shift from the larger pump-pulse energy.

Although the agreement between the experimentally measured spectra and the spectra calculated from the model is qualitatively accurate, there are some quantitative differences. For instance, the overall transmission spectrum is about 25 % lower in the simulation. Additionally, there is disagreement in the degree of overall wave-

Table 6.1: Parameters* used for the simulations shown in Figs. 6.2 and 6.3.

quality factor (Q)	18614
ring diameter	6 μm
cavity volume (V_{cav})	2.12 μm^3
probe wavelength (λ)	1.564 μm
pump wavelength (λ_p)	0.415 μm
probe pulse width	18 ps
pump pulse width	0.1 ps
absorption efficiency (ξ)	0.07
pump-probe delay	13.2 ps

*Taken or deduced from Ref. [128]

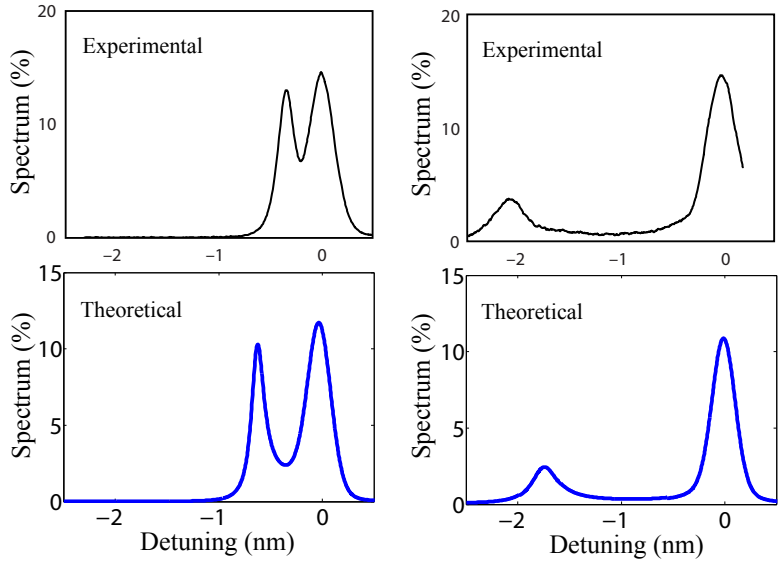

Figure 6.2: Comparison with experimental results from Ref. [128] of AWC in a silicon ring resonator for pump-pulse energies of (a) 0.419 pJ and (b) 1.38 pJ. The parameters used in the simulation were taken from [128] and are recorded in table 6.1. No fitting parameters were used.

length shift. Interestingly, this disagreement does not exhibit a uniform pattern. In Fig. 6.2(a) the theoretical degree of wavelength shift is larger than the experimental one, and in Fig. 6.2(b) it is smaller. There are many possible reasons for these discrepancies. For instance, the semi-empirical model for the refractive index change expressed in Eq. (6.16) has not been rigorously confirmed by any experiment to the author's knowledge. Also, the experimental parameters reported in table 6.1 were all measured with some degree of uncertainty. Given the number of possible sources of error and the complete absence of any fitting parameter, the degree of agreement between the theoretical and experimental spectra is remarkable in the opinion of the author.

Figure 6.3 compares the predictions of the theory with experimental observations from Ref. [128] when parameters other than the pump-pulse energy are varied. In Fig. 6.3(a) the experimental conditions are the same as for the measurements of Fig. 6.2 except for a different pump-pulse energy, which is taken to be 0.7 pJ based

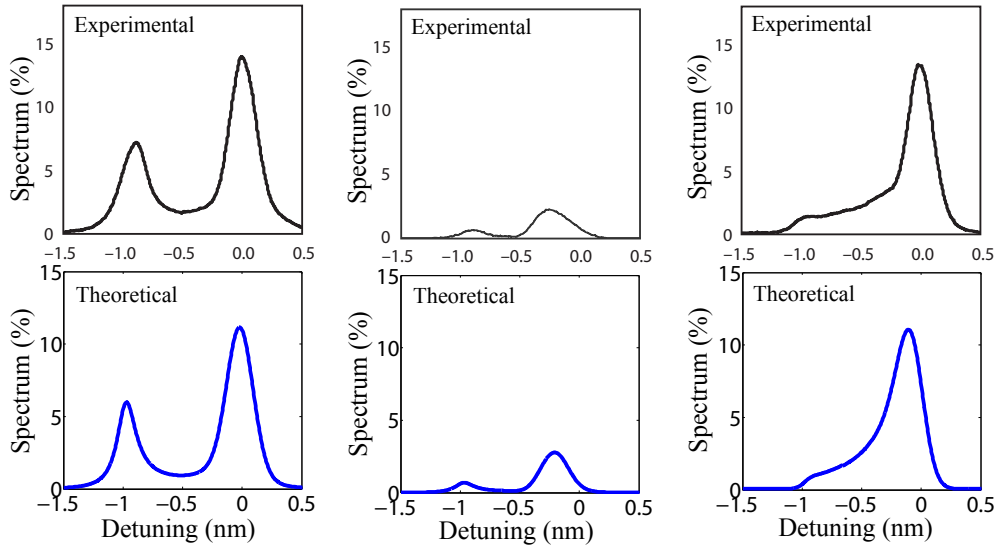

Figure 6.3: Comparison with experimental results from Ref. [128] when (a) the pump pulse energy is 0.7 pJ; (b) The probe pulse is detuned from resonance by -0.25 nm; (c) the pump pulse is broadened to a 26 ps duration. In (c) a pump-probe delay of 20 ps was chosen as a fitting parameter. All other parameters were reported in [128] and are recorded in table 6.1.

on the plot in Fig. 3 of Ref. [128]. The same pump-pulse energy was used in the measurements of Figs. 6.3(b) and 6.3(c). The difference in Fig. 6.3(b) is that the input pulse was detuned from the cavity resonance by -0.25 nm. Because the detuned probe pulse only weakly excites the cavity mode, the transmission spectrum drops uniformly. Notice that the ratio of the wavelength-shifted peak to the initial peak is approximately the same as in Fig. 6.3(a). In Fig. 6.3(c) the experimental parameters were the same as in Fig. 6.3(a), except that the pump pulse was broadened to a 26 ps duration so that the refractive-index change occured on a time scale comparable to the 15.5 ps photon lifetime of the cavity. As a result the conversion efficiency was much lower. In Fig. 6.3(c) the pump-probe delay was not reported in Ref. [128], and a value of 20 ps was chosen as a fitting parameter. No other fitting parameters were used in any of the calculations in Fig. 6.3.

6.2.2 Dynamic mode coupling

Dynamic refractive-index changes can transfer optical energy from a resonantly excited mode into neighboring modes. Even if the input beam has only a single spectral peak and couples only to one resonant mode, the index change can redistribute the optical energy among the modes so that the output beam exhibits multiple spectral peaks. We will refer to this phenomenon as dynamic mode coupling.

Interpretation of equations (6.3)

Dynamic mode coupling occurs only under specific conditions. It is described by the system of Eqs. (6.3) and occurs as a result of the off-diagonal elements of the coupling matrix (i.e. Γ_{km} for $m \neq k$), which couples the various mode amplitudes.

Transfer of energy from one mode to another can only occur appreciably if the refractive-index change happens on a time scale that is short compared to the reciprocal of the frequency spacing between those two modes, $\Delta\omega_{km} = \omega_k - \omega_m$. This is most clearly understood from the approximate form of the dynamic equations, Eq. (6.5). Since the amplitude a_k is oscillating at ω_k, then the term $i\Gamma_{km}\omega_m a_m$ that appears on the right-hand side of the equation can only influence its time development if it has a spectral component oscillating at ω_k as well. Since the amplitude a_m is oscillating at ω_m this leads to the requirement that Γ_{km}, and hence the index change $\Delta n(t)$, have spectral components at the difference frequency $\Delta\omega_{km}$. In other words, the index change must occur on a time scale that is short compared to the reciprocal of this frequency difference. If modes k and m are nearest neighbors then this is equivalent to the refractive index changing on a time scale that is short compared to the cavity round-trip time, τ_r.

A second condition necessary for the occurrence of dynamic mode coupling is that the refractive index change be spatially nonuniform. This is deduced from the expression for Γ_{km} in Eq. (6.4) and the spatial symmetry properties of the resonator modes. Consider as an example the ring resonator depicted in Fig. 6.4. In a cylindrical coordinate system with origin at the center of the ring and z-axis normal to the substrate the k^{th} mode profile can be written

$$\mathbf{e}_k(r,\theta,z) = E_k\mathbf{u}(r,\theta,z)e^{ik\theta}. \tag{6.18}$$

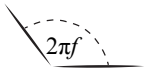

Figure 6.4: Schematic of the silicon ring resonator used in the experiments of Ref. [121].

Here $\mathbf{u}$ represents the transverse profile of the waveguide mode, which is assumed for the sake of simplicity to be independent of frequency. Note that it is only the orientation of $\mathbf{u}$ that depends on θ, and that its modulus depends only on r and z. Thus, we can choose $\mathbf{u}$ to be normalized so that $\iint r|\mathbf{u}|^2 dr dz = 1$. Using Eqs. (6.18) for the mode profiles, the coupling coefficient can be calculated from Eq. (6.4) to be

$$\Gamma_{km} = (f/n_0)\Delta n(t)\mathrm{sinc}[(m-k)\pi f]e^{i(m-k)\pi f}, \tag{6.19}$$

where $\mathrm{sinc}(x) = \sin(x)/x$. Here it has been assumed that the optical field is primarily concentrated in the waveguide core, which has refractive index n_0.

Equation (6.19) indicates that if the index change is spatially uniform (i.e. if $f = 1$) then dynamic mode coupling will not occur since $\Gamma_{km} = 0$ for all $m \neq k$ in this case. For the case $f < 1$, Eq. (6.19) provides an estimate of the number of modes that will be excited by dynamic coupling. For example, if $f = 1/3$ then a resonantly excited cavity mode can only appreciably couple to its 4 nearest spectral neighbors, 2 on the red side and 2 on the blue. For larger mode spacings Γ_{km} will be negligibly small in comparison. In the case $f \ll 1$, an estimated $1/f$ modes can be appreciably excited by dynamic coupling.

Dynamic mode coupling was explored using finite-difference time-domain simulations in Ref. [127] and demonstrated experimentally in Ref. [121]. In both of these studies the requirement of an index change that is sufficiently fast and spatially nonuniform was observed.

Comparison with experiments

Consider the experiment of Ref. [121]. It was performed by the same group that reported the observation of AWC in Ref. [128], which was studied in section 6.2.1. It was in many ways very similar to that experiment except for two key differences. First, a much larger silicon ring resonator was used so that the focused pump pulses only partially overlapped with the cavity. As a result, electron-hole pairs were only generated in a fraction of the ring and the refractive-index change was spatially nonuniform. A second difference was that a continuous-wave (CW) probe beam was used instead of a pulsed probe beam.

The theory of this chapter is used to model their experimental result by solving Eqs. (6.3) for the coupled mode amplitudes, along with the rate equation for the carrier density (6.17), which in turn gives the change in refractive index through Eq. (6.16). The output field is related to the mode amplitude by Eq. (5.19). The elements of the dynamic coupling matrix are calculated using Eq. (6.19). Two parameters necessary for modeling the experiment that were not explicity given in Ref. [121] are the pump-cavity overlap fraction f and the pump absorption efficiency ξ. If we assume that the spot size of the focused pump pulses (W_{pump}) is 10 μm as was reported previously by the same group in [128], then the pump-cavity overlap fraction can be calculated as $f = W_{pump}/\pi D$, where D is the diamater of the ring. This leads to $f = 1/30$ for the 100 μm diameter ring used in the experiment. The pump absorption efficiency can be induced by fitting the plot in Fig. 2(e) of [121], which shows the adiabatic wavelength shift of each of the cavity resonances as a function of pump-pulse energy. The expected adiabatic wavelength shift of each of the modes is $\Delta\lambda = \Gamma\lambda_0$, where $\Gamma = f\Delta n/n_0$ from Eq. (6.19). Using this expression a value of $\xi = 0.07$ is found to fit the measurement, which is exactly the same value of ξ that was reported previously by the same group in Ref. [128]. This suggests that f and ξ have been accurately induced from the reported data. The rest of the parameters used in the simulation were given in [121] and are recorded in table 6.2.

Figure 6.5 compares the measured transmission spectrum from Ref. [121] with the modeling result. The spectral peak at 1567.5 nm is from the CW probe beam that is initially on resonance with a mode of the cavity. After the arrival of a 200 fs pump pulse, part of the energy in this mode is adiabatically blue-shifted by ~1 nm to its new

Table 6.2: Parameters* used in the simulation of Fig. 6.5.

quality factor (Q)	12000
ring diameter	100 μm
cavity volume (V_{cav})	35.3 μm^3
free-spectral range	1.9 nm
probe wavelength (λ)	1.5675 μm
pump wavelength (λ_p)	0.412 μm
pump pulse width	0.200 ps
pump pulse energy (E_p)	300 pJ
absorption efficiency (ξ)	0.07
pump-cavity overlap fraction (f)	1/30

*Taken or induced from Ref. [128]

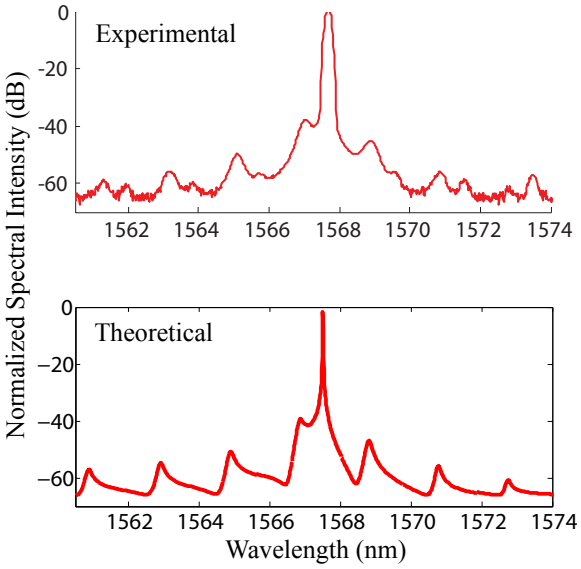

Figure 6.5: Comparison with an experimental spectrum from Ref. [121] for the case of dynamic mode coupling. All of the simulation parameters were taken or induced from statements made in [121] and are recorded in table 6.2. No fitting parameters were used.

resonance wavelength. Another part of the energy is redistributed among a number of neighboring modes. The resonance wavelengths of these modes are also blue-shifted by ~1 nm from their initial values as a result of the arrival of the pump pulse. These initial resonances can be observed in the experimental spectrum in Fig. 6.5 as a result of broadband noise in the CW input beam (most likely from an amplifier). Because the blue-shifted resonances are larger than these intial ones, it can be concluded that their existence is primarily a result of the mode coupling phenomenon, rather than from AWC. The initial resonance wavelengths are not present in the theoretical spectrum because no noise was taken into account for the input beam in the simulation. a -65 dB noise floor was, however, imposed artificially on the output beam in order to take into account as much of the experimental scenario as possible.

The relative degree of excitation of the neighboring modes predicted by the model is in good agreement with the experimental observation. One source of error in the simulations is the use of a finite number of modes. In this case 9 modes were used in the calculation in order to obtain an accurate spectrum over the 7 modes shown in Fig. 6.5. Error was observable in the bluest mode simulated (not depicted in Fig. 6.5), which exhibited a 'piling up' of spectral energy of unknown numerical origin. An additional source of error is the use of a finite time window. In the simulation, a time window of only 1.6 ns was used, which is much smaller than the 13.2 ns repetition period of the pump pulses. Despite these sources of error, the degree of quantitative agreement between the measured and simulated spectra is remarkable in the opinion of the author.

6.3 Reconfigurable wavelength conversion devices

AWC is an attractive means of implementing wavelength conversion devices for optical communications because of its potential for reconfigurability. The final wavelength of the optical field depends only on the degree of refractive-index change, which can be reconfigured by adjusting the strength of the signal that controls it. This signal could be, for example, an electrical voltage that changes the index by an electro-optic effect. It could also be an optical signal that changes the index by a nonlinear effect for all-optical wavelength conversion.

The question is, could such devices be made to perform suitably? Even before AWC was first demonstrated in resonators, it was argued that resonator-based AWC devices would suffer from inherent limitations in conversion efficiency and would also impose an unacceptable degree of pulse distortion [134]. As an alternative it was proposed [134] and later demonstrated experimentally [131] to use slow-light modes in photonic-crystal waveguides as a means of spatially confining an optical pulse for AWC. The advantage of this approach is that, in principle, the wavelength of the pulse can be converted with 100% overall efficiency while imposing negligible distortion. However, such a scheme may suffer from two practical problems. First, slow-light modes of photonic-crystal waveguides have notoriously high propagation losses [140], imposing a constraint on the achievable conversion efficiency. Second, the volume of material for which the refractive index must be changed may be significantly larger than in the resonator approach, leading to higher energy consumption. For these reasons the resonator approach to AWC may still be viable, provided that such devices can be designed to perform suitably both in principle and in practice.

In this section the question of how efficiently resonator-based AWC devices can perform in principle is addressed. In section 6.3.1 the design criteria for optimal device performance are outlined. Section 6.3.2 presents an example of a cavity design for efficient and reconfigurable AWC of optical pulses in the 1.55 μm wavelength regime.

6.3.1 Design principles

AWC is described by Eq. (6.6) for the mode amplitude a_q, along with the relations for the output fields (5.16) and (5.17). For reconfigurable conversion in a communications system at least two parameters in these equations are prescribed. The first is the input field $A_{in}(t)$, which is generally a bit stream. For simplicity we will consider only a single pulse in this bit stream. Note that this is only a realistic simplification for the case of the return-to-zero modulation format, and the considerations of this section will not be applicable to conversion of a bit stream encoded in the non-return-to-zero format. The second fixed parameter will be the overall change in refractive index [and hence the final value of $\Gamma(t)$]. This is because the device will have a prescribed target wavelength channel to which it should convert the information (in a given configuration), and this final wavelength is determined by the index change.

Equation (6.6) indicates that there are three remaining degrees of freedom that influence AWC and can be engineered for optimal device performance. The first is the cavity photon lifetime, τ_{ph}. The lifetime can be engineered by changing the strength of coupling to external fields. This could be accomplished in the ring resonator depicted in Fig. 6.1, for example, by changing the distance between the input waveguide and the ring. The second degree of freedom is the temporal profile of the refractive-index change that determines $\Gamma(t)$. As noted previously, the final value of Γ is prescribed by the application. However, the dependence of Γ on time before it reaches this final value is not prescribed and remains to be chosen. The third and final degree of freedom is the type of resonator used. Although Eq. (6.6) is very general in that it applies to all types of resonators, the coupling coefficient κ that appears in the equation depends on the resonator design. Additionally, both κ and κ^t influence the performance of the device through the output field relations of Eqs. (5.16) and (5.17). It should also be noted that this last degree of freedom is not independent of the first. The photon lifetime is related to the coupling coefficients by Eqs. (5.20), (5.21), and (5.22). When combined together these become

$$\frac{1}{\tau_{ph}} = \frac{1}{\tau_{ph}^{i}} + |\kappa|^2 + |\kappa^t|^2, \tag{6.20}$$

where the mode subscript k has been dropped since we will consider only a single mode. Thus, the three degrees of freedom are not independent of one another. We will consider each of these in their turn on conceptual grounds before demonstrating the performance capabilities of a resonator-based AWC device using numerical solutions of Eq. (6.6).

The photon lifetime

Notomi and Mitsugi first recognized that if the photon lifetime of the resonator is sufficiently long then the efficiency of the conversion of light inside the resonator will be 100% [127]. It was later pointed out by Gaburro et al. that the overall conversion efficiency of an optical pulse will be less than this since not all of the pulse will be in the resonator at the time of the refractive-index change [134]. If the photon lifetime is much longer than the temporal duration of the pulse then the spectral width of the resonance will be much narrower than the spectrum of the pulse. As a result, the

pulse will not couple efficiently into the resonator and the overall efficiency will be low. Not only this, but because of the spectral filtering imposed by the resonator the pulse will be considerably broadened in the time domain. On the other hand, if the photon lifetime is much less than the pulse duration, much of the optical field will have leaked out of the resonator before the change occurs and the efficiency will also be low, and the converted pulse duration will be much less than the incident pulse duration.

Based on these considerations we can conclude that the optimal photon lifetime is comparable to the temporal duration of the incident optical pulse. Not only this, but such a photon lifetime should simultaneously preserve the pulse duration upon conversion.

The temporal profile of the refractive index change

Notomi and Mitsugi argued that a requirement for efficient conversion is that the temporal duration of the refractive index change be much shorter than the photon lifetime [127]. This was later verified experimentally by Preble et al. [128]. Their experimental results are also included in this chapter. Figures 6.3(a) and 6.3(c) show the converted spectrum when the refractive index changes on a time scale $\ll \tau_{ph}$ and $> \tau_{ph}$, respectively. In the latter case the frequency conversion is almost unnoticeable, and the influence of the refractive-index change is better characterized as a spreading or smearing of the pulse spectrum rather than a conversion of it. Physically, the underlying reason for this is that the frequency of light inside the cavity is slaved to the value of the index change. If light is leaking out of the resonator while the index is still changing it will retain the frequency to which it was tuned at the time it left the cavity. Thus, a resonator that undergoes a refractive-index change on a time scale longer than or comparable to the photon lifetime will release light over a broad spectrum rather than cleanly converting it to a new wavelength.

These considerations lead to two basic design principles for the temporal profile of the index change. First, as pointed out by Notomi and Mitsugi, it must occur on a time scale short compared to the photon lifetime. Second, since the index change will convert all of the light trapped inside the cavity at the time that it occurs, it should initiate at a time for which the optical energy in the cavity is a maximum.

The type of cavity

One of the phenomenal things about the theoretical model of this chapter is that it makes no assumptions about the kind of dielectric cavity used for AWC. Thus, the kind of resonator used only matters in so far as it influences the parameters that appear in Eq. (6.6), as well as in Eqs. (5.16) and (5.17) for the output fields. In practice there will be other considerations for resonator design that have to do with the most efficient means of changing the refractive index, but we will not be concerned with those here. We will assume that such means have been figured out and result in the desired temporal profile for $\Gamma(t)$. The three remaining parameters are τ_{ph}, κ, and κ^t, which are related by Eq. (6.20). Because we are interested in the optimal conversion efficiency attainable, we will assume that the photon lifetime is mainly determined by coupling losses, and that intrinsic losses resulting from material absorption and scattering are negligible in comparison. This situation corresponds to an 'overcoupled' cavity, and mathematically it means the quantity $1/\tau_{ph}^i$ that appears in Eq. (6.20) is much smaller than the coupling terms so that this equation can be approximated as

$$\frac{1}{\tau_{ph}} \approx |\kappa|^2 + |\kappa^t|^2. \tag{6.21}$$

In this case the photon lifetime is entirely determined by the coupling coefficients. This imposes a constraint on the coupling coefficients since, as we determined earlier, the photon lifetime should be chosen to be approximately equal to the duration of the input pulse.

The one choice left to make regarding the cavity is how many output ports to use. It is conceivable to have any number of output ports, but we will limit our discussion to the most common cases of having either 1 or 2 of them, as was done in section 5.1.3. These two cases correspond to resonators of the Gires–Tournois and Fabry–Perot types, respectively. Examples of Gires–Tournois type resonators are shown in Fig. 6.6(a). The sole output port of a Gires–Tournois resonator is always a reflection port. This is unavoidable because of the necessity of having an input coupler. Examples of Fabry–Perot type resonators are shown in Fig. 6.6(b). The second output port of the Fabry-Perot will be assumed to be a transmission port, which is the most common case. It might be expected on intuitive grounds that the

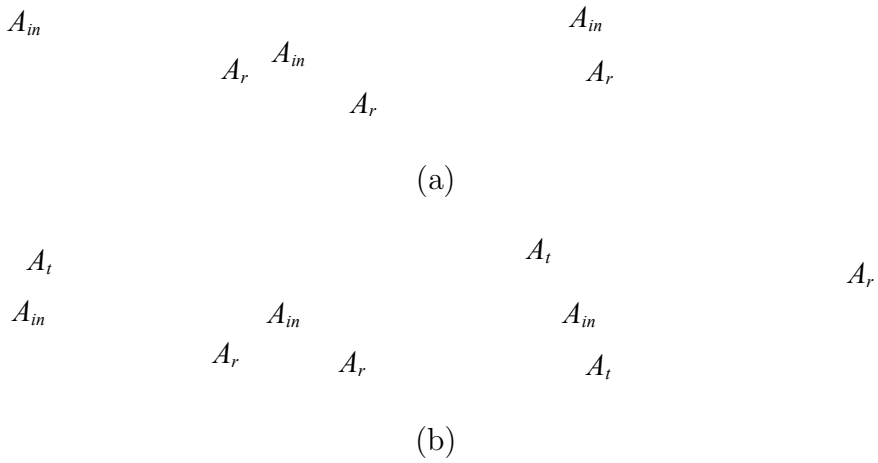

Figure 6.6: (a) Examples of Gires–Tournois resonators; (b) examples of Fabry–Perot resonators

Gires–Tournois cavity will exhibit a superior conversion efficiency when compared to that of the Fabry–Perot since its output is all channeled into a single port, whereas the Fabry–Perot's output is shared between two ports. This conclusion is correct, as will be shown, but the comparison between the two is more complicated than this thinking suggests.

For the Gires–Tournois cavity $\kappa^t = 0$ and Eq. (6.21) dictates that $\kappa = 1/\sqrt{\tau_{ph}}$. For the Fabry–Perot $\kappa^t \neq 0$ and a choice remains about the relative values of κ and κ^t that will optimize the conversion efficiency at the transmission port. Noting that the transmitted field is linearly proportional to κ^t from Eq. (5.17), and that the excitation of the mode amplitude (and hence the transmitted field) is proportional to κ from Eq. (6.6), we conclude that the transmitted field is proportional to the product $\kappa\kappa^t$. Therefore, the energy in the converted pulse E_t, which depends on the modulus-squared, can be expressed

$$E_t = \alpha|\kappa\kappa^t|^2, \tag{6.22}$$

where α is a constant of proportionality. Because κ and κ^t are constrained by Eq. (6.21), we can express the converted pulse energy in terms of only one of them,

$$E_t = \alpha|\kappa^t|^2\sqrt{1/\tau_{ph} - |\kappa^t|^2}. \tag{6.23}$$

This function is maximized when $|\kappa^t|^2 = 1/2\tau_{ph}$. Thus, when

$$\kappa^t = \kappa = 1/\sqrt{2\tau_{ph}} \tag{6.24}$$

the conversion efficiency of the Fabry–Perot device will be maximized.

Figure 6.7(a) compares the performance of the Fabry–Perot and Gires–Tournois cavities. In the simulations parameters were chosen to optimize the efficiency of each of the resonators. The photon lifetime was chosen to be comparable to the input pulse width. More specifically, $\tau_{ph} = T_0$ for a Gaussian pulse shape given by

$$A_{in}(t) = A_0 e^{-1/2(t/T_0)^2 - i\omega_0 t}. \tag{6.25}$$

The refractive-index change was initiated at a time for which the energy in the cavity was maximum (this time is the same for both cavities), and its duration was chosen to be only 5% of the photon lifetime. The temporal profile of the index change had a linear slope as shown in the inset of Fig. 6.7(b). The coupling coefficients are chosen

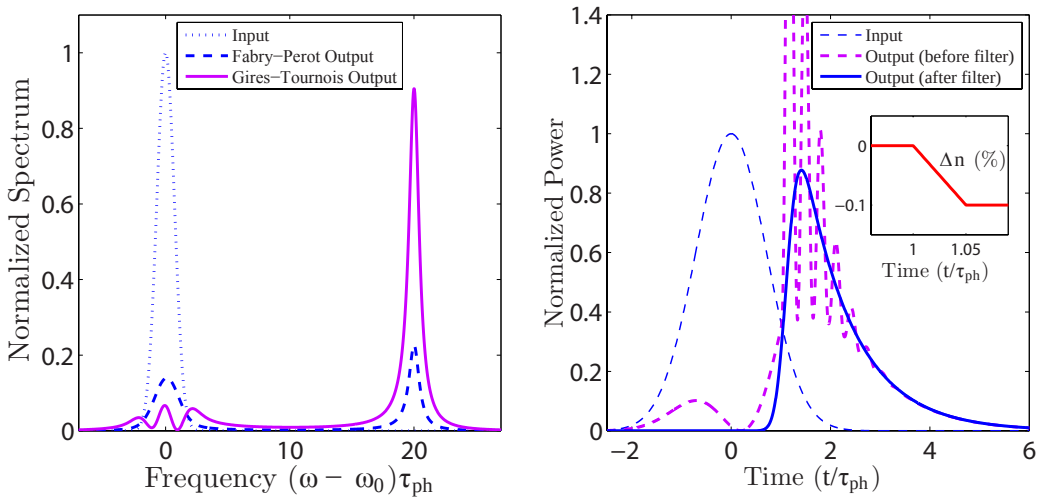

(a) (b)

Figure 6.7: Comparison of Fabry–Perot and Gires–Tournois resonators when used for AWC. (a) Comparison of the input and converted spectra for each of the devices; (b) Comparison of the input pulse shape with the output pulse from the Gires–Tournois device both before and after a spectral component at the initial resonance is filtered out. The temporal profile of the refractive index change is shown in the inset.

to be those given by Eq. (6.24) for the Fabry–Perot. For the Gires–Tournois $\kappa^t = 0$ and $\kappa = 1/\sqrt{\tau_{ph}}$ as discussed earlier. The quality factor (Q) of the cavity was chosen to be 20,000, a typical experimental value [128, 129].

Evident from Fig. 6.7(a) is the superior performance of the Gires–Tournois cavity. The overall conversion efficiency can be calculated by filtering each of the output spectra to remove a spectral component at the initial cavity resonance and then integrating to obtain the converted energy. The efficiency of the Gires–Tournois device is found to be 74.32%, whereas the efficiency in both the transmission port and reflection port of the Fabry–Perot is 18.58%. Thus, the Gires–Tournois' efficiency is 4 times the Fabry–Perot's. There are two reasons for this. One of these is a factor of 2 that results from the fact that the Fabry–Perot shares its output between two ports whereas the Gires–Tournois does not. The other factor of 2 has more subtle origins. It results from the fact that, in order for the photon lifetime to be the same in both cases, the input coupling coefficient κ must be $\sqrt{2}$ times as large for the Gires–Tournois device. This translates into a factor of 2 greater pulse energy coupled into the resonator, and hence converted to the new wavelength. Simulations also show that by choosing a slightly different photon lifetime the conversion efficiency can be enhanced, but that the degree of this enhancement is negligible (<0.2%). It may also be the case that alternative pulse shapes (rather than the Gaussian) might enhance this efficiency somewhat, but this enhancement is unlikely to be very large. It thus appears that the simulation shown in Fig. 6.7(a) approaches a fundamental limit to the wavelength conversion efficiency achievable by AWC of an optical pulse in a resonator.

The only question that remains is whether or not the pulse duration is preserved in the AWC process. Figure 6.7(b) shows that, by a stroke of good fortune, this happens to be the case for the Gires–Tournois cavity with optimized conversion efficiency whose spectrum is shown in Fig. 6.7(a). Shown in 6.7(b) are the converted pulse shapes before and after being passed through a Gaussian filter to remove a spectral component at the original cavity resonance. Before the filter these two frequency components beat together to produce intensity oscillations, but after the filter a clean pulse shape is obtained with a temporal duration nearly equal to that of the input pulse.

6.3.2 An example

In section 6.3.1 the design principles of an AWC device were outlined, and an example was presented in Fig. 6.7 showing frequency conversion of a pulse to a specific target frequency (20 cavity linewidths away from the original resonance). The purpose of this section is to consider the performance capabilities of such a device when used for conversion to a variety of target frequencies, such as would be the case if it were used reconfigurably. In order to make the example more concrete the use of normalized units will be abandoned in favor of standard units.

Figure 6.8 shows the results of simulations demonstrating the performance of an AWC device for conversion of a 40 ps input pulse to a number of different frequencies, each spaced at integer multiples of 50 GHz away from the initial carrier frequency. The cavity design and simulation parameters are similar to those used in Fig. 6.7, with some differences. The input pulse is assumed to be Gaussian and given by Eq. (6.25). The photon lifetime is chosen so that $\tau_{ph} = T_0$, leading to a 24 ps photon lifetime for the 40 ps full-width-at-half-maximum input pulse. The Q factor for a cavity having such a lifetime at the 1550 nm wavelength is $\approx 29,000$. The magnitude of the maximum refractive-index change is 0.155% for the furthest channel spacings of ±300 GHz. The duration of the index change is chosen to be 5% of the photon lifetime for all channel spacings and is shown in the inset of Fig. 6.8(a) for the upconverted frequencies. After the conversion, all of the pulses are passed through 50 GHz (full-width-at-half-maximum) Gaussian filters.

Figure 6.8 demonstrates that the device performance can be virtually independent of the extent of frequency conversion. Fig. 6.8(b) shows the temporal profiles of the 6 upconverted pulses investigated in the simulations after they have been passed through the 50 GHz filters. The temporal profiles are relatively independent of the final frequency, meaning that both their conversion efficiency and pulse shape are the same. The pulse that was converted by only one channel spacing (50 GHz) exhibits some distortion as a result of a spectral component at the original resonance frequency that is not completely eliminated by the filter. All of the other pulse shapes are identical. Figure 6.8(c) shows that not only the temporal profiles of the pulses but also their spectral shapes are nearly identical. Also shown in Fig. 6.8(c) are downconverted pulses that are obtained by applying similar refractive-index changes

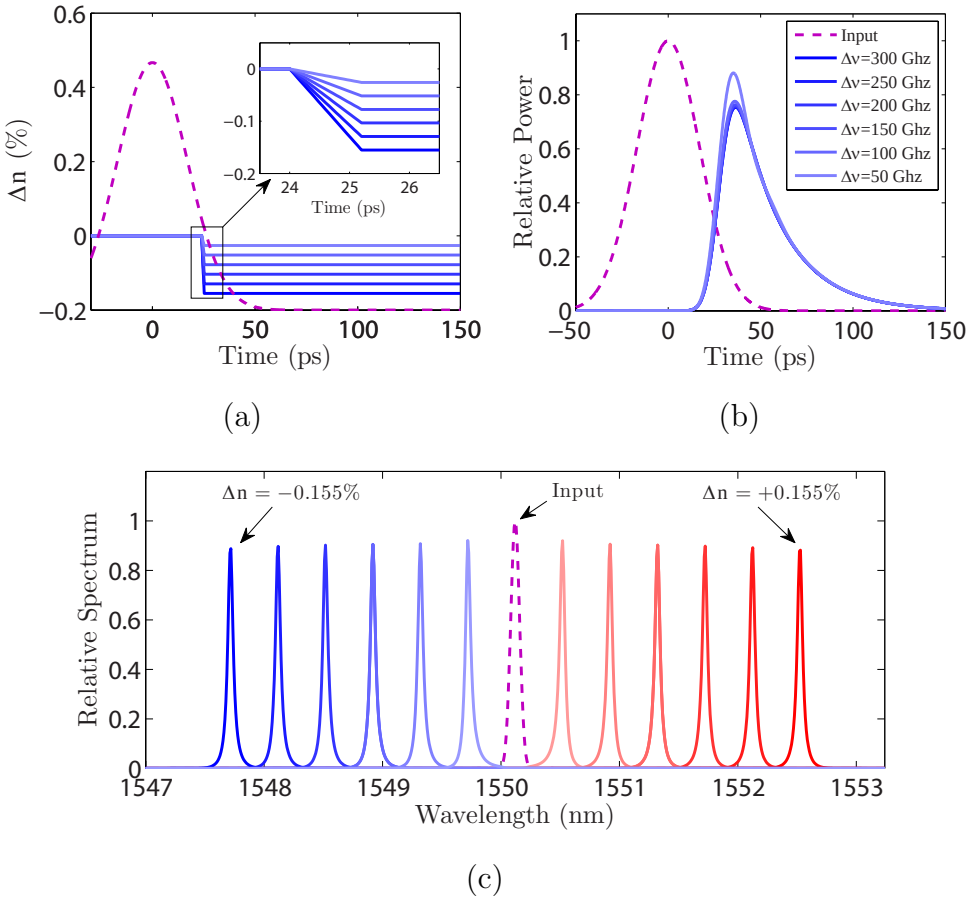

Figure 6.8: Example of a reconfigurable AWC device. (a) Input pulse shape (dashed curve) and temporal profile of the refractive-index changes for each of the upconverted pulses; (b) Comparison of the input with the converted pulse shapes after passing through 50 GHz filters; (c) Input and output spectra for each of the configurations. The final wavelength in each configuration is determined by the value of the index change.

as shown in Fig. 6.8(a), except that the sign is flipped (the index changes are positive in this case).

The performance potential for reconfigurable AWC devices laid out in this section demonstrate that they could conceivably be designed to operate efficiently. However, there are a number of practical issues that remain to be addressed before such devices could be realized. For example, the issue of timing of the index change. The example of Fig. 6.8 assumed that the index change occured over a time of less than 2 ps, which

may not be practical. Additionally, it was assumed that the index change initiated at just the right time for optimal conversion efficiency, and a mechanism for timing the signal to the input pulse would be needed to implement this in reality. Finally, the converted pulses in the simulations are delayed from those of the input by about one pulse width. Thus, it is not clear how such a device could convert two consecutive pulses in an optical bit stream. It may be that some sacrifice in conversion efficiency could remove this obstacle, or that the device could be used to convert alternate pulses for time-division demultiplexing applications, but it may also be the case that this difficulty proves insurmountable. What the simulations of this section really show, then, is not that reconfigurable AWC devices are achievable but that methods for overcoming these obstacles may be worth pursuing.

6.4 Summary

In this chapter a comprehensive theory of dynamic refractive-index changes in optical resonators was developed, which describes the dynamics of the optical field when the index is changed by some external means such as an electro-optic effect. The theory describes two distinct wavelength conversion processes. The first is AWC, which is a tuning of the optical frequency of light by the index changes while it is trapped inside a single mode of the cavity. The second is dynamic mode coupling, which is the transfer of optical energy of light from one mode into many different modes at different frequencies. The theory was shown to reproduce the results of experiments in the literature of both of these phenomena with both qualitative and quantitative accuracy. It was then applied to consider the possibility of using AWC for reconfigurable wavelength conversion devices. The design criteria of such devices were clarified, and it was shown that they are able in principle to convert the wavelength of optical pulses with $> 74\%$ overall efficiency while nearly preserving their temporal duration. Their performance was further shown to be relatively independent of the extent of wavelength conversion in each configuration.

7 Phase-switched two-input Kerr flip-flops

Optical flip-flops have the potential to be used for buffering in communications systems as well as for memory elements in future all-optical computers. They're typically realized by using bistability in resonators, which requires a nonlinear material response. The three most common means of implementing bistability are the Kerr effect, free-carrier dispersion in semiconductor devices, and thermal nonlinearities. Of these the Kerr effect is the fastest, having an almost instantaneous material response time. As a result the switching speed of Kerr flip-flops is not limited by the nonlinear medium but by the photon lifetime of the cavity, which can be engineered. For this reason the Kerr effect may become the most desirable means for implementing optical flip-flops at some point in the future. At present, their implementation in microresonator cavities is facing serious practical challenges. Optical absorption inevitably heats the cavity and changes the refractive index via the thermo-optic effect [141, 142]. As a result the nonlinear response is dominated by the much stronger and slower thermal nonlinearity, and switching between the 'on' state (for which the cavity is full of light) and the 'off' state (for which it is empty) is limited to μs time scales [141]. Two-input bistability, for which the cavity is equally full of light in both stable states, has the potential to circumvent thermal limitations. Such a device could be flipped between its two stable states on time scales that are much shorter than the thermal response time. As a result the thermally-induced index changes, being unable to respond fast enough, would behave as an essentially constant background.

Figure 7.1 describes two-input bistability conceptually. Two distinct resonator modes are excited by two different input beams. In Fig. 7.1(a) these modes are spa-

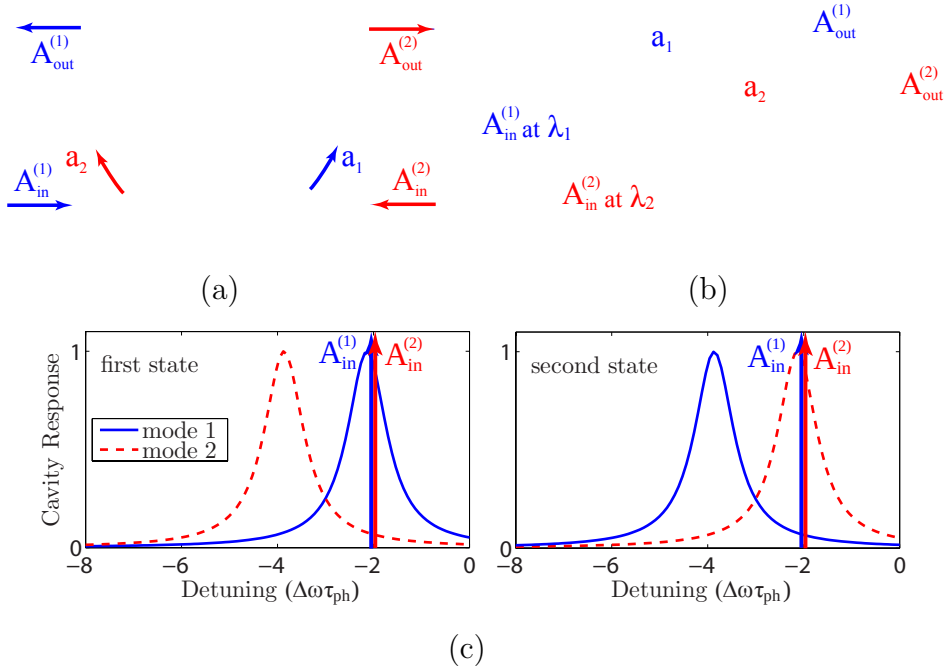

Figure 7.1: A description of two-input Kerr bistability. (a) a configuration with two spatially distinct modes; (b) a configuration with two spectrally distinct modes; (c) a conceptual explanation of the two stable states in either configuration.

tially distinct; one is a clockwise-propagating mode and the other is a counterclockwise-propagating mode. Figure 7.1(b) shows an alternative configuration where the two modes are spectrally distinct, having different resonance wavelengths at λ_1 and λ_2. In both configurations the physical mechanism that leads to two-input bistability is the asymmetry between Kerr-induced self- and cross-phase modulations, the latter being twice as large as the former. If the mode a_1 is intense enough self-phase modulation can cause it to experience a nonlinear change in refractive index, Δn_{NL}. This results in a shift of its resonance frequency by an amount $-\omega_1 \Delta n_{NL}/n_0$, where ω_1 and n_0 are the low-intensity resonance frequncy and refractive index of the medium, respectively. However, the change in refractive index experienced by mode a_2 through cross-phase modulation will be twice as much, and its resonance frequency will shift by an amount $-2\omega_2 \Delta n_{NL}/n_0$. If the two input beams $A_{in}^{(1)}$ and $A_{in}^{(2)}$ are equally intense and equally detuned from resonance this can lead to the existence of two stable states, as described in Fig. 7.1(c). In the first state, input beam 1 (depicted by a blue arrow) is

on resonance and fills the cavity with light in mode a_1 so that the transmission of beam 1 is high. Input beam 2 (depicted by a red arrow), however, is off resonance and only weakly excites mode a_2 so that its transmission is low. In the second state, the roles of beams 1 and 2 are reversed.

Two-input bistability in a ring resonator was investigated by Agrawal in the early 1980's [143,144]. The focus of this work was absorptive bistability, but Kerr bistability was also discussed and it was suggested to have a significant influence on the Sagnac effect [144]. This suggestion was later taken up by Kaplan and Meystre who analyzed the concept in detail and found that the effect would indeed enhance the sensitivity of Sagnac measurements [145]. A later work of theirs that considered a non-rotating ring resonator represents the first detailed study of the operating regimes of two-input Kerr bistability [146]. Haelterman et al. considered the same phenomena in a Fabry-Perot etalon where the two inputs were beams distinguished by propagating at different angles [147, 148]. Haelterman later developed a dynamic theory of this same structure and numerically demonstrated flip-flop operation by modulating the intensities of the two input beams [149]. No experimental demonstration of two-input Kerr bistability has been reported to the author's knowledge.

While most studies of single-input Kerr flip-flops have considered switching by intensity modulations of the input beam, it was pointed out as early as 1979 that the phase properties of the field can play a dramatic role in the switching process [150]. In this work, a dynamic theory of the mode amplitude was developed and it was argued that the device performance might suffer from anomalous switching mechanisms that result from phase variations in the input field [151, 152]. In Ref. [151] the model of Ref. [150] was adopted to show that a pulse with the appropriate phase and amplitude, when coherently combined with the input field, can switch the device both on and off almost instantaneously even for high Q cavities. In Ref. [152] a similar equation was used to show that the pulse power required for intensity modulation switching of a bistable photonic-crystal microresonator can be reduced by engineering its spectral phase structure. This last work also showed excellent agreement between the mode amplitude equation and finite-difference time-domain simulations. No experimental study of the role of input-beam phase in switching single-input Kerr flip-flops has been reported to the author's knowledge.

In this chapter it is proposed to use pure phase modulation as a mechanism for switching two-input Kerr flip-flops. In section 7.1 the theoretical methodology of chapter 5 is used to derive the dynamic equations for two modes in a Kerr resonator. The equations derived are valid for all types of dielectric cavities with Kerr media and rigorous expressions are found for the nonlinear parameters. Thus, section 7.1 provides a general theoretical foundation for the equations used in Ref. [149] for two-input nonlinear resonators, as well as the equation used in Refs. [150–152] for the single-input case. In section 7.2 the equations are applied to two-input bistability, and the appropriate biasing conditions of the flip-flop are clarified. In section 7.3 the phase-switched device is proposed and verified by numerical simulations. Additionally, a model of the thermodynamics of the device is developed and used to formulate criteria for suitable materials and cavity designs. Section 7.4 summarizes the results of this chapter.

7.1 Governing equations

The influence of the Kerr effect on the electromagnetic field in the cavity is modeled using the dynamic mode-amplitude Eq. (5.15), where the nonlinear dipole-moment density results from the Kerr effect. In other words $\mathbf{P}^{NL} = \mathbf{P}^{(3)}$, where $\mathbf{P}^{(3)}$ describes the interaction of the field with the third-order susceptibility of the medium. By making the approximation $\partial\mathbf{P}^{(3)}/\partial t \approx -i\omega_k\mathbf{P}^{(3)}$ Eq. (5.15) becomes

$$\frac{da_k}{dt} = -i\omega_k a_k - \frac{1}{2\tau_{ph}}a_k + \kappa A_{in}^{(k)}(t) + \frac{i\omega_k}{4\sqrt{N_k}}\int \mathbf{e}^{*(k)}\cdot\mathbf{P}^{(3)}\,d^3\mathbf{r}. \tag{7.1}$$

The third-order dipole moment density can be written in terms of the third-order susceptibility tensor and the electric field as [65, 87]

$$P_\mu^{(3)}(\mathbf{r},t) = \frac{3\varepsilon_0}{4}\sum_{\alpha,\beta,\gamma}\chi_{\mu\alpha\beta\gamma}^{(3)}\left(\omega_0;\omega_0,-\omega_0,\omega_0\right)\,E_\alpha(\mathbf{r},t)E_\beta^*(\mathbf{r},t)E_\gamma(\mathbf{r},t). \tag{7.2}$$

The electric field is given from Eq. (7.2) as

$$\mathbf{E}(\mathbf{r},t) = \sum_m \frac{a_m(t)}{\sqrt{N_m}}\mathbf{e}_m\left(\mathbf{r}\right). \tag{7.3}$$

The governing equations are found by combining Eqs. (7.3), (7.2), and (7.1) for the two modes considered. The result is a pair of coupled nonlinear mode amplitude equations,

$$\frac{da_1}{dt} = -i\omega_1 a_1 - \frac{1}{2\tau_{ph}} a_1 + \kappa A_{in}^{(1)}(t) + i(\gamma_{11}|a_1|^2 + 2\gamma_{12}|a_2|^2)a_1, \tag{7.4}$$

$$\frac{da_2}{dt} = -i\omega_2 a_2 - \frac{1}{2\tau_{ph}} a_2 + \kappa A_{in}^{(2)}(t) + i(\gamma_{22}|a_2|^2 + 2\gamma_{21}|a_1|^2)a_2. \tag{7.5}$$

In deriving Eqs. (7.4) and (7.5) no specific configuration of the two-input device has been assumed. As a result they describe both the device depicted in Fig. 7.1(a) and the device depicted in Fig. 7.1(b), as well as any other two-mode configuration. It should be noted that 5 nonlinear terms in each equation have been neglected. If one considers the two modes to be at different resonance frequencies as in Fig. 7.1(b), then this is done by making the rotating-wave approximation because they are not frequency-matched to the mode in question. On the other hand, if the two modes share the same resonance frequency but are spatially distinct as in Fig. 7.1(a), then the terms are neglected because they are equal to zero or approximately so as a result of the spatial phase structure of the counterpropagating modes.

The values of the parameters in Eqs. (7.4) and (7.5) depend on the structure of the cavity used and the modes that it supports. The nonlinear γ parameters are given by

$$\gamma_{kl} = \frac{\omega_k n_2 c \eta_{kl}}{n_0^2 (V_k V_l)^{1/2}}, \tag{7.6}$$

where V_k is the *effective mode volume* of the kth mode and is given by

$$V_k = \frac{\left(\int \epsilon(\mathbf{r}) \left|\mathbf{e}^{(k)}\right|^2 d^3\mathbf{r}\right)^2}{n_0^4 \int \left(\left|\mathbf{e}^{(k)}\right|^2\right)^2 d^3\mathbf{r}}. \tag{7.7}$$

The terms η_{kl} are *nonlinear overlap factors* that measure how the modes interact through the third-order susceptibility tensor,

$$\eta_{kl} = \sum_{\mu\alpha\beta\gamma} \frac{\int \chi^{(3)}_{\mu\alpha\beta\gamma} e^{*(k)}_{\mu} e^{(k)}_{\alpha} e^{*(l)}_{\beta} e^{(l)}_{\gamma} \, d^3\mathbf{r}}{\chi_c^{(3)} \left[\int \left(\left|\mathbf{e}^{(k)}\right|^2\right)^2 d^3\mathbf{r} \int \left(\left|\mathbf{e}^{(l)}\right|^2\right)^2 d^3\mathbf{r}\right]^{1/2}}. \tag{7.8}$$

Here the susceptibility tensor has been normalized to one of its components, $\chi_c^{(3)}$. Often this is chosen to be $\chi_c^{(3)} = \chi_{1111}^{(3)}$, where $\chi_{1111}^{(3)}$ is in the crystallographic coordinate system so that the n_2 in Eq. (7.6) is the intensity-dependent refractive index of a

wave polarized along the x-axis of that system (they're related by $\chi_c^{(3)} = 4\varepsilon_0 c n_0^2 n_2/3$). It should also be noted that n_0 in Eq. (7.6) is the low-intensity refractive index of the Kerr material in the resonator, and it is assumed that only one kind of Kerr material dominates the nonlinear response (i.e. nonlinear inhomogeneity is not considered here). In many cases Eqs. (7.4) and (7.5) can be simplified by making the approximations $\eta_{kl} \approx 1$ and $V_1 \approx V_2$ so that $\gamma_{11} \approx \gamma_{22} \approx \gamma_{12} \approx \gamma_{21} = \gamma$ for a lossless nonlinear medium. This will be assumed throughout the rest of this chapter.

7.2 Two-input bistability

We have presumed on conceptual grounds that the two-input Kerr device can be biased such that there are two stable states like the ones described by Fig. 7.1(c). That intuition will be rigorously verified in this section by finding the steady-state solutions of Eqs. (7.4) and (7.5) and examining their stability. For an input field coupled to mode k and oscillating at frequency ω_{0k}, the steady-state solutions correspond to constants B_k and b_k given by

$$A_{in}^{(k)}(t) = B_k\, e^{-i\omega_{0k}t}, \tag{7.9}$$

$$a_k(t) = b_k\, e^{-i\omega_{0k}t}. \tag{7.10}$$

Equations (7.4) and (7.5) then lead to a pair of algebraic equations for the complex constants b_k,

$$\left[-i\left(\Delta\omega_k + \gamma|b_k|^2 + 2\gamma|b_{3-k}|^2\right) + 1/2\tau_{ph}\right] b_k = \kappa B_k, \tag{7.11}$$

where $k = 1$ or 2 and $\Delta\omega_k = \omega_{0k} - \omega_k$. Taking the modulus squared of these two equations leads to a pair of algebraic equations relating the real mode energies $E_k = |b_k|^2$ to the input beam powers $P_k = |B_k|^2$,

$$\left[\left(\Delta\omega_k + \gamma E_k + 2\gamma E_{3-k}\right)^2 + \left(1/2\tau_{ph}\right)^2\right] E_k = |\kappa|^2 P_k. \tag{7.12}$$

Note that there is a one-to-one correspondence between the solutions of Eqs. (7.12) and the solutions of Eqs. (7.11). In other words, Eqs. (7.12) are not only a necessary condition for Eqs. (7.11) but also a sufficient one. After solving (7.12) for the mode energies, the solutions can be used in (7.11) to find the mode phases.

In general Eqs. (7.12) are not easy to solve. For given biasing conditions, corresponding to given input-beam detunings $\Delta\omega_k$ and input-beam powers P_k, they form a pair of coupled cubic equations for the mode energies. In practice the solutions are plotted using numerical tricks. Once the solutions are found, however, Eqs. (7.12) do not guarantee their stability.

7.2.1 Stability analysis

The steady-state solutions of Eqs. (7.12) are not useful for biasing a flip-flop unless they are also stable. A steady-state solution is unstable if the system tends to evolve away from it. In other words, if a small perturbation is applied (such as occurs regularly in practice), then the system will evolve away from an unstable state. The stability of the steady-state solutions of Eqs. (7.11) can be analyzed using Eqs. (7.4) and (7.5). Assume that there is a solution to the equations given by

$$a_k(t) = b_k \left[1 + c_k(t)\right] e^{-i\omega_{0k}t}, \tag{7.13}$$

where b_k is a solution to Eqs. (7.11) and $c_k(t)$ is a small perturbation to the solution so that $|c_k| \ll 1$. By using this assumed solution in Eqs. (7.4) and (7.5), and keeping only the terms up to first order in c_k, a system of four coupled differential equations is found for c_k and their complex conjugates,

$$\frac{d\mathbf{c}}{dt} = \overleftrightarrow{\boldsymbol{S}}\,\mathbf{c}, \tag{7.14}$$

where

$$\mathbf{c} = \begin{pmatrix} c_1 \\ c_2 \\ c_1^* \\ c_2^* \end{pmatrix}. \tag{7.15}$$

The matrix $\overleftrightarrow{\boldsymbol{S}}$ that appears in Eq. (7.14) is given by

$$\overleftrightarrow{\boldsymbol{S}} = \begin{pmatrix} i\left[\Delta\omega_1 + 2\gamma\left(E_1+E_2\right)\right] - 1/2\tau_{ph} & i2\gamma E_2 & \\ i2\gamma E_1 & i\left[\Delta\omega_2 + 2\gamma\left(E_1+E_2\right)\right] - 1/2\tau_{ph} & \cdots \\ -i\gamma E_1 & -i2\gamma E_2 & \\ -i2\gamma E_1 & -i\gamma E_2 & \end{pmatrix}$$
$$\cdots \begin{pmatrix} i\gamma E_1 & i2\gamma E_2 \\ i2\gamma E_1 & i\gamma E_2 \\ -i\left[\Delta\omega_1 + 2\gamma\left(E_1+E_2\right)\right] - 1/2\tau_{ph} & -i2\gamma E_2 \\ -i2\gamma E_1 & -i\left[\Delta\omega_2 + 2\gamma\left(E_1+E_2\right)\right] - 1/2\tau_{ph} \end{pmatrix}, \tag{7.16}$$

where the E_k are the mode energy solutions of (7.12) whose stability is being examined. The stability of the state is determined by evaluating the eigenvalues of the matrix $\overleftrightarrow{\boldsymbol{S}}$. The eigenvectors $\mathbf{c}_m$ with eigenvalues Ω_m satisfy

$$\overleftrightarrow{\boldsymbol{S}}\,\mathbf{c}_m = \Omega_m \mathbf{c}_m, \tag{7.17}$$

and any solution of (7.15) can be written as a linear combination of the solutions $\mathbf{c}_m e^{\Omega_m t}$. Thus, a solution is stable if for all of the eigenvalues of its $\overleftrightarrow{\boldsymbol{S}}$ matrix

$$\mathrm{Re}\left\{\Omega_m\right\} < 0. \tag{7.18}$$

In practice the eigenvalues cannot be found by analytical means. Rather, they are evaluated numerically for each solution to determine its stability. Before this can be done, however, the steady-state solutions must be found.

7.2.2 Stable steady-state solutions

It is possible to bias the device asymmetrically, so that the detunings and power levels of the two inputs may differ. However, we are interested in finding a pair of stable states for which the temperature, and hence the cavity energy, is the same in both states. Thus, not only is there no apparent advantage to using asymmetric biasing but there is an apparent disadvantage. Therefore, we will consider the simplest case of symmetric biasing. This is the case that was analyzed by Kaplan and Meystre in

Ref. [146]. Because the analysis is involved it is not reproduced here but in appendix E. It is performed by finding steady-state solutions of Eqs. (7.12), where $P_1 = P_2 = P_0$ and $\Delta\omega_1 = \Delta\omega_2 = \Delta\omega_0$ for symmetric biasing, and then evaluating their stability by using the method described in section 7.2.1. The final insight drawn is a crucial device design criterion: the set of available biasing conditions for which the flip-flop will work. Figure 7.2 shows such bias points in the $(\Delta\omega_0, P_0)$ plane. The suitable bias points are defined by the purple shaded region. Their suitability is determined by their exhibiting only a single pair of stable asymmetric solutions of Eqs. (7.12) such as the ones shown in Fig. 7.1(c). The device will work for any of these points but in the rest of this chapter we will focus on one with $\Delta\omega_0\tau_{ph} = -2$ and $4\gamma|\kappa|^2\tau_{ph}^3 P_0 = 2$.

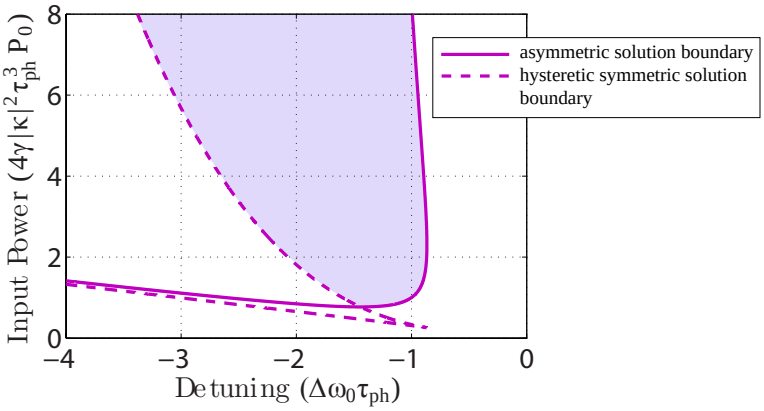

Figure 7.2: Biasing regimes for the flip-flop device in the ($\Delta\omega_0$,P_0) plane after Ref. [146]. The purple shaded region shows the set of ideal bias points where only two stable states such as the ones described in Fig. 7.1(c) exist.

7.3 Phase-switched memory devices

In 1991 Haelterman numerically demonstrated flip-flop operation of the two-input bistable resonator by modulating the intensities of the two input beams for set and reset operations [149]. Specific designs and/or applications of the device have not been conceived (indeed the two-input device has not even been demonstrated experimentally), so it is difficult to say whether or not intensity modulation would be the most practical switching mechanism. If set and reset operations could be realized

by applying pure phase modulations to the input beams (so that their intensities are kept constant) this may be a more technologically simple way to realize flip-flop operation. In this section we demonstrate numerically that pure phase modulations can indeed be used to achieve both set and reset operations. Such phase modulations could be implemented either electro-optically (e.g. the Pockel's effect) or all-optically (e.g. cross-phase modulation by set/reset pulses) but we will not assume a specific mechanism in the analysis of this section.

The principle behind phase switching can be understood by considering the nature of the stable states of the system when biasing conditions deviate from symmetry. Consider, for example, a device that is initially biased symmetrically so that it is in the second state depicted in Fig. 7.1(c) and input beam 2 is on resonance and fills the cavity with light. If the detuning of beam 2 increases (so that the red arrow shifts to the right in the figure) while its power level is kept constant, the energy in mode 2 will be forced to decrease. As a result cross-phase modulation will no longer be able to hold the resonance of mode 1 at bay and input beam 1 will begin to fill the cavity with light. After the cavity fills up with light in mode 1, the resonance of mode 2 will be pushed to negative detunings. The cavity will then empty of light in mode 2 and after the detuning of beam 2 is brought back to its bias value, the device will have flipped to the first state depicted in Fig. 7.1(c). A reset operation that flops the device can be realized in an exactly analogous way by modulating the detuning of input beam 1.

This intuitive understanding of the switching process is verified mathematically in Fig. 7.3. The figure shows the available stable states of the system when the detuning of input beam 2 ($\Delta\omega_2\tau_{ph}$) deviates from its bias value of -2. In the calculations the detuning of input beam 1 is kept constant at -2 and the input powers of both beams are equal and fixed so that $4\gamma|\kappa|^2\tau_{ph}^3 P_0 = 2$. For values of $\Delta\omega_2\tau_{ph}$ less than -2 the stable states of the system exhibit complicated behavior. For values greater than -2 they are much simpler. When the detuning is slightly larger than -2 there exists a region where the only available state is one for which the transmission of input beam 1 is high and input beam 2 is low (shaded in purple in the figure). If the device were initially in a state for which the transmission of beam 2 were high and the transmission of beam 1 low, then a temporary increase of the input beam 2's detuning into this

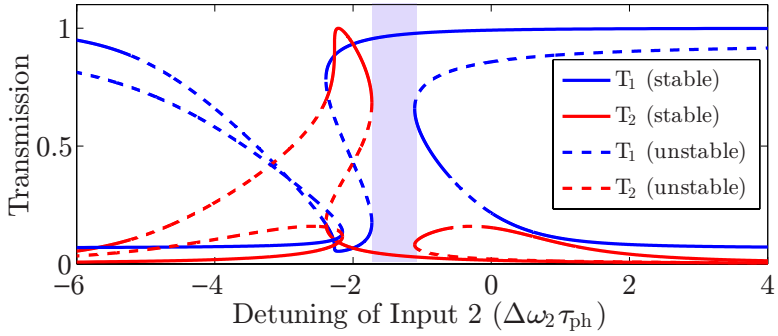

Figure 7.3: Stable and unstable transmission states as a function of input field 2's detuning when the detuning of input field 1 and both of their power levels are kept constant at the bias point. The purple shaded region indicates where switching will occur in the presence of a phase modulation.

region could flip the device. Figure 7.3 indicates that for detunings of input beam 2 larger than ~-1.1 (to the right of the shaded region in the figure) the states exhibit a slightly more complicated behavior. However, it seems that the transmission of beam 2 will inevitably drop even for detunings larger than this value, and the device may be expected to flip in this case as well.

7.3.1 Design principles

Modulations of the input-beam detunings are directly related to modulations in their phases. The phase-switching process is modeled by solving Eqs. (7.4) and (7.5) for the dynamics of the field when the input beams are given by

$$A_{in}^{(k)}(t) = \sqrt{P_0}e^{i\phi_k(t)-i\omega_0 t}. \tag{7.19}$$

Here the time-dependent phase $\phi_k(t)$ is imposed by a set or reset signal. Its influence is to temporarily modulate the detuning of the input beam,

$$\Delta\omega_k(t) = \Delta\omega_0 - \frac{d\phi_k}{dt}. \tag{7.20}$$

Thus, the negative of the derivate of the phase profile is equivalent to a shift in detuning. A negative slope in the phase profile thus increases the detuning and moves the system into a desired switching region according to the previous considerations. Practically, however, it is desirable that the phase modulation signal be able to be turned

off. Thus a negative slope in the phase cannot be realized without an accompanying positive slope. The most convenient means for implementing the phase modulation is in pulsed form. Therefore, we will consider Gaussian phase modulations of the form

$$\phi_k(t) = \phi_0 e^{-(t-t_p)^2/T_0^2}. \tag{7.21}$$

The leading edge of this phase modulation induces a negative detuning on the beam that is not useful for either the set or reset operations. The trailing edge, however, is exactly what is needed to switch the device. The maximum detuning in the trailing edge of the phase modulation is approximately given by

$$\Delta\omega_k^{max} \approx \Delta\omega_0 + 0.86\phi_0/T_0. \tag{7.22}$$

If the detuning is sufficiently large and maintained for a sufficiently long duration of time that the resonator can respond, the device can be expected to set or reset as the case may be.

The phase modulation profile

These considerations lead to some useful design principles for the phase modulation profile. The first comes from the requirement that the change in detuning must be large enough to drive the system into an appropriate switching region. Roughly speaking, it is desirable that the maximum shift in detuning be approximately a cavity linewidth ($1/\tau_{ph}$). This intuitive understanding is confirmed by considering Eq. (7.22) for the maximum detuning and the values defining the switching region shown in Fig. 7.3. Thus, it is approximately the case that the device will switch for phase modulation parameters satisfying

$$\frac{\phi_0}{T_0} \gtrsim \frac{1}{\tau_{ph}}. \tag{7.23}$$

Additionally it is necessary that the system have enough time to respond to the phase modulation in order for it to switch. This consideration leads to a second approximate condition for the modulation's temporal duration,

$$T_0 \gtrsim \tau_{ph}. \tag{7.24}$$

The intuitive criteria for the phase-modulation parameters expressed in Eqs. (7.23) and (7.24) are verified by numerical solutions of Eqs. (7.4) and (7.5). The input beam amplitudes $A_{in}^{(k)}$ are modeled by Eq. (7.19) with phase profiles of the form (7.21). The results are shown in Figs. 7.4 and 7.5. Figure 7.4 shows a set of simulation results for modulations with different values of maximum phase shift ϕ_0 but having the same temporal duration $T_0 = 2\tau_{ph}$. The difference between Figs. 7.4(a) and 7.4(b) is that the ratio ϕ_0/T_0 is increased from $1/\tau_{ph}$ in 7.4(a) to $1.15/\tau_{ph}$ in 7.4(b). As a result, a switching threshold is crossed and the set and reset operations that fail in the former case succeed in the latter. Note that this threshold is approximated well by Eq. (7.23). Figures 7.4(c) and 7.4(d) show that switching continues to succeed for ϕ_0 values of π and 2π, respectively. Further simulation results not presented here show that the phase modulation continues to succeed up to $\phi_0 \sim 9$. This corresponds to a ratio ϕ_0/T_0 of $4.5/\tau_{ph}$, indicating that switching occurs reliably for values of the temporary detuning significantly to the right of the shaded region in Fig. 7.3.

Figure 7.5 shows a set of simulation results for different values of the temporal duration T_0 but the same maximum phase shift $\phi_0 = \pi$. The difference between Figs. 7.5(a) and 7.5(b) is that T_0 is increased from $\tau_{ph}/2$ to τ_{ph}. As a result, the set and reset operations that fail in the former case succeed in the latter. Note that this switching threshold is predicted well by Eq. (7.24) and results from the fact that the system needs enough time to respond to the phase modulation in order to switch. Figures 7.5(c) and 7.5(d) indicate that there exists a second switching threshold for T_0 somewhere between $4\tau_{ph}$ and $5\tau_{ph}$. Note that these values of T_0 correspond to ratios ϕ_0/T_0 of $0.76/\tau_{ph}$ and $0.63/\tau_{ph}$. Thus, the location of this second switching threshold is in relatively good approximation with the prediction of Eq. (7.23).

A figure of merit for suitable materials

The results in Figs. 7.4 and 7.5 demonstrate that phase switching can work in principle. What they do not show is that two-input Kerr bistability, much less phase switching, are feasible in practice. In practice material absorption heats up the cavity and changes its refractive index via the thermo-optic effect. It was stated in the introduction of this chapter that the two-input configuration can overcome this limitation. Here that claim will be examined in more detail. A thermal model of the

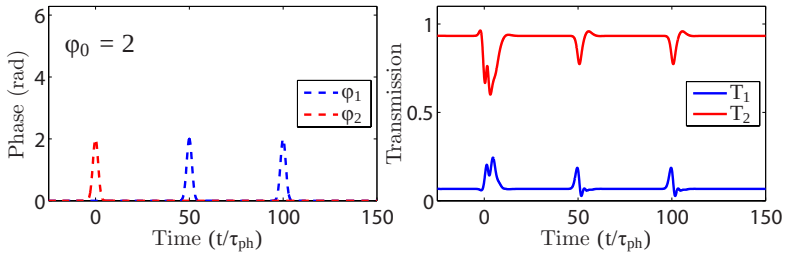

(a)

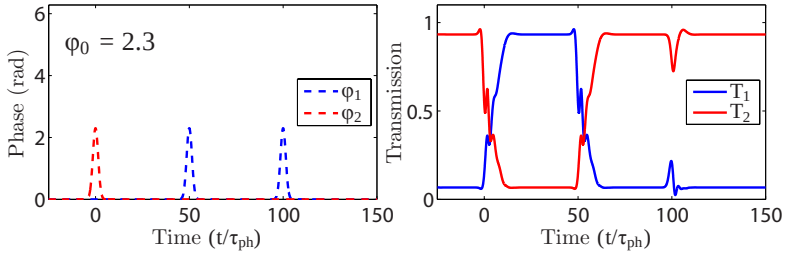

(b)

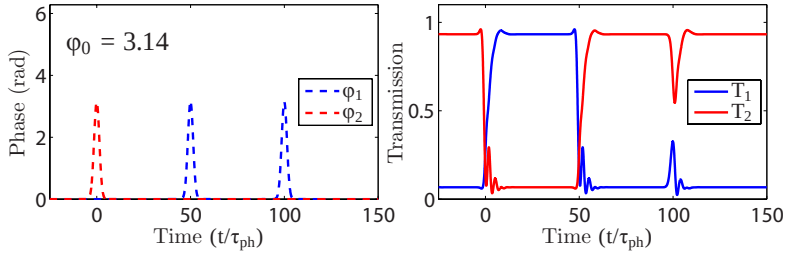

(c)

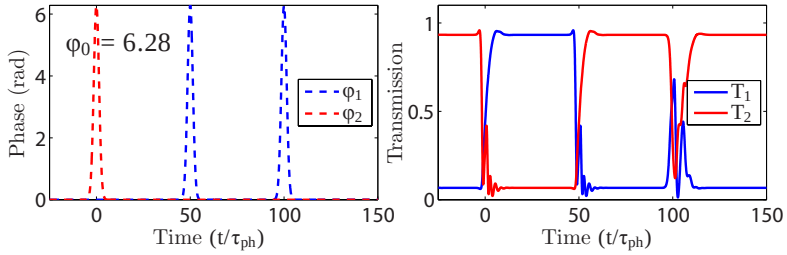

(d)

Figure 7.4: Flip-flop operation by pure phase modulation of the input fields when the temporal duration of the modulation $T_0 = 2\tau_{ph}$ and the maximum phase shift is (a) $\phi_0 = 2$, (b) $\phi_0 = 2.3$, (c) $\phi_0 = \pi$, and (d) $\phi_0 = 2\pi$. The power levels of the two inputs are the same and do not change in time.

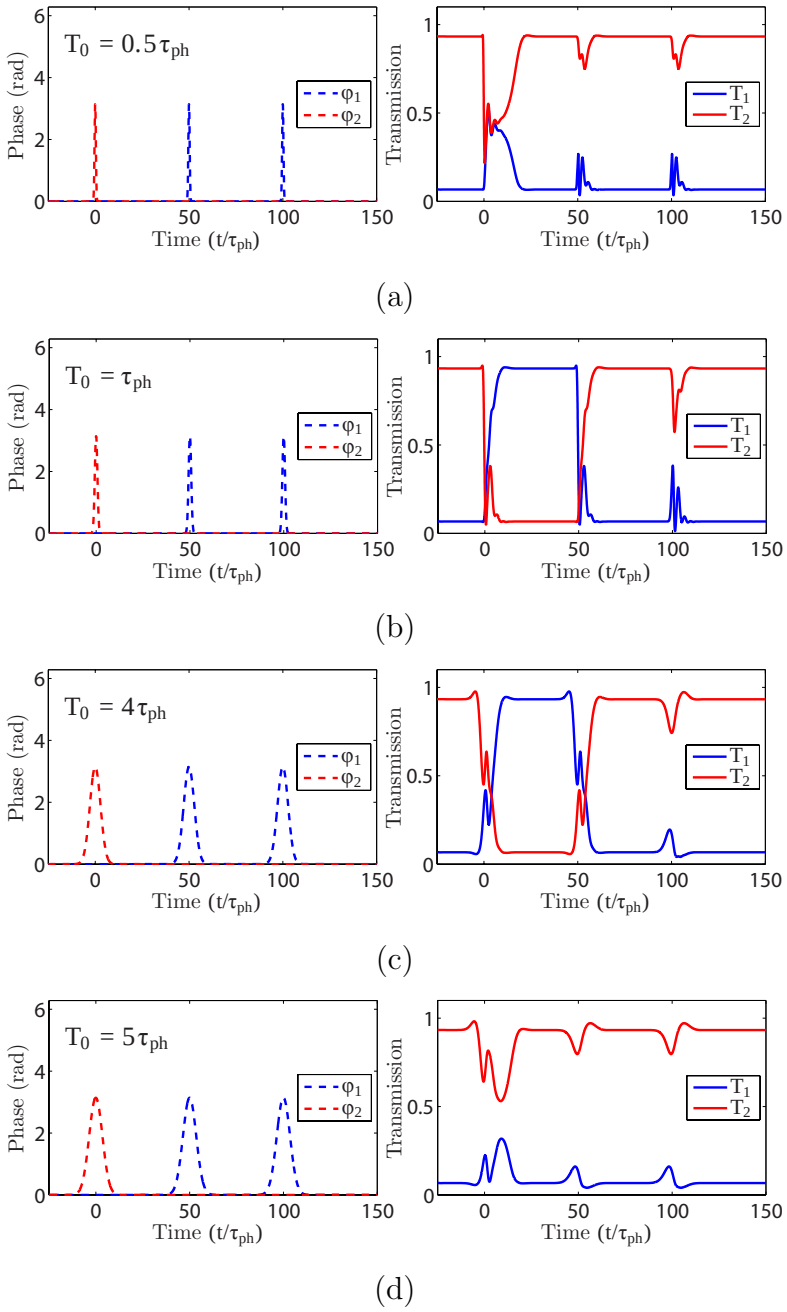

Figure 7.5: Flip-flop operation by pure phase modulation of the input fields when the maximum phase shift $\phi_0 = \pi$ and the temporal duration of the modulation is (a) $T_0 = \tau_{ph}/2$, (b) $T_0 = \tau_{ph}$, (c) $T_0 = 4\tau_{ph}$, and (d) $T_0 = 5\tau_{ph}$. The power levels of the two inputs are the same and do not change in time.

resonator will be developed and used to formulate a figure of merit for the suitability of material systems out of which to construct it.

The intrinsic photon lifetime of the cavity [related to the overall photon lifetime by Eq. (5.20)] has two distinct contributions. One contribution is from material absorption and another is from scattering and radiation losses. In other words,

$$\frac{1}{\tau_{ph}^{i}} = \frac{1}{\tau_{ph}^{ab}} + \frac{1}{\tau_{ph}^{sc}}, \tag{7.25}$$

where τ_{ph}^{ab} accounts for absorption and τ_{ph}^{sc} accounts for scattering. Absorption can be analyzed as a perturbative contribution in the dynamic mode amplitude equation (7.1), leading to the relation

$$\frac{1}{\tau_{ph}^{ab}} \approx \frac{c\alpha^{(ab)}}{n_0}, \tag{7.26}$$

where $\alpha^{(ab)}$ is the absorption coefficient of the material out of which the cavity is made (absorptive inhomogeneity will be neglected for simplicity). By assuming that 100% of the absorbed energy goes towards heating up the device, a rate equation is formulated for the thermal energy stored in the cavity ΔU_T,

$$\frac{d\Delta U_T}{dt} = \frac{c\alpha^{(ab)}}{n_0}\left(|a_1|^2 + |a_2|^2\right) - \frac{\Delta U_T}{\tau_T}, \tag{7.27}$$

where τ_T is a thermal lifetime that is typically on the order of microseconds. The thermal energy is related to the thermally-induced change in refractive index Δn_T by

$$\Delta n_T = \frac{(\partial n/\partial T)\Delta U_T}{\rho C_\rho V_{cav}}, \tag{7.28}$$

where $\partial n/\partial T$ is the thermo-optic coefficient of the medium, ρ is its density, C_ρ is its specific heat capacity, and V_{cav} is the volume of the cavity. By combining Eq. (7.28) with Eq. (7.27) a rate equation is found for the index change,

$$\frac{d\Delta n_T}{dt} = \frac{(\partial n/\partial T)c\alpha^{(ab)}}{n_0\rho C_\rho V_{cav}}\left(|a_1|^2 + |a_2|^2\right) - \frac{\Delta n_T}{\tau_T}. \tag{7.29}$$

In order to describe the influence of the index change on the mode amplitudes the theory of chapter 6 is used to add an additional term to Eqs. (7.4) and (7.5),

$$\frac{da_k}{dt} = -i\omega_k a_k - \frac{1}{2\tau_{ph}}a_k + \kappa A_{in}^{(k)}(t) + i\gamma(|a_k|^2 + 2|a_{3-k}|^2)a_k + i\omega_k\frac{\Delta n_T}{n_0}a_k, \tag{7.30}$$

where $k = 1$ or 2 and it has been assumed that all of the γ parameters are approximately the same. Here the additional term $i\omega_k \frac{\Delta n_T}{n_0} a_k$ is taken directly from Eq. (6.5) by assuming a spatially uniform index change and making the rotating-wave approximation if necessary. Note that this term simply results in a shift of the resonance frequency by an amount $-\omega_k \Delta n_T / n_0$ as expected. Equations (7.29) and (7.30) can be used to evaluate the relative magnitudes of the Kerr and thermal nonlinearities. By finding the steady-state solution for Δn_T in Eq. (7.29) and using it in (7.30) the resonance frequency shift from the thermal effect is evaluated as

$$\Delta\omega_{Thrm} \approx -\frac{\omega_k \tau_T c \alpha^{(ab)} (\partial n/\partial T)}{n_0^2 \rho C_\rho V_{cav}} E_k, \tag{7.31}$$

where E_k is the energy stored in the cavity (it is assumed that one mode dominates the cavity energy at a given time). The resonance frequency shift from the Kerr effect in a stable state of the system can also be evaluated from Eq. (7.30) as

$$\Delta\omega_{Kerr} \approx -\frac{\omega_k c n_2}{n_0^2 V_{cav}} E_k, \tag{7.32}$$

where the following approximate form of γ has been used:

$$\gamma \approx \frac{\omega_k c n_2}{n_0^2 V_{cav}}. \tag{7.33}$$

The ratio of the thermally-induced resonance shift to the Kerr-induced resonance shift is then found to be

$$\Upsilon_T = \left| \frac{\Delta\omega_{Thrm}}{\Delta\omega_{Kerr}} \right| = \frac{\tau_T \alpha^{(ab)} (\partial n/\partial T)}{\rho C_\rho n_2}. \tag{7.34}$$

The parameter Υ_T depends only on properties of the material and is independent of the design of the resonator (although this is not strictly true since τ_T has some dependence on the cavity structure). Values of Υ_T that are acceptable will depend on the application, but it is clearly desirable that it be as small as possible. Realistically, if the two-input device is ever used some active cooling mechanism will probably be needed for temperature stability, and this will reduce the effective value of Υ_T by reducing the effective value of τ_T.

Cavity design

If a suitable material is found, an appropriate cavity design will also be needed to make the device feasible. The two crucial parameters to choose here are the cavity's

quality (Q) factor and volume. It will be assumed that the cavity is overcoupled, meaning that the intrinsic cavity losses are negligible compared to coupling losses. This will be desirable in practice. It will also be assumed that the cavity is of the Fabry–Perot type so that $|\kappa|^2 = 1/2\tau_{ph}$ from Eq. (6.24).

First, we'll estimate the optical power of the input beams that will be needed for a given material system and cavity design. In order to bias the device at the point $4\gamma|\kappa|^2\tau_{ph}^3 P_0 = 2$ that we have been considering, the required power would be $P_0 \approx 1/\gamma\tau_{ph}^2$. Using the expression for γ in Eq. (7.33) and the relation $Q = \omega_k\tau_{ph}$ this estimate can be reduced to

$$P_0 \approx \left(\frac{V_{cav}}{Q^2}\right)\frac{\omega_k n_0^2}{c n_2}. \tag{7.35}$$

The necessary power is proportional to the cavity volume and inversely proportional to the square of the quality factor. This dependence on the volume makes sense since a larger volume will result in a lower intra-cavity intensity for the same bias power. The dependence on the quality factor can be seen as having two distinct contributions. One is from the fact that a higher value of Q means a smaller spectral linewidth. Shifting the resonance by a fixed number of linewidths would then imply a smaller total frequency shift and less required power to obtain that shift. The second factor of Q comes from the cavity-enhancement in intensity. The higher the Q, the higher the intracavity energy for a given bias power and hence the less bias power required.

A second important parameter for device operation is the temperature shift caused in the cavity by material absorption. If this is too high the device can be damaged. This can be evaluated by the relation $\Delta T = \Delta n_T/(\partial n/\partial T)$ and the steady-state solution for Eq. (7.29),

$$\Delta T \approx \left(\frac{1}{Q}\right)\frac{2\tau_T\alpha^{(ab)}n_0}{n_2\rho C_\rho}, \tag{7.36}$$

where the intracavity energy has been approximated as $E = 2/\gamma\tau_{ph}$ in accordance with the biasing conditions under consideration. The temperature estimate in Eq. (7.36) shows that it depends inversely on the Q factor. Because low temperature shifts and low bias powers are desirable it might be concluded from Eqs. (7.35) and (7.36) that a high Q factor must be desirable, but this is not always the case. A higher Q factor would also imply a slower switching speed. The simulations of Figs. (7.4) and (7.5)

show that typical switching times (T_{sw}) are given approximately by

$$T_{sw} = 5\tau_{ph}, \tag{7.37}$$

and hence the switching time is linearly proportional to Q. Thus, a trade-off exists between power and operating temperature on the one hand, and speed on the other.

7.3.2 An example

In order to flesh out these design principles a specific example will now be considered. It should be noted that this example is inherently speculative. It is not meant to be a definitive claim that the device considered could easily be made nor that it is the best design that could be conceived. The purposes of this example are to demonstrate the feasibility of the device using realistic material parameters and an appropriate cavity design, and to compare and contrast the performance of the single-input mode of operation with the two-input phase-switched mode of operation proposed in this chapter. Not all of the parameters used in the simulations are known with certainty, as will be discussed, but they are reasonably derived from the literature.

The cavity medium that will be considered is silicon nitride, which has been investigated by a number of groups in recent years for photonics applications [26–28, 142,153,154]. It is chosen for this example because it exhibits an intensity-dependent refractive index ~10 times higher than silica glass and does not exhibit the strong two-photon absorption and resulting free-carrier absorption nonlinearities that silicon does [142]. The cavity structure that will be considered is depicted in Fig. 7.6. This structure was not chosen arbitrarily. The ring resonators that are commonly investigated for Si_3N_4 do not appear to be technologically feasible for this device because they either have large volumes or else radiation losses from small bend radii limit their achievable Q [153]. Additionally, by using stop-band Bragg gratings in the structure of Fig. 7.6 spectrally selective feedback could be used to prevent the onset of parametric oscillation, a phenomenon that has been observed in silicon nitride ring resonators [28] and would prevent the device from working. The author is not aware of any experimental effort to fabricate a resonator such as depicted in Fig. 7.6 in silicon nitride and is also unaware of what challenges would be faced in doing so.

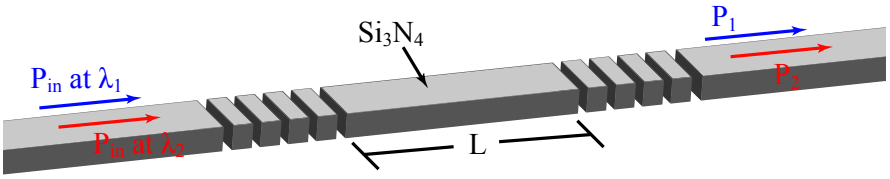

Figure 7.6: A silicon nitride two-input flip-flop. Two input fields with the same power P_{in} are coupled to spectrally distinct cavity modes with resonance wavelengths λ_1 and λ_2.

They will inevitably exist for achieving the value of $Q = 240,000$ that is considered in this example.

The parameters used in the calculations are listed in table 7.1, with references to where they are taken from. Before proceeding a couple of the more speculative parameters should be discussed. Chief among them is the material absorption coefficient, $\alpha^{(ab)}$. In Ref. [153] experimental measurements of propagation losses in Si_3N_4

Table 7.1: Parameter values used for simulations of the cavity described in Fig. 7.6.

quality factor (Q)	240,000
propagation loss[1] (α)	3 dB/m
absorption loss[1] ($\alpha^{(ab)}$)	0.3 dB/m
cavity length (L)	60 μm
cavity volume (V_{cav})	16.8 μm^3
intensity-dependent index[2] (n_2)	2.4×10^{-19} m^2/W
thermo-optic coefficient[2] ($\partial n/\partial T$)	4×10^{-5} K^{-1}
specific heat capacity[3] (C_ρ)	0.71 J/gK
density[4] (ρ)	3.17 g/cm^3
thermal lifetime[2] (τ_T)	5 μs
refractive index[5] (n_0)	2
grating reflectivity	99.8%
figure of merit (Υ_T)	25.5

Values are taken or reasonably inferred from Refs. [1] [153], [2] [142], [3] [155], [4] [156], and [5] [33]

waveguides made using a specific fabrication technique were studied and found to be quite low. It was observed that waveguide losses exhibited a strong dependence on their bending radius, and this dependence agreed well with a numerical model. The assumption of the model was that material absorption was negligible in comparison to radiation and scattering, and the authors concluded from its accuracy that this assumption was valid. Based on that conclusion a value of $\alpha^{(ab)} = 0.3$ dB/m that is one order of magnitude smaller than the lowest propagation losses acheived in Ref. [153] is used as a reasonable estimate for the example of this section. The total attenuation coefficient for the waveguide is chosen to be the smallest value that they measured, $\alpha = 3$ dB/m. It should also be noted that some of the parameters, such as $\partial n/\partial T$, were measured in silicon-rich silicon-nitride (SiN) devices and it is assumed here that they are good estimates for Si_3N_4.

One-input intensity-switched operation

The device is modeled by solving Eqs. (7.30) for the mode amplitudes along with the rate Eq. (7.29) for the thermal index change. In the case of a single input beam a_2 can be set to zero so that (7.30) reduces to a single equation for a_1. Figure 7.7 shows flip-flop operation by intensity modulation in the one-input case. Figure 7.7(a) shows that the required input power is quite low (~1.2 mW) since the thermal nonlinearity is strong. The reset operation is applied by reducing the power of the input beam to about 0.3 mW at $t = 50$ μs. The output power immediately drops after this, but the transmission of the resonator does not change immediately. The transmission takes 10 μs or so to transition to the low state. The reason for this is evident from Fig. 7.7(c), which shows the temperature shift of the cavity transitioning on a similar time scale. A similar set operation is applied at $t = 125$ μs by increasing the input power to 2.8 mW. The set operation also occurs on a time scale of roughly 10 μs as can be seen from Figs. 7.7(b) and 7.7(c).

Two-input phase-switched operation

Figure 7.8 shows flip-flop operation by pure phase modulation in the two-input case. The set and reset signals are phase modulations of input beams 2 and 1, respectively,

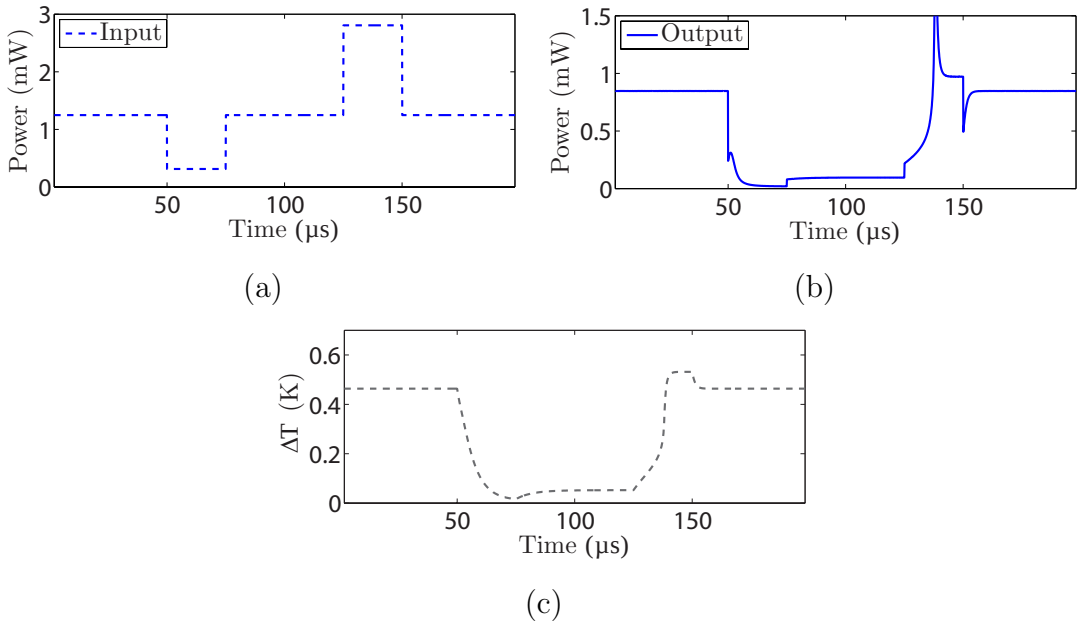

Figure 7.7: Simulated operation of the silicon nitride cavity of Fig. 7.6 as a one-input intensity-switched flip-flop based on thermal nonlinearity. (a) The power of the input field; (b) the power of the output field; (c) the temperature shift of the cavity from optical absorption.

and occur at t = 10 and 20 μs as shown in Fig. 7.8(a). The phase modulations are Gaussian in form and given by Eq. (7.21) with T_0 = 400 ps and $\phi_0 = \pi$. When the set signal arrives at t = 10 μs the device flips from the state where the transmission of beam 1 is low to the state where it is high as shown in Fig. 7.8(b). The inset of Fig. 7.8(b) shows that switching occurs over a time period of ~ 1 ns, which is several orders of magnitude faster than the one-input device.

The input bias power P_{in} is also plotted in Fig. 7.8(b) and is ≈ 19 mW. Note that this is much higher than the required bias power for the one-input device of Fig. 7.7 because the nonlinear mechanism in the two-input case is the Kerr effect, which is much weaker than the thermal one. The temperature shift of the resonator caused by the presence of the powerful cavity-enhanced input beams is predicted by the model to be ~10 K as shown in Fig. 7.8(c). When the set and reset operations occur there is some slight perturbation to the cavity temperature, but it is quickly restored to its steady-state value without having any noticeable effect.

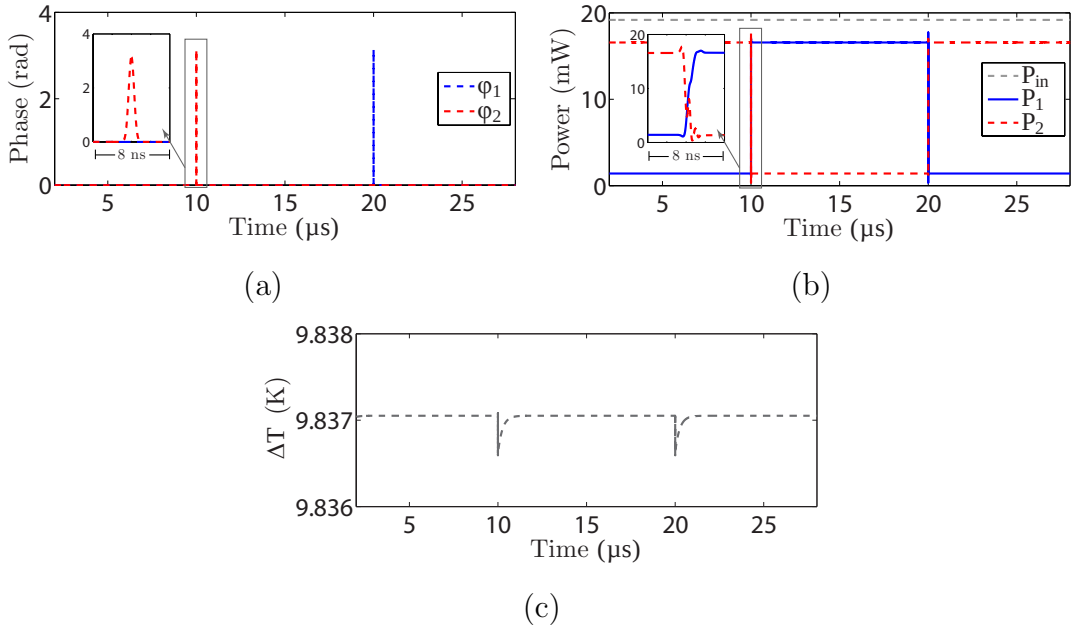

Figure 7.8: Simulated operation of the silicon nitride cavity of Fig. 7.6 as a two-input phase-switched flip-flop based on the Kerr effect. (a) The phases of the two input fields; (b) the transmitted powers of the two inputs, as well as the power of either input that is kept constant at ~ 19 mW; (c) the temperature shift of the cavity from optical absorption.

7.4 Summary

In this chapter the use of two input fields to bistable Kerr resonators was proposed as a possible means of overcoming thermal limitations to their use as optical memory elements (flip-flops). The theoretical methodology of chapter 5 was applied to formulate a general theoretical description of such devices and clarify their appropriate biasing regimes. Switching between the two stable states by pure phase modulations of the input fields was also proposed and numerically demonstrated as a robust alternative to switching by intensity modulation. A model of the thermal dynamics of the resonator was developed and used to derive criteria for evaluating appropriate materials and cavity designs. An example simulation using feasible material and cavity parameters was used to compare the performance of one-input intensity-switched operation of the device to the two-input phase-switched operation proposed in this chapter.

8 Conclusions

In this thesis a set of theoretical methods was developed for describing nonlinear optical phenomena in photonic devices. In particular, the methods developed are applicable to devices of any size scale and with any degree of refractive-index contrast. They were then applied to understand a selection of nonlinear phenomena. Chapter 1 framed this work in terms of the past, placing it in its historical context. The aim of the present chapter is to frame it in terms of the future. The central question here is 'where is this work going?' Section 8.1 attempts to answer this question regarding chapters 2-4 and is concerned with waveguide devices. Section 8.2 attempts to answer this question regarding chapters 5-7 and is concerned with resonator devices.

8.1 Nonlinear photonic waveguides

Modeling techniques

In chapter 2 a set of theoretical methods was developed for describing nonlinear optical phenomena in guided-wave structures. The goal of this chapter was generality. Methods were developed for describing a variety of material systems that are applicable to devices of any size scale and any material index contrast. Thus, the vast majority of nonlinear guided-wave phenomena can be described both qualitatively and quantitatively using the approaches presented there.

There remain, however, some important phenomena that violate an assumption made in chapter 2. As a result, future work is needed to clarify how this assumption

can be avoided in a way that is both simple enough to yield insight and that is also quantitatively accurate. The assumption is that the electric and magnetic field mode profiles **e** and **h** are independent of frequency over the optical bandwidth. In the case of slow-light propagation in photonic crystals this assumption breaks down because the mode profiles become highly dispersive even for narrowband fields [47]. Exploring the implications of this mode dispersion would be not only an interesting venture but a relevant one. Studies of nonlinear optical phenomena in slow-light photonic crystals are being widely pursued as a result of the enhancement in optical nonlinearity, and hence the lower power requirements, that they provide [46, 47, 157–160]. In the case of supercontinuum generation this assumption often breaks down even for waveguides that exhibit minimal mode dispersion as a result of the extremely broad bandwidth generated in the field. Studies of supercontinuum generation have naturally been extended to waveguides with subwavelength dimensions in recent years, owing to their enhanced nonlinearity [161, 162]. As this trend continues the implications of mode-profile dispersion will become more relevant since it is a stronger effect in this size regime (see chapter 3). What these implications are is not well known, and future studies that clarify them would be relevant.

The analysis of chapter 2 also suggests that the operator-equation approach to guided-wave optics developed in Refs. [59,60] has been under-utilized for many years in the research community. It is only recently that a few people have begun to seriously apply it [61–64]. Its application in this thesis to rigorously describe nonlinear effects supports the indication of their work: that the operator approach can be fruitful for understanding a wide variety of guided-wave phenomena. This is not surprising; the approach itself finds an underlying simplicity to a complicated system of differential equations. As a result it is the opinion of the author that future work in the field of guided-wave optics could greatly benefit from it.

Prospects for devices

In chapters 3 and 4 the theoretical method of chapter 2 was applied to studying nonlinear effects in silicon waveguides. Chapter 3 presented a detailed study of the influence of subwavelength waveguide dimensions on the propagation parameters of the optical field. The insights drawn in this chapter will be important for anyone

attempting to using such size scales for maximizing waveguide nonlinearity, which is often done [163]. The implications here are primarily quantitative in nature, and it is not an anticipation of the author that they will lead to fundamentally new devices. Rather, they will be useful for optimizing existing ones.

Chapter 4 presented an experimental and theoretical study of some nonlinear polarization effects that can occur in silicon waveguides. The results are beautiful and interesting, but not important from a technological point of view. This is largely because, in the author's opinion, the implication of the large body of research conducted on nonlinear silicon photonics is that silicon is not a very useful nonlinear material in the 1.55-μm wavelength region. Because of nonlinear absorption mechanisms, many of the proposed devices are not very practical.

Integrated nonlinear photonic devices in other materials do, however, hold promise. It has long been a dream that all-optical signal processing based on nonlinear effects could eliminate the need for conversion of telecommunication signals between the optical and electrical domains. Many device ideas for signal processing have been developed using optical fiber [10]. For the most part these devices haven't become practical as a result of their high power requirements and expensive manufacturing costs. If such devices could be monolithically integrated on a single chip using submicron, highly nonlinear waveguides both of these problems could be overcome. Thus, it is conceivable that integrated nonlinear photonic devices could have a significant societal impact in the long term. In this context the fundamental study of chapter 4 may inspire new ideas in a growing and important field (assuming, of course, that it is ever read).

8.2 Nonlinear photonic resonators

Modeling techniques

In chapter 5 a set of theoretical methods was developed for describing nonlinear optical phenomena in resonators. The goal of this chapter was generality. Methods were developed for describing a variety of material systems that are applicable to devices of any size scale and material index contrast. By establishing the theory

rigorously from Maxwell's equations for a wide variety of resonators, this chapter can be seen as crowning the work of Haus [125] and of Oskar Painter's group [53–55]. Haus established the same equations on purely heuristic grounds, including the perturbative term, using only energy-conservation considerations (with truly formidable intuition) [125]. In Refs. [53–55] they were derived from Maxwell's equations using mode-orthogonality conditions that apply only to specific types of resonators. Thus, chapter 5 can be seen as an extension of their work, rigorously demonstrating the validity of these equations to a much wider range of resonator types.

There remain, however, some important devices that violate an assumption made in chapter 5. The two primary assumptions made were 1) that the unperturbed cavity exhibits neither material absorption nor gain, and that 2) the unperturbed cavity's finesse $\gg 1$. Semiconductor lasers and semiconductor optical amplifiers do not violate assumption 1 but many of them violate assumption 2. The reason assumption 1 is not violated is that the material gain and/or loss created by current-injected free carriers can always be included as a perturbation to the cavity. Assumption 2, however, is violated by many semiconductor laser and amplifier devices. These cavities are often designed to dump energy very quickly in order to optimize output power, and hence often have a low finesse. Thus the theory of chapter 5 does not obviously apply to them. It is conceivable, however, that it can be extended to incorporate them in a rigorous way. In the case of semiconductor lasers, for instance, it is still the case that the electromagnetic field solution is dominated by modes at discrete resonance frequencies, which is the implication of assumption 2) and at the heart of the methodology. Extending this methodology to incorporate these devices is therefore a problem of making the right assumptions in the right order. It would be a useful endeavor since they are extremely important from a technological point of view, and modeling them is currently dominated by purely phenomenological methods (e.g. rate-equation approaches).

Prospects for devices

In chapter 6 a wavelength conversion device was proposed based on dynamically changing the refractive index of a resonator. The device would be relevant to current communication networks if it could be realized suitably in practice, especially because

of its potential for reconfigurability. It should be realized that if photonic-crystal waveguide technology improves, then the 'slow-light waveguide way' of implementing the same device has the potential for superior performance. Specifically, such waveguides would need low propagation losses in spectral regions exhibiting large group indices. In the author's opinion the resonator implementation of the device proposed in chapter 6 is closer to being achievable given the current state of fabrication technology. There are some practical issues that need to be addressed before this could be done. A specific technique for changing the refractive index on the short time scales needed for decent performance needs to be found, as well as the appropriate material system for implementing that technique. Timing issues and device energy consumption will also need to be addressed, but similar issues are regularly addressed in the industry and it is likely that they will not prove insurmountable. Understanding the specific applications within communication networks for which such a device would find commercial interest will guide all of these considerations.

In chapter 7 a phase-switched optical memory device was proposed based on the Kerr effect in a resonator. The device uses two input fields in order to overcome thermal limitations to the switching speed that are normally observed in bistable microresonator devices. It is conceivable that the device could be developed for commercial application in the long term. The next step in development would be an experimental demonstration of two-input bistability in general and phase-switching in particular. The thermal analysis of chapter 7 provides the guidelines that should be followed in any such experimental effort. It remains an open question of what precisely are the applications of the device that would find commercial interest. The answer to this question would guide any development effort down the road.

8.3 Final thoughts

The aim of this thesis was to develop methods for solving Maxwell's equations that are applicable to a wide range of phenomena in nonlinear photonics. In the opinion of the author chapters 2 and 5 have found this mark. The applications of these methods to various problems in chapters 3, 4, 6, and 7 demonstrate their ability to simultaneously make quantitative predictions about the real world and to yield insight. I believe they

are keys that can open vast warehouses of understanding, and the work of this thesis has solidified that belief in my mind.

A Proof that $\hat{A}$ and $\hat{B}$ are Hermitian

Both $\hat{A}$ and $\hat{B}$ are operators of the form

$$\hat{O} = \begin{pmatrix} \hat{O}_{11} & \hat{O}_{12} \\ \hat{O}_{21} & \hat{O}_{22} \end{pmatrix}, \tag{A.1}$$

where the elements $\hat{O}_{kl}$ are not operators on the set of vectors described by Eq. (2.12), but on the set of two-dimensional complex vector functions $\mathbf{f}_T(x, y)$. A sufficient condition for the operator $\hat{O}$ to be Hermitian is that

$$\left[\iint \mathbf{f}_T^{a\star} \cdot \hat{O}_{kl}\, \mathbf{f}_T^b \, dxdy \right]^* = \iint \mathbf{f}_T^{b\star} \cdot \hat{O}_{lk}\, \mathbf{f}_T^a \, dxdy, \tag{A.2}$$

for all integrable $\mathbf{f}_T^a$ and $\mathbf{f}_T^b$. In other words, it is sufficient that the diagonal elements $\hat{O}_{11}$ and $\hat{O}_{22}$ themselves be Hermitian and that $\hat{O}_{12}$ and $\hat{O}_{21}$ be a Hermitian conjugate pair.

Consider the operator $\hat{B}$ in Eq. (2.13). Since its diagonal elements are zero, it is sufficient to demonstrate that its off diagonal elements ($\hat{B}_{12} = -\hat{\mathbf{z}}\times$ and $\hat{B}_{21} = \hat{\mathbf{z}}\times$) form a Hermitian conjugate pair in the sense of Eq. (A.2).

$$\begin{aligned} \left[\iint \mathbf{f}_T^{a\star} \cdot \hat{B}_{12}\, \mathbf{f}_T^b \, dxdy \right]^* &= \left[\iint \mathbf{f}_T^{a\star} \cdot \left(-\hat{\mathbf{z}} \times \mathbf{f}_T^b \right) dxdy \right]^* \\ &= \left[\iint -\mathbf{f}_T^b \cdot \left(\mathbf{f}_T^{a\star} \times \hat{\mathbf{z}} \right) dxdy \right]^* \\ &= \iint \mathbf{f}_T^{b\star} \cdot \left(\hat{\mathbf{z}} \times \mathbf{f}_T^a \right) dxdy \\ &= \iint \mathbf{f}_T^{b\star} \cdot \hat{B}_{21} \mathbf{f}_T^a \, dxdy, \end{aligned}$$

establishing the Hermiticity of $\hat{B}$. Establishing the Hermiticity of $\hat{A}$ follows a similar line of reasoning, but the details will be different depending on what kinds of materials are being considered.

A.1 Isotropic media

In the case of isotropic dielectric media $\hat{A}$ is given in Eq. (2.13) and has no off-diagonal components. Thus it is sufficient to demonstrate that $\hat{A}_{11}$ and $\hat{A}_{22}$ are individually Hermitian. Consider $\hat{A}_{11}$,

$$\begin{aligned}
\left[\iint \mathbf{f}_T^{a*} \cdot \hat{A}_{11}\, \mathbf{f}_T^b \, dxdy\right]^* &= \left[\iint \mathbf{f}_T^{a*} \cdot \left(\frac{\omega\epsilon}{c} - \frac{c}{\omega}\nabla_T \times \nabla_T \times\right) \mathbf{f}_T^b \, dxdy\right]^* \\
&= \iint \mathbf{f}_T^{b*} \cdot \left(\frac{\omega\epsilon}{c}\mathbf{f}_T^a\right) dxdy - \iint \mathbf{f}_T^a \cdot \frac{c}{\omega}\nabla_T \times \nabla_T \times \mathbf{f}_T^{b*}\, dxdy \\
&= \iint \mathbf{f}_T^{b*} \cdot \left(\frac{\omega\epsilon}{c}\mathbf{f}_T^a\right) dxdy - \iint \frac{c}{\omega}\nabla_T \times \mathbf{f}_T^a \cdot \nabla_T \times \mathbf{f}_T^{b*}\, dxdy \\
&= \iint \mathbf{f}_T^{b*} \cdot \left(\frac{\omega\epsilon}{c}\mathbf{f}_T^a\right) dxdy - \iint \frac{c}{\omega}\mathbf{f}_T^{b*} \cdot \nabla_T \times \nabla_T \times \mathbf{f}_T^a \, dxdy \\
&= \iint \mathbf{f}_T^{b*} \cdot \left(\frac{\omega\epsilon}{c} - \frac{c}{\omega}\nabla_T \times \nabla_T \times\right) \mathbf{f}_T^a \, dxdy \\
&= \iint \mathbf{f}_T^{b*} \cdot \hat{A}_{11}\, \mathbf{f}_T^a \, dxdy,
\end{aligned}$$

establishing the Hermiticity of $\hat{A}_{11}$. Here we've used the relation

$$\iint \mathbf{C}_T \cdot \nabla_T \times \mathbf{D}_L \, dxdy = \iint \mathbf{D}_L \cdot \nabla_T \times \mathbf{C}_T \, dxdy, \tag{A.3}$$

which holds for any integrable transverse vector field $\mathbf{C}_T$ and longitudinal vector field $\mathbf{D}_L$. Proof of the Hermiticity of $\hat{A}_{22}$ is very similar and establishes that $\hat{A}$ is Hermitian for isotropic dielectric media.

A.2 Anisotropic and/or magnetic media

Establishing the Hermiticity of $\hat{A}$ for the more general case of media that is anisotropic and/or magnetic [given by Eqs. (2.56)] is not as straightforward. First consider the

off-diagonal elements,

$$\begin{aligned}
\left[\iint \mathbf{f}_T^{a*}\cdot\hat{A}_{12}\,\mathbf{f}_T^{b}\,dxdy\right]^* &= \left[\iint \mathbf{f}_T^{a*}\cdot\left(\frac{i}{\epsilon_{33}}\begin{pmatrix}\epsilon_{13}\\ \epsilon_{23}\end{pmatrix}\hat{\mathbf{z}}\cdot\nabla_T\times\mathbf{f}_T^{b}\right)dxdy\right]^* \\
&+ \left[\iint \mathbf{f}_T^{a*}\cdot\left(i\nabla_T\times\hat{\mathbf{z}}\frac{1}{\mu_{33}}\begin{pmatrix}\mu_{31} & \mu_{32}\end{pmatrix}\mathbf{f}_T^{b}\right)dxdy\right]^* \\
&= \iint \mathbf{f}_T^{a}\cdot\left(\frac{-i}{\epsilon_{33}}\begin{pmatrix}\epsilon_{31}\\ \epsilon_{32}\end{pmatrix}\hat{\mathbf{z}}\cdot\nabla_T\times\mathbf{f}_T^{b*}\right)dxdy \\
&+ \iint \mathbf{f}_T^{a}\cdot\left(-i\nabla_T\times\hat{\mathbf{z}}\frac{1}{\mu_{33}}\begin{pmatrix}\mu_{13} & \mu_{23}\end{pmatrix}\mathbf{f}_T^{b*}\right)dxdy \\
&= \iint \left(\frac{-i}{\epsilon_{33}}\begin{pmatrix}\epsilon_{31} & \epsilon_{32}\end{pmatrix}\mathbf{f}_T^{a}\hat{\mathbf{z}}\right)\cdot\nabla_T\times\mathbf{f}_T^{b*}\,dxdy \\
&+ \iint -i\frac{1}{\mu_{33}}\begin{pmatrix}\mu_{13} & \mu_{23}\end{pmatrix}\mathbf{f}_T^{b*}\hat{\mathbf{z}}\cdot\nabla_T\times\mathbf{f}_T^{a}\,dxdy \\
&= \iint \mathbf{f}_T^{b*}\cdot\left(-i\nabla_T\times\hat{\mathbf{z}}\frac{1}{\epsilon_{33}}\begin{pmatrix}\epsilon_{31} & \epsilon_{32}\end{pmatrix}\mathbf{f}_T^{a}\right)dxdy \\
&+ \iint \mathbf{f}_T^{b*}\cdot\left(-i\frac{1}{\mu_{33}}\begin{pmatrix}\mu_{13}\\ \mu_{23}\end{pmatrix}\hat{\mathbf{z}}\cdot\nabla_T\times\mathbf{f}_T^{a}\right)dxdy \\
&= \iint \mathbf{f}_T^{b*}\cdot\hat{A}_{21}\,\mathbf{f}_T^{b}\,dxdy,
\end{aligned}$$

where we have again used relation (A.3) and the assumption that $\overleftrightarrow{\boldsymbol{\epsilon}}$ and $\overleftrightarrow{\boldsymbol{\mu}}$ are Hermitian matrices. Now consider the diagonal element $\hat{A}_{11}$. It will be convenient to define a 2×2 matrix $\overleftrightarrow{\boldsymbol{d}}$ as

$$\overleftrightarrow{\boldsymbol{d}} = \overleftrightarrow{\boldsymbol{\epsilon_T}} - \frac{1}{\epsilon_{33}}\begin{pmatrix}\epsilon_{13}\epsilon_{31} & \epsilon_{13}\epsilon_{32}\\ \epsilon_{23}\epsilon_{31} & \epsilon_{23}\epsilon_{32}\end{pmatrix}.$$

Note that $\overleftrightarrow{\boldsymbol{d}}$ is a Hermitian matrix so that $d^*_{ij} = d_{ji}$. Using this definition we have

$$\begin{aligned}
\left[\iint \mathbf{f}_T^{a*} \cdot \hat{A}_{11}\, \mathbf{f}_T^b \, dxdy\right]^* &= \left[\iint \mathbf{f}_T^{a*} \cdot \left(\frac{\omega}{c}\overleftrightarrow{\boldsymbol{d}} - \frac{c}{\omega}\nabla_T \times \frac{1}{\mu_{33}}\nabla_T \times\right) \mathbf{f}_T^b \, dxdy\right]^* \\
&= \iint \mathbf{f}_T^a \cdot \left(\frac{\omega}{c}\overleftrightarrow{\boldsymbol{d}}^* \mathbf{f}_T^{b*}\right) dxdy \\
&- \iint \frac{c}{\omega}\frac{1}{\mu_{33}}\nabla_T \times \mathbf{f}_T^a \cdot \nabla_T \times \mathbf{f}_T^{b*}\, dxdy \\
&= \iint \mathbf{f}_T^{b*} \cdot \left(\frac{\omega}{c}\overleftrightarrow{\boldsymbol{d}}\, \mathbf{f}_T^a\right) dxdy \\
&- \iint \frac{c}{\omega}\mathbf{f}_T^{b*} \cdot \nabla_T \times \frac{1}{\mu_{33}}\nabla_T \times \mathbf{f}_T^a \, dxdy \\
&= \iint \mathbf{f}_T^{b*} \cdot \left(\frac{\omega}{c}\overleftrightarrow{\boldsymbol{d}} - \frac{c}{\omega}\nabla_T \times \frac{1}{\mu_{33}}\nabla_T \times\right) \mathbf{f}_T^a \, dxdy \\
&= \iint \mathbf{f}_T^{b*} \cdot \hat{A}_{11}\, \mathbf{f}_T^a \, dxdy,
\end{aligned}$$

establishing that $\hat{A}_{11}$ is Hermitian. The proof that $\hat{A}_{22}$ is Hermitian is very similar and establishes that the operator $\hat{A}$ is also Hermitian for anisotropic and/or magnetic media.

B Construction of a mode-locked laser source

The purposes of this appendix are to chronicle the construction of the laser source used in the experiments of chapter 4 and to present a detailed description of its properties. Figure B.1 shows a schematic of the source, which is composed of three elements. The first element is the master oscillator, which is a mode-locked erbium-doped fiber laser. In order to temporally broaden the pulses from the laser, reduce their chirp and increase their peak power, they're passed through a 1.3 nm filter and subsequently amplified. Section B.1 presents a detailed description of the mode-locked laser, and section B.2 describes the influence of the filter and power amplifier on the pulse properties.

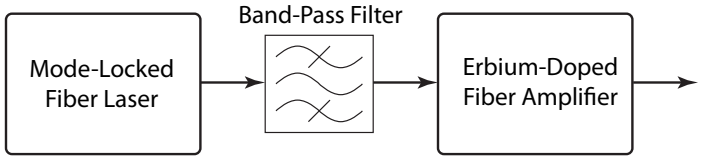

Figure B.1: Schematic of the source used in the experiments of chapter 4. Pulses from a mode-locked fiber laser are passed through a 1.3 nm bandpass filter and then amplified.

B.1 The laser

Figure B.2 shows a schematic of the mode-locked laser. At the heart of the cavity is a 5 m length of erbium-doped fiber. 980 nm pump light is coupled into the doped fiber

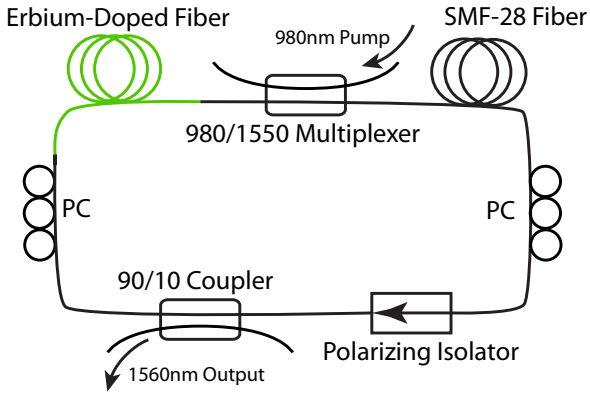

Figure B.2: Schematic of the mode-locked laser cavity.

and absorbed by the erbium ions, providing optical gain for the 1560 nm signal light propagating in the clockwise direction. The signal light is passed through a length of standard single-mode fiber (SMF-28) for dispersion compensation, two polarization controllers (PCs) at different locations in the cavity, a combination linear polarizer and optical isolator, and a directional coupler that removes 10 % of the signal for the output.

Nonlinear polarization rotation is the mode-locking mechanism. Nonlinear polarization rotation is the phenomenon of an optical pulse's polarization state rotating in an intensity-dependent manner as a result of the Kerr effect [29]. When the PCs are appropriately configured in the cavity the combined effect of nonlinear polarization rotation and the linear polarizer is similar to saturable absorption. As a result the laser can mode-lock, and the signal can oscillate in the cavity in the form of one or more short pulses.

Before dispersion management

Mode-locked fiber lasers are very sensitive to any dispersion-inducing elements in the cavity. The erbium-doped fiber typically exhibits normal dispersion that needs to be compensated. For this reason the standard single-mode fiber is used, which exhibits anomalous dispersion at the 1560 nm wavelength. In the initial arrangement ~10 m of single-mode fiber were used to attain mode locking. The signal output, measured using a 2 GHz photodiode and a 10 GHz oscilloscope, is shown in Fig. B.3. Pulses

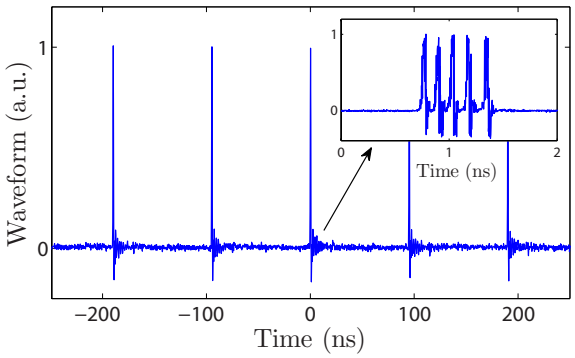

Figure B.3: The temporal waveform of the laser output before dispersion management, measured by a photodiode and standard oscilloscope. The inset shows a measurement of the same signal with an optical sampling oscilloscope, showing multiple pulses in each repetition period.

are seen to repeat about every 100 ns, which is the cavity's round-trip time. The temporal resolution of the photodiode-oscilloscope pair is limited to a response time of ~500 ps as a result of their finite bandwidth. As a result, while it appears from the oscilloscope that only one pulse exists in every repetition period, this appearence is deceptive.

The inset of Fig. B.3 shows a measurement of the same signal, except that an optical sampling oscilloscope was used instead of the photodiode and standard oscilloscope. The sampling oscilloscope can measure optical signals with a temporal resolution of ~20 ps. Clearly seen in the inset is that in each repetition period not one but five distinct pulses are present, being equally spaced by ~100 ps. This multipulsing behavior of the laser presented a problem because it meant that each pulse, after the external-cavity amplifier, had a peak power about five times lower than would be obtainable if the laser were operating in a single pulse-per-cycle regime.

After dispersion management

The multipulse phenomena was observed to be closely related to both the optical power and the amount of dispersion inside the cavity. The total number of pulses increased with increasing pump (and hence signal) power. Additionally, it exhibited a strong dependence on the amount of SMF-28 fiber used in the cavity. By cutting

the SMF-28 fiber down to ~6.6 m a stable single-pulse-per-cycle regime was attained. Moreover, mode-locking the laser into this single pulse regime was found to be relatively easy and repeatable. The output waveform is shown in Fig. B.4(a). The sampling-scope measurement shown in the inset clearly indicates a single pulse in each repetition period.

The pulse spectrum at the output of the laser is shown in Fig. B.4(b). The spectral width is ~8 nm, indicating that the pulse is either heavily chirped or that it has a subpicosecond temporal duration. The average power is too low (~0.25 mW) for autocorrelation and the pulse duration at this point has not been determined (although another amplifier could be used for the autocorrelation it would impose too much dispersion for an accurate measurement). Because it was desirable for the

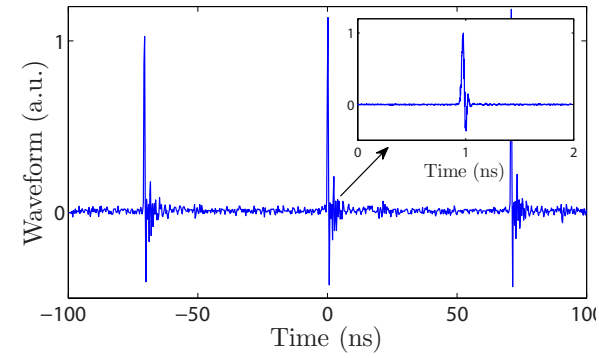

(a)

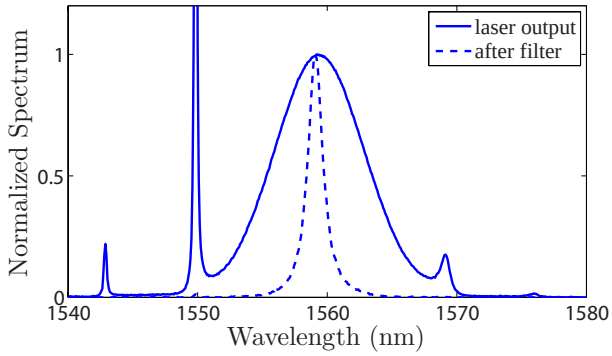

(b)

Figure B.4: The laser output after dispersion management. The sampling oscilloscope measurement in the inset of (a) shows a single pulse per round trip. (b) the laser's output spectrum (solid line), as well as the spectrum after the filter (dashed line).

experiments of chapter 4 to use high power pulses with durations > 1 ps, they were passed through a 1.3 nm bandpass filter and subsequently amplified. The spectrum of the pulses after the filter (but before the amplifier) is also shown in Fig. B.4(b).

B.2 Influence of the filter and power amplifier

The pulse spectrum and autocorrelation after the amplifier are shown in Fig. B.5. Notice that the spectrum has been modified by the amplifier. There are, presumably, two causes of this spectral modification. The first is self-phase modulation, which occurs because the high power pulses pass through ~10 m of fiber in the amplifier. The second is asymmetric spectral gain, which causes the blue side of the spectrum to be amplified more than the red at the 1560 nm wavelength.

The temporal width of the autocorrelation in Fig. B.5(b) is ~3.8 ps. If a Gaussian pulse shape is assumed this indicates a full-width-half-maximum temporal duration of 2.7 ps, which was sufficient for the experiments of chapter 4. As discussed there, the source is modeled as a train of chirped Gaussian pulses. The average power of the train is 2 mW, and the repetition period is 70 ns, indicating a pulse energy of 140 pJ. This implies a peak pulse power of ~50 W.

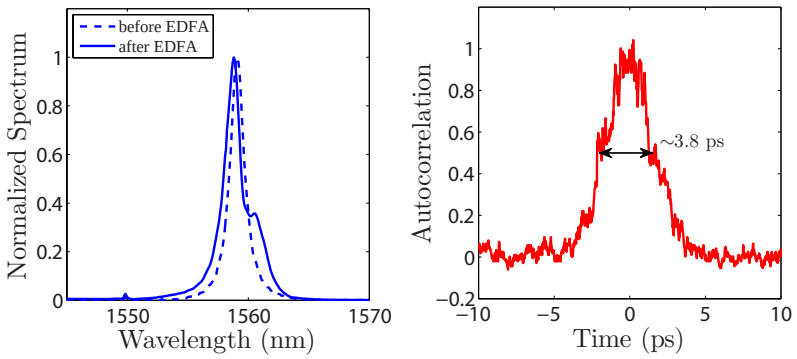

Figure B.5: Measurements of the source after the external-cavity amplifier shown in Fig. B.1. (a) the spectrum before and after the amplifier. (b) the autocorrelation at the amplifier output.

C Proof that $\hat{M}$ is Hermitian

In order to prove that $\hat{M}$ is Hermitian for the various kinds of material systems considered in chapter 5, we will make use of the following identity, which holds for any two square-integrable vector fields $\mathbf{F}$ and $\mathbf{G}$:

$$\int \mathbf{F} \cdot \nabla \times \mathbf{G}\, d^3\mathbf{r} = \int \mathbf{G} \cdot \nabla \times \mathbf{F}\, d^3\mathbf{r}. \tag{C.1}$$

Equation (C.1) can be derived from the product rule $\nabla \cdot (\mathbf{F} \times \mathbf{G}) = \mathbf{G} \cdot \nabla \times \mathbf{F} - \mathbf{F} \cdot \nabla \times \mathbf{G}$ and Stoke's theorem.

C.1 Isotropic media

In the case of isotropic media $\hat{M}$ is given by Eq. (5.5) and the inner product by Eq. (5.7). Using these two definitions and Eq. (C.1) we find

$$\begin{aligned}
\left\langle \psi_a \middle| \hat{M} \middle| \psi_b \right\rangle &= \frac{1}{4} \int \epsilon(\mathbf{r}) \sqrt{\epsilon_0} \mathbf{E}_a^* \cdot \left(i \frac{c}{\epsilon} \sqrt{\mu_0} \nabla \times \mathbf{H}_b \right) \\
&\qquad + \sqrt{\mu_0} \mathbf{H}_a^* \cdot \left(-ic \sqrt{\epsilon_0} \nabla \times \mathbf{E}_b \right) d^3\mathbf{r} \\
&= \frac{1}{4} \int i \mathbf{E}_a^* \cdot \nabla \times \mathbf{H}_b - i \mathbf{H}_a^* \cdot \nabla \times \mathbf{E}_b \, d^3\mathbf{r} \\
&= \frac{1}{4} \int i \mathbf{H}_b \cdot \nabla \times \mathbf{E}_a^* - i \mathbf{E}_b \cdot \nabla \times \mathbf{H}_a^* \, d^3\mathbf{r} \\
&= \left[\frac{1}{4} \int i \mathbf{E}_b^* \cdot \nabla \times \mathbf{H}_a - i \mathbf{H}_b^* \cdot \nabla \times \mathbf{E}_a \, d^3\mathbf{r} \right]^* \\
&= \left\langle \psi_b \middle| \hat{M} \middle| \psi_a \right\rangle^*,
\end{aligned} \tag{C.2}$$

establishing the Hermiticity of $\hat{M}$ for isotropic media.

C.2 Anisotropic and/or magnetic media

For anisotropic and/or magnetic media the proof is very similar. In this case the operator $\hat{M}$ is given by Eq. (5.32) and the inner product is defined by Eq. (5.33), leading to

$$\begin{aligned}
\left\langle \psi_a \middle| \hat{M} \middle| \psi_b \right\rangle &= \frac{1}{4} \int \sqrt{\epsilon_0} \mathbf{E}_a^* \cdot \overleftrightarrow{\boldsymbol{\epsilon}} \left(ic\sqrt{\mu_0} \overleftrightarrow{\boldsymbol{\epsilon}}^{-1} \nabla \times \mathbf{H}_b \right) \\
&\qquad + \sqrt{\mu_0} \mathbf{H}_a^* \cdot \overleftrightarrow{\boldsymbol{\mu}} \left(-ic\sqrt{\epsilon_0} \overleftrightarrow{\boldsymbol{\mu}}^{-1} \nabla \times \mathbf{E}_b \right) d^3\mathbf{r} \\
&= \frac{1}{4} \int i\mathbf{E}_a^* \cdot \nabla \times \mathbf{H}_b - i\mathbf{H}_a^* \cdot \nabla \times \mathbf{E}_b \, d^3\mathbf{r} \\
&= \frac{1}{4} \int i\mathbf{H}_b \cdot \nabla \times \mathbf{E}_a^* - i\mathbf{E}_b \cdot \nabla \times \mathbf{H}_a^* \, d^3\mathbf{r} \\
&= \left[\frac{1}{4} \int i\mathbf{E}_b^* \cdot \nabla \times \mathbf{H}_a - i\mathbf{H}_b^* \cdot \nabla \times \mathbf{E}_a \, d^3\mathbf{r} \right]^* \\
&= \left\langle \psi_b \middle| \hat{M} \middle| \psi_a \right\rangle^* , \qquad \text{(C.3)}
\end{aligned}$$

which establishes the Hermiticity of $\hat{M}$ for anisotropic and/or magnetic media.

D Incorporation of resonator loss and coupling to an input field

This appendix presents a phenomenological derivation of the terms in the mode-amplitude Eq. (5.15) that describe resonator loss and coupling to an external input field. These have been incorporated before on intuitive heuristic grounds [125]. The aim here is to support that intuition with a mathematical framework. We will derive an equation describing the mode dynamics in the absence of the perturbative term, but in the presence of losses and coupling to an input field. Their influence on the time development of the mode's amplitude is combined with the influence of the perturbation in Eq. (5.14) to yield Eq. (5.15).

First, it will be useful to define a slowly-varying mode amplitude A_k in the following way:

$$a_k(t) = \sqrt{\tau_r} A_k(t) e^{-i\omega_0 t}. \tag{D.1}$$

With this definition $|A_k|^2$ is the optical power of mode k at some location inside the cavity. It will also be useful to define a slowly-varying amplitude for the input field A'_{in} by the relation

$$A_{in}(t) = A'_{in}(t) e^{-i\omega_0 t}, \tag{D.2}$$

where ω_0 is the carrier frequency of the optical field, which can be detuned from the mode's resonance frequency by an amount $\Delta\omega = \omega_0 - \omega_k$. Consideration of how the amplitude changes during a round trip through the cavity leads to the following equation:

$$A_k(t) = \sqrt{\eta_k} A_k(t - \tau_r) e^{i\Delta\omega\tau_r} + \sqrt{T_k} A'_{in}(t). \tag{D.3}$$

Here η_k is the fraction of power remaining after the round trip. We will assume that the mode has undergone only minor changes after a single round trip and make the approximation

$$\frac{dA_k}{dt} \approx \frac{A_k(t) - A_k(t-\tau_r)}{\tau_r}. \tag{D.4}$$

Using this expression in Eq. (D.3) leads to

$$\frac{dA_k}{dt} = -\frac{1}{\tau_r\sqrt{\eta_k}}\left(e^{-i\Delta\omega\tau_r} - \sqrt{\eta_k}\right)A_k + \frac{\sqrt{T_k}}{\tau_r\sqrt{\eta_k}}A'_{in}e^{-i\Delta\omega\tau_r}. \tag{D.5}$$

Making the approximations $|\Delta\omega\tau_r| \ll 1$ and $\eta_k \approx 1$, and using identities (D.1) and (D.2) reduces Eq. (D.5) to

$$\frac{da_k}{dt} = -i\omega_k a_k - \frac{1}{2\tau_{ph}^k}a_k + \kappa_k A_{in}, \tag{D.6}$$

where $\kappa_k = \sqrt{T_k/\tau_r}$ and $1/\tau_{ph}^k = (1-\eta_k)/\tau_r$. Equation (D.6) is equivalent to Eq. (5.15) in the absence of the perturbative term, completing the proof.

We can also derive Eqs. (5.20) and (5.21) from these considerations. Note that, under the assumption of two output fields as clarified in section 5.1.3, there are three distinct contributions to resonator loss. As a result, $\eta_k = \eta_k^i\eta_k^r\eta_k^t$, where $1-\eta_k^i$ is the fraction of power lost to absorption and scattering in a round trip, and η_k^r and η_k^t are the reflectivities of the two output couplers. Assuming that all of the η parameters are close to 1, a first order Taylor expansion can be taken of $1/\tau_{ph}^k$,

$$\frac{1}{\tau_{ph}^k} = \frac{1}{\tau_{ph}^{k,i}} + \frac{1}{\tau_{ph}^{k,r}} + \frac{1}{\tau_{ph}^{k,t}}, \tag{D.7}$$

which is Eq. (5.20). Here $1/\tau_{ph}^{k,i} = (1-\eta_k^i)/\tau_r$ and likewise for $\tau_{ph}^{k,r}$ and $\tau_{ph}^{k,t}$. Note that because $\eta_k^r + T_k = 1$ as a result of energy conservation (and similarly for the transmission coupler),

$$1/\tau_{ph}^{k,r} = T_k/\tau_r, \tag{D.8}$$

$$1/\tau_{ph}^{k,t} = T_k^t/\tau_r, \tag{D.9}$$

which implies that $\kappa_k = \left(\tau_{ph}^{k,r}\right)^{-1/2}$, Eq. (5.21).

E Steady-state solutions of the symmetrically-biased two-input Kerr resonator

In this appendix the analysis of Kaplan and Meystre in Ref. [146] that clarified the stable steady-state solutions of the two-input Kerr resonator is reproduced within the theoretical framework of chapter 7. The insights drawn from this analysis lead to an understanding of the appropriate biasing regimes for the flip-flop device and form the foundation of the conclusions drawn in Fig. 7.2.

As discussed in section 7.2.2 symmetric biasing conditions are ideal. Symmetric biasing means that

$$\Delta\omega_1 = \Delta\omega_2 = \Delta\omega_0, \tag{E.1}$$

and

$$P_1 = P_2 = P_0. \tag{E.2}$$

Before applying these two equations to Eqs. (7.12) it will be useful to introduce normalized units in the following way:

$$\Delta = \Delta\omega_0\tau_{ph}, \tag{E.3}$$

$$V_k = \tau_{ph}\gamma E_k, \tag{E.4}$$

$$G = 4|\kappa|^2\tau_{ph}^3\gamma P_0. \tag{E.5}$$

Each of these definitions has physical significance. The normalized detuning, Δ, is the number of cavity linewidths that the input beams are detuned from the low-intensity resonance frequencies of the cavity. The normalized mode energy, V_k, is the

number of cavity linewidths that the mode detunes itself via the Kerr effect. Finally, G is the maximum value that either of the V_k can become when they are resonant with the cavity. In other words, G is the maximum number of linewidths that either input beam can shift the resonance frequency of the mode to which it is coupled if it maximally excites that mode.

With these definitions, Eqs. (7.12) become

$$G/4 = \left[(\Delta + V_k + 2V_{3-k})^2 + 1/4\right] V_k. \tag{E.6}$$

Following the analysis of Ref. [146], the sum, difference, and product of the mode energies are introduced:

$$S = V_1 + V_2, \tag{E.7}$$

$$D = V_1 - V_2, \tag{E.8}$$

$$T = V_1 V_2. \tag{E.9}$$

Equations (E.6) can then be rewritten as

$$G/4 = \left[(S + \Delta)^2 + 1/4\right] V_1 + 2T\,(S + \Delta) + TV_2, \tag{E.10}$$

$$G/4 = \left[(S + \Delta)^2 + 1/4\right] V_2 + 2T\,(S + \Delta) + TV_1. \tag{E.11}$$

Subtracting Eq. (E.11) from Eq. (E.10) leads to

$$\left[(S + \Delta)^2 + 1/4\right] D - TD = 0. \tag{E.12}$$

This last equation implies that

$$\Rightarrow \qquad D = 0 \qquad \text{or} \qquad T = (S + \Delta)^2 + 1/4. \tag{E.13}$$

This conclusion allows the steady-state solutions to be divided into two categories. The first category contains all of the solutions for which $D = 0$ so that the two mode energies are equal. These will be referred to as the *symmetric solutions*. The second category contains all of the solutions for which $D \neq 0$, which will be referred to as the *asymmetric solutions*.

Symmetric solutions

The symmetric solutions can be found numerically by using the definition $V_1 = V_2 = V$ in Eq. (E.6),

$$G/4 = \left[(\Delta + 3V)^2 + 1/4\right] V. \tag{E.14}$$

In order to find solutions of this equation Δ is fixed at a given value and G is then calculated for a particular value of V.

Asymmetric solutions

The asymmetric solutions are slightly more complicated to find. Note that the second condition in Eq. (E.13) must be true of them. Using this condition in Eq. (E.6) yields

$$G/4 = T\left(3S + 2\Delta\right), \tag{E.15}$$

which by applying the condition a second time can also be written

$$G/4 = \left[(S + \Delta)^2 + 1/4\right]\left(3S + 2\Delta\right). \tag{E.16}$$

The method for finding the asymmetric solutions then proceeds as follows: first G is found for a given S in Eq. (E.16) and a fixed value of Δ. Then, T is found for that set of values of S, G, and Δ using Eq. (E.15). Finally, using Eqs. (E.7) and (E.9) the solutions for V_1 and V_2 are found to be given by

$$V_1 = S/2 \pm \sqrt{(S/2)^2 - T}, \tag{E.17}$$

$$V_2 = S/2 \mp \sqrt{(S/2)^2 - T}. \tag{E.18}$$

As expected, the solutions come in pairs since the roles of modes 1 and 2 can always be reversed under symmetric biasing conditions.

Figure (E.1) plots both the symmetric and asymmetric solutions versus G for various values of the detuning Δ. When $\Delta = -0.5$ there is only a single symmetric solution that increases monotonically with the input power. When $\Delta = -1$, however, this situation changes. A region of bias powers opens up where the symmetric solution becomes unstable and in its place a single pair of stable asymmetric solutions exist. When $\Delta = -2$ this region where the asymmetric solutions exist becomes much larger

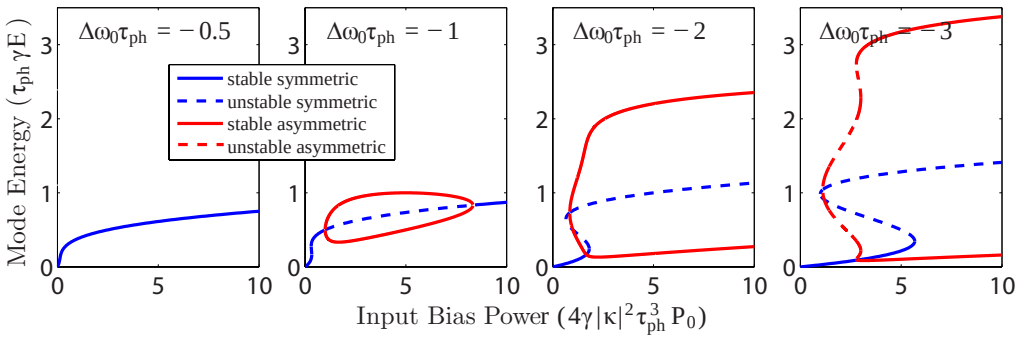

Figure E.1: Symmetric and asymmetric mode-energy solutions versus bias power for different values of detuning. Stable and unstable solutions are denoted by solid and dashed curves, respectively.

(it extends beyond the values of G plotted there) and the symmetric solution begins to exhibit hysteresis. This hysteresis becomes much more pronounced for $\Delta = -3$, where it extends more deeply into the region where a pair of asymmetric solutions exist. Interestingly, the bottom branch of the symmetric solution remains stable, even where it extends into the region where asymmetric solutions exist.

Biasing regimes

What values of detuning and input power will appropriately bias the device? Clearly, in order to obtain the kind of bistability depicted in Fig. 7.1(c) the device should be biased in a region where a pair of asymmetric solutions exist. Moreover, the device should be biased where the only stable solutions are a single pair of asymmetric ones. Otherwise, the device may slip into other operating regimes and fail. An example of a desirable biasing regime is given by the $\Delta = -1$ case of Fig. E.1 for values of G between ~1 to ~8. For the $\Delta = -3$ case, however, it is only values of $G \gtrsim 6$ that are valid for biasing, since for values less than that there exists an undesirable stable symmetric solution.

Therefore, the appropriate set of bias points in the (Δ,G) plane is the set for which two simultaneous conditions hold: 1) a single pair of stable asymmetric solutions exist, and 2) there are no stable symmetric ones. From considerations about Fig. E.1 we can induce that condition 2) is equivalent to requiring that the symmetric solutions

not exhibit hysteresis. The two sets of bias points that satisfy conditions 1) or 2) were derived analytically by Kaplan and Meystre [146]. Curves bounding the region in the (Δ,G) plane where asymmetric solutions exist can be found by finding the intersection of the symmetric and asymmetric branches. This is done by setting $V_1 = V_2 = V$ in Eq. (E.15) for the asymmetric solutions so that $T = V^2$ and $S = 2V$, and then subtracting it from Eq. (E.14). After considerable algebra one can then derive the result of Kaplan and Meystre [146],

$$G/4 = \frac{2}{3}\left[-\Delta\left(3\Delta^2 - 5/4\right) \pm \left(3\Delta^2 - 1/4\right)\sqrt{\Delta^2 - 3/4}\right]. \tag{E.19}$$

Region 2) is derived by noting that the boundaries of the hysteretic region of the symmetric solution satisfy $dG/dV = 0$. After applying this condition to Eq. (E.14) it can be shown after considerable algebra that the curves bounding this region are given by

$$G/4 = \frac{2}{81}\left[-\Delta\left(\Delta^2 + 9/4\right) \pm \left(\Delta^2 - 3/4\right)^{3/2}\right], \tag{E.20}$$

which is another result from Kaplan and Meystre [146]. The curves defined by Eqs. (E.19) and (E.20) are plotted in Fig. 7.2. It should be noted that biasing points in the region defined by Eq. (E.19) do not necessarily have only a single pair of asymmetric solutions, and hence this region does not define but only contains region 1). However, a third equation defining regions where multiple asymmetric solutions exist (such as can be seen in the last case of Fig. E.1) was also found in Ref. [146] and shows that region to be completely contained within 2). These points therefore have no overlap with the purple shaded region in Fig. 7.2 and do not affect the conclusion that this is indeed the appropriate biasing regime.

Bibliography

[1] "photonics," *Oxford English Dictionary*, 3rd ed. 2006.

[2] K. C. Kao and G. A. Hockham, "Dielectric-fibre surface waveguides for optical frequencies," Proc. IEE **113**, 1151-1158 (1966).

[3] F. P. Kapron, D. B. Keck, and R. D. Maurer, "Radiation losses in glass optical waveguides," Appl. Phys. Lett. **17**, 423-425 (1970).

[4] International Telecommunication Union, "The world in 2011: ICT facts and figures," (2011).

[5] R. H. Stolen, E. P. Ippen, and A. R. Tynes, "Raman oscillation in glass optical waveguide," Appl. Phys. Lett. **20**, 62-64 (1972).

[6] E. P. Ippen and R. H. Stolen, "Stimulated Brillouin scattering in optical fibers," Appl. Phys. Lett. **21**, 539-541 (1972).

[7] R. H. Stolen, J. E. Bjorkholm, and A. Ashkin, "Phase-matched three-wave mixing in silica fiber optical waveguides," Appl. Phys. Lett. **24**, 308-310 (1973).

[8] R. H. Stolen and C. Lin, "Self-phase-modulation in silica optical fibers," Phys. Rev. A **17**, 1448-1453 (1978).

[9] L. F. Mollenauer, R. H. Stolen, and J. P. Gordon, "Experimental observation of picosecond pulse narrowing and solitons in optical fibers," Phys. Rev. Lett. **45**, 1095-1098 (1980).

[10] G. P. Agrawal, *Applications of Nonlinear Fiber Optics*, 2nd ed. (Academic, 2008).

[11] S. E. Miller, "Integrated optics: an introduction," Bell Syst. Tech. J. **48**, 2059-2069 (1969).

[12] R. Nagarajan, M. Kato, J. Pleumeekers, P. Evans, S. Corzine, S. Hurtt, A. Dentai, S. Murthy, M. Missey, R. Muthiah, R. A. Salvatore, C. Joyner, R. Schneider, Jr., M. Ziari, F. Kish, and D. Welch, "InP photonic integrated circuits," IEEE J. Sel. Top. Quantum Electron. **16**, 1113-1125 (2010).

[13] C. R. Doerr and K. Okamoto, "Advances in silica planar lightwave circuits," J. Lightwave Technol. **24**, 4763-4789 (2006).

[14] R. A. Soref and J. P. Lorenzo, "Single-crystal silicon: a new material for 1.3 and 1.6 μm integrated-optical components" Electron. Lett. **21**, 953-954 (1985).

[15] R. A. Soref and J. P. Lorenzo, "All-silicon active and passive guided-wave components for λ = 1.3 and 1.6 μm," IEEE J. Quantum Electron. **22**, 873-879 (1986).

[16] A. Liu, L. Liao, Y. Chetrit, J. Basak, H. Nguyen, D. Rubin, and M. Paniccia, "Wavelength division multiplexing based photonic integrated circuits on silicon-on-insulator platform," IEEE J. Sel. Top. Quantum Electron. **16**, 23-32 (2010).

[17] S. Assefa, F. Xia, W. M. J. Green, C. L. Schow, A. V. Rylyakov, and Y. A. Vlasov, "CMOS-integrated optical receivers for on-chip interconnects," IEEE J. Sel. Top. Quantum Electron. **16**, 1376-1385 (2010).

[18] R. L. Espinola, J. I. Dadap, R. M. Osgood Jr., S. J. McNab, and Y. A. Vlasov, "Raman amplification in ultrasmall silicon-on-insulator wire waveguides," Opt. Express **12**, 3713-3718 (2004).

[19] H. K. Tsang, C. S. Wong, T. K. Liang, I. E. Day, S. W. Roberts, A. Harpin, J. Drake, and M. Asghari, "Optical dispersion, two-photon absorption and self-phase modulation in silicon waveguides at 1.5 μm wavelength," Appl. Phys. Lett. **80**, 416-418 (2002).

[20] R. Claps, D. Dimitropoulos, V. Raghunathan, Y. Han, and B. Jalali, "Observation of stimulated Raman amplification in silicon waveguides," Opt. Express **11**, 1731-1739 (2003).

[21] O. Boyraz and B. Jalali, "Demonstration of a silicon Raman laser," Opt. Express **12**, 5269-5273 (2004).

[22] H. Fukuda, K. Yamada, T. Shoji, M. Takahashi, T. Tsuchizawa, T. Watanabe, J. Takahashi, and S. Itabashi, "Four-wave mixing in silicon wire waveguides," Opt. Express **13**, 4629-4637 (2005).

[23] Q. Lin, O. J. Painter, and G. P. Agrawal, "Nonlinear optical phenomena in silicon waveguides: modeling and applications," Opt. Express **15**, 16604-16644 (2007).

[24] R. M. Osgood, Jr., N. C. Panoiu, J. I. Dadap, X. Liu, X. Chen, I. Hsieh, E. Dulkeith, W. M. J. Green, and Y. A. Vlasov, "Engineering nonlinearities in nanoscale optical systems: physics and applications in dispersion-engineered silicon nanophotonic wires," Adv. Opt. Photon. **1**, 162-235 (2009).

[25] T. W. Baehr-Jones and M. J. Hochberg, "Polymer silicon hybrid systems: a platform for practical nonlinear optics," J. Phys. Chem. C **112**, 8085-8090 (2008).

[26] D. T. H. Tan, K. Ikeda, P. C. Sun, and Y. Fainman, "Group velocity dispersion and self phase modulation in silicon nitride waveguides," Appl. Phys. Lett. **96**, 061101 (2010).

[27] J. S. Levy, M. A. Foster, A. L. Gaeta, and M. Lipson, "Harmonic generation in silicon nitride ring resonators," Opt. Express **19**, 11415-11421 (2011).

[28] Y. Okawachi, K. Saha, J. S. Levy, Y. H. Wen, M. Lipson, and A. L. Gaeta, "Octave-spanning frequency comb generation in a silicon nitride chip," Opt. Lett. **36**, 3398-3400 (2011).

[29] G. P. Agrawal, *Nonlinear Fiber Optics*, 4th ed. (Academic, 2007).

[30] H. Kogelnik, "Theory of dielectric waveguides," in *Integrated Optics*, T. Tamir ed. (Springer-Verlag, 1975), pp. 13-81.

[31] G. P. Agrawal, *Lightwave Technology: Components and Devices* (Wiley, 2004).

[32] M. J. Weber, *Handbook of Optical Materials* (CRC, 2003).

[33] A. M. Pérez, C. Santiago, and F. R. C. Zuñiga, "Optical properties of amorphous hydrogenated silicon nitride thin films," Opt. Eng. **45**, 123802 (2006).

[34] F. Fiedler and A. Schlachetzki, "Optical parameters of InP-based waveguides," Solid State Electron. **30**, 73-83 (1986).

[35] A. W. Snyder, "Coupled-mode theory for optical fibers," J. Opt. Soc. Am. **62**, 1267-1277 (1972).

[36] D. Dimitropoulos, B. Houshmand, R. Claps, and B. Jalali, "Coupled-mode theory of the Raman effect in silicon-on-insulator waveguides," Opt. Lett. **28**, 1954-1956 (2003).

[37] X. Chen, N. C. Panoiu, and R. M. Osgood, Jr., "Theory of Raman-mediated pulsed amplification in silicon-wire waveguides," IEEE J. Quantum Electron. **42**, 160-170 (2006).

[38] E. Dulkeith, Y. A. Vlasov, X. Chen, N. C. Panoiu, and R. M. Osgood, Jr., "Self-phase-modulation in submicron silicon-on-insulator photonic wires," Opt. Express **14**, 5524-5534 (2006).

[39] I. Hsieh, X. Chen, J. I. Dadap, N. C. Panoiu, R. M. Osgood, Jr., S. J. McNab, and Y. A. Vlasov "Cross-phase modulation-induced spectral and temporal effects on co-propagating femtosecond pulses in silicon photonic wires," Opt. Express **15**, 1135-1146 (2007).

[40] J. B. Driscoll, X. Liu, S. Yasseri, I. Hsieh, J. I. Dadap, and R. M. Osgood, Jr., "Large longitudinal electric fields (E_z) in silicon nanowire waveguides," Opt. Express **17**, 2797-2804 (2009).

[41] S. Afshar V. and T. M. Monro, "A full vectorial model for pulse propagation in emerging waveguides with subwavelength structures part I: Kerr nonlinearity," Opt. Express **17**, 2298-2318 (2009).

[42] M. D. Turner, T. M. Monro, and S. Afshar V., "A full vectorial model for pulse propagation in emerging waveguides with subwavelength structures part II: stimulated Raman scattering," Opt. Express **17**, 11565-11581 (2009).

[43] S. Afshar V., W. Q. Zhang, H. Ebendorff-Heidepriem, and T. M. Monro, "Small core optical waveguides are more nonlinear than expected: experimental confirmation," Opt. Lett. **34**, 3577-3579 (2009).

[44] M. Notomi, "Manipulating light with strongly modulated photonic crystals," Rep. Prog. Phys. **73**, 096501 (2010).

[45] H. Lee and G. P. Agrawal, "Nonlinear switching of optical pulses in fiber Bragg gratings," IEEE J. Quantum Electron. **39**, 508-515 (2003).

[46] T. Kamalakis and T. Sphicopoulos, "A new formulation of coupled propagation equations in periodic nanophotonic waveguides for the treatment of Kerr-induced nonlinearities," IEEE J. Quantum Electron. **43**, 923-933 (2007).

[47] N. C. Panoiu, J. F. McMillan, and C. W. Wong, "Theoretical analysis of pulse dynamics in silicon photonic crystal wire waveguides," IEEE J. Sel. Topics Quantum Electron. **16**, 257-266 (2010).

[48] K. Srinivasan, P. E. Barclay, M. Borselli, and O. Painter, "Optical-fiber-based measurement of an ultrasmall volume high-Q photonic crystal microcavity," Phys. Rev. B **70**, 081306 (2004).

[49] J. C. Slater, *Microwave Electronics*, (D. Van Nostrand Company, 1950).

[50] V. N. Lugovoĭ, "Stimulated Raman emission in an optical resonator," Sov. Phys. JETP **29**, 374-378 (1969).

[51] V. N. Lugovoĭ, "On the theory of a non-linear optical resonator," Optica Acta **24**, 743-756 (1977).

[52] A. Yariv and S. Kwong, "Theory of laser oscillation in resonators with photorefractive gain," Opt. Lett. **10**, 454-456 (1985).

[53] Q. Lin, T. J. Johnson, R. Perahia, C. P. Michael, and O. J. Painter, "A proposal for highly tunable optical parametric oscillation in silicon micro-resonators," Opt. Express **16**, 10596-10610 (2007).

[54] Q. Lin, T. J. Johnson, C. P. Michael, and O. Painter, "Adiabatic self-tuning in a silicon microdisk optical resonator," Opt. Express **16**, 14801-14811 (2008).

[55] T. J. Johnson, "Silicon microdisk resonators for nonlinear optics and dynamics," Ph.D. dissertation (California Institute of Technology, 2009).

[56] J. C. Maxwell, "A dynamical theory of the electromagnetic field," Philosophical Transactions of the Royal Society of London (1865).

[57] J. C. Maxwell, "On physical lines of force," Philosophical Magazine (1861).

[58] J. D. Jackson, *Classical Electrodynamics* (Wiley, 1999).

[59] R. A. Sammut, "Orthogonality and normalization of radiation modes in dielectric waveguides," J. Opt. Soc. Am. **72**, 1335-1337 (1982).

[60] A. D. Bresler, G. H. Joshi, and N Marcuvitz, "Orthogonality properties for modes in passive and active uniform wave guides," J. Appl. Phys **29**, 794-799 (1958).

[61] S. G. Johnson, M. Ibanescu, M. Skorobogatiy, O. Weisberg, T. D. Engeness, M. Soljačić, S. A. Jacobs, J. D. Joannopoulos, and Y. Fink, "Low-loss asymptotically single-mode propagation in large-core OmniGuide fibers," Opt. Express **9**, 748-779 (2001).

[62] M. Skorobogatiy, M. Ibanescu, S. G. Johnson, O. Weisberg, T. D. Engeness, M. Soljačić, S. A. Jacobs, and Y. Fink, "Analysis of general geometric scaling perturbations in a transmitting waveguide: fundamental connection between polarization-mode dispersion and group-velocity dispersion," J. Opt. Soc. Am. B **19**, 2867-2875 (2002).

[63] S. G. Johnson, P. Bienstman, M. A. Skorobogatiy, M. Ibanescu, E. Lidorikis, and J. D. Joannopoulos, "Adiabatic theorem and continuous coupled-mode the-

ory for efficient taper transitions in photonic crystals," Phys. Rev. E **66**, 066608 (2002).

[64] M. Skorobogatiy, S. G. Johnson, S. A. Jacobs, and Y. Fink, "Dielectric profile variations in high-index-contrast waveguides, coupled mode theory, and perturbation expansions," Phys. Rev. E **67**, 046613 (2003).

[65] P. N. Butcher and D. Cotter, *The Elements of Nonlinear Optics* (Cambridge, 1998).

[66] M. Born and E. Wolf, *Principles of Optics*, 7th ed. (Cambridge, 1999).

[67] C. Vassallo, "Orthogonality and normalization of radiation modes in dielectric waveguides: an alternative derivation," J. Opt. Soc. Am. **73**, 680-683 (1983).

[68] A. W. Snyder and J. D. Love, *Optical Waveguide Theory* (Kluwer Academic, 2000).

[69] P. S. Pershan, "Magneto-optical effects," J. Appl. Phys. **33**, 1482-1490 (1967).

[70] A. Yariv and P. Yeh, *Optical Waves in Crystals* (Wiley, 1984).

[71] C. Enkrich, M. Wegener, S. Linden, S. Burger, L. Zschiedrich, F. Schmidt, J. F. Zhou, Th. Koschny, and C. M. Soukoulis, "Magnetic metamaterials at telecommunication and visible frequencies," Phys. Rev. Lett. **95**, 203901 (2005).

[72] W. Cai, U. K. Chettiar, H. Yuan, V. C. de Silva, A. V. Kildishev, V. P. Drachev, and V. M. Shalaev, "Metamagnetics with rainbow colors," Opt. Express **15**, 3333-3341 (2007).

[73] S. C. Rand, W. M. Fisher, and S. L. Oliveira, "Optically induced magnetization in homogeneous, undoped dielectric media," J. Opt. Soc. Am. B **25**, 1106-1117 (2008).

[74] J. D. Joannopoulos, S. G. Johnson, J. N. Winn, and R. D. Meade, *Photonic Crystals: Molding the Flow of Light* (Princeton University Press, 2008).

[75] D. Michaelis, U. Peschel, C. Wächter, and A. Bräuer, "Reciprocity theorem and perturbation theory for photonic crystal waveguides," Phys. Rev. E **68**, 065601 (2003).

[76] G. W. Rieger, K. S. Virk, and J. F. Young, "Nonlinear propagation of ultrafast 1.5 μm pulses in high-index-contrast silicon-on-insulator waveguides," Appl. Phys. Lett. **84**, 900-902 (2004).

[77] O. Boyraz, T. Indukuri, and B. Jalali, "Self-phase-modulation induced spectral broadening in silicon waveguides," Opt. Express **12**, 829-834 (2004).

[78] A. R. Cowan, G. W. Rieger, and J. F. Young, "Nonlinear transmission of 1.5 μm pulses through single-mode silicon-on-insulator waveguide structures," Opt. Express **12**, 1611-1621 (2004).

[79] H. Yamada, M. Shirane, T. Chu, H. Yokoyama, S. Ishida, and Y. Arakawa, "Nonlinear-optic silicon-nanowire waveguides," Jpn. J. Appl. Phys. **44**, 6541-6545 (2005).

[80] E. Dulkeith, Y. A. Vlasov, X. Chen, N. C. Panoiu, and R. M. Osgood, Jr., "Self-phase-modulation in submicron silicon-on-insulator photonic wires," Opt. Express **14**, 5524-5534 (2006).

[81] I. Hsieh, X. Chen, J. I. Dadap, N. C. Panoiu, R. M. Osgood, Jr., S. J. McNab, and Y. A. Vlasov, "Ultrafast-pulse self-phase modulation and third-order dispersion in Si photonic wire-waveguides," Opt. Express **14**, 12380-12387 (2006).

[82] L. Yin and G. P. Agrawal, "Impact of two-photon absorption on self-phase modulation in silicon waveguides," Opt. Lett. **32**, 2031-2033 (2007).

[83] N. Matsuda, Y. Mitsumori, H. Kosaka, A. Sato, H. Yokoyama, K. Yamada, T. Watanabe, T. Tsuchizawa, H. Fukuda, S. Itabashi, and K. Edamatsu, "All-optical phase modulations in a silicon wire waveguide at ultralow light levels," Appl. Phys. Lett. **95**, 171110 (2009).

[84] B. A. Daniel and G. P. Agrawal, "Vectorial nonlinear propagation in silicon nanowire waveguides: polarization effects," J. Opt. Soc. Am. B **27**, 956-965 (2010).

[85] B. A. Daniel, J. Y. Lee, P. M. Fauchet, and G. P. Agrawal, "Observation of spectral and temporal polarization oscillations of optical pulses in a silicon nanowaveguide," Appl. Phys. Lett. **99**, 201104 (2011).

[86] J. Zhang, Q. Lin, G. Piredda, R. W. Boyd, G. P. Agrawal, and P. M. Fauchet, "Anisotropic nonlinear response of silicon in the near-infrared region," Appl. Phys. Lett. **91**, 071113 (2007).

[87] R. W. Boyd, *Nonlinear Optics*, 3rd ed. (Academic, 2008).

[88] M. Dinu, F. Quochi, and H. Garcia, "Third-order nonlinearities in silicon at telecom wavelengths," Appl. Phys. Lett. **82**, 2954-2956 (2003).

[89] Q. Lin, J. Zhang, G. Piredda, R. W. Boyd, P. M. Fauchet, and G. P. Agrawal, "Dispersion of silicon nonlinearities in the near infrared region," Appl. Phys. Lett. **91**, 021111 (2007).

[90] R. A. Soref and B. R. Bennett, "Electrooptical effects in silicon," IEEE J. Quantum Electron. **23**, 123-129 (2007).

[91] J. Y. Lee, L. Yin., G. P. Agrawal, and P. M. Fauchet, "Ultrafast optical switching based on nonlinear polarization rotation in silicon waveguides," Opt. Express **18**, 11514-11523 (2010).

[92] D. F. Prelewitz and T. G. Brown, "Optical limiting and free-carrier dynamics in a periodic semiconductor waveguide," J. Opt. Soc. Am. B **11**, 304-312 (1994).

[93] D. Dimitropoulos, R. Jhaveri, R. Claps, J. C. S. Woo, and B. Jalali, "Lifetime of photogenerated carriers in silicon-on-insulator rib waveguides," Appl. Phys. Lett. **86**, 071115 (2005).

[94] M. Rosling, H. Bleichner, P. Jonsson, and E. Nordlander, "The ambipolar diffusion coefficient in silicon: dependence on excess carrier concentration and temperature," J. Appl. Phys. **76**, 2855-2859 (1994).

[95] P. Yeh, "Electromagnetic propagation in birefringent layered media," J. Opt. Soc. Am. **69**, 742-756 (1978).

[96] P. Lüsse, P. Stuwe, J . Schule, and H. G. Unger, "Analysis of vectorial mode fields in optical waveguides by a new finite difference method," J. Lightwave Technol. **12**, 487-494 (1994).

[97] M. A. Foster, A. C. Turner, R. Salem, M. Lipson, and A. L. Gaeta, "Broad-band continuous-wave parametric wavelength conversion in silicon nanowaveguides," Opt. Express **15**, 12949-12958 (2007).

[98] A. C. Turner-Foster, M. A. Foster, R. Salem, A. L. Gaeta, and M. Lipson, "Frequency conversion over two-thirds of an octave in silicon nanowaveguides," Opt. Express **18**, 1904-1908 (2010).

[99] L. Yin, Q. Lin, and G. P. Agrawal, "Soliton fission and supercontinuum generation in silicon waveguides," Opt. Lett. **32**, 391-393 (2007).

[100] L. Tong, J. Lou, and E. Mazur, "Single-mode guiding properties of subwavelength-diameter silica and silicon wire waveguides," Opt. Express **12**, 1025-1035 (2004).

[101] A. C. Turner, C. Manolatou, B. S. Schmidt, M. Lipson, M. A. Foster, J. E. Sharping, and A. L. Gaeta, "Tailored anomalous group-velocity dispersion in silicon channel waveguides," Opt. Express **14**, 4357-4362 (2006).

[102] E. Dulkeith, F. Xia, L. Schares, W. M. J. Green, and Y. A. Vlasov, "Group index and group velocity dispersion in silicon-on-insulator photonic wires," Opt. Express **14**, 3853-3863 (2006).

[103] L. Yin, Q. Lin, and G. P. Agrawal, "Dispersion tailoring and soliton propagation in silicon waveguides," Opt. Lett. **31**, 1295-1297 (2006).

[104] J. Jágerská, N. Le Thomas, R Houdré, J. Bolten, C. Moormann, T. Wahlbrink, J. Čtyroký, M. Waldow, and M. Först, "Dispersion properties of silicon nanophotonic waveguides investigated with Fourier optics," Opt. Lett. **32**, 2723-2725 (2007).

[105] D. Duchesne, P. Cheben, R. Morandotti, B. Lamontagne, D. Xu, S. Janz, and D. Christodoulides, "Group-index birefringence and loss measurements in silicon-on-insulator photonic wire waveguides," Opt. Eng. **46**, 104602 (2007).

[106] B. A. Daniel and G. P. Agrawal, "Dependence of dispersive and birefringence properties of silicon nanowires on waveguide dimensions," Opt. Lett. **35**, 190-192 (2010).

[107] J. Zhang, Q. Lin, G. Piredda, R. W. Boyd, G. P. Agrawal, and P. M. Fauchet, "Optical solitons in a silicon waveguide," Opt. Express **15**, 7682-7688 (2007).

[108] L. Yin, J. Zhang, P. M. Fauchet, and G. P. Agrawal, "Optical switching using nonlinear polarization rotation inside silicon waveguides," Opt. Lett. **34**, 476-478 (2009).

[109] I. D. Rukhlenko, I. L. Garanovich, M. Premaratne, A. A. Sukhorukov, G. P. Agrawal, and Y. S. Kivshar, "Polarization rotation in silicon waveguides: analytical modeling and applications," IEEE Photon. J. **2**, 423-435 (2010).

[110] C. M. Dissanayake, M. Premaratne, I. D. Rukhlenko, and G. P. Agrawal, "FDTD modeling of anisotropic nonlinear optical phenomena in silicon waveguides," Opt. Express **18**, 21427-21448 (2010).

[111] C. M. Dissanayake, I. D. Rukhlenko, M. Premaratne, and G. P. Agrawal, "Polarization-dependent spectral broadening of femtosecond pulses in silicon waveguides," J. Opt. Soc. Am. B **28**, 2383-2389 (2011).

[112] T. J. Kippenberg, S.M. Spillane, and K. J. Vahala, "Kerr-nonlinearity optical parametric oscillation in an ultrahigh-Q toroid microcavity," Phys. Rev. Lett. **93**, 083904 (2004).

[113] J. S. Levy, A. Gondarenko, M. A. Foster, A. C. Turner-Foster, A. L. Gaeta, and M. Lipson, "CMOS-compatible multiple-wavelength oscillator for on-chip optical interconnects," Nat. Photon. **4**, 37-40 (2010).

[114] L. Razzari, D. Duchesne, M. Ferrera, R. Morandotti, S. Chu, B. E. Little, and D. J. Moss, "CMOS-compatible integrated optical hyperparametric oscillator," Nat. Photon. **4**, 41-45 (2010).

[115] H. Rong, A. Liu, R. Jones, O. Cohen, D. Hak, R. Nicolaescu, A. Fang, and M. Paniccia, "An all-silicon Raman laser," Nature **433**, 292-294 (2005).

[116] H. Rong, Y. Kuo, S. Xu, A. Liu, R. Jones, and M. Paniccia, "Monolithic integrated Raman silicon laser," Opt. Express **14**, 6705-6712 (2006).

[117] H. Rong, S. Xu, O. Cohen, O. Raday, M. Lee, V. Sih, and M. Paniccia, "A cascaded silicon Raman laser," Nat. Photon. **2**, 170-174 (2008).

[118] V. R. Almeida, C. A. Barrios, R. R. Panepucci, M. Lipson, M. A. Foster, D. G. Ouzounov, and A. L. Gaeta, "All-optical switching on a silicon chip," Opt. Lett. **29**, 2867-2869 (2004).

[119] M. Waldow, T. Plötzing, M. Gottheil, M. Först, J. Bolten, T. Wahlbrink, and H. Kurz, "25ps all-optical switching in oxygen implanted silicon-on-insulator microring resonator," Opt. Express **16**, 7693-7702 (2008).

[120] K. Nozaki, T. Tanabe, A. Shinya, S. Matsuo, T. Sato, H. Taniyama, and M. Notomi, "Sub-femtojoule all-optical switching using a photonic-crystal nanocavity," Nat. Photon. **4**, 477-483 (2010).

[121] P. Dong, S. F. Preble, J. T. Robinson, S. Manipatruni, and M. Lipson, "Inducing photonic transitions between discrete modes in a silicon optical microcavity," Phys. Rev. Lett. **100**, 033904 (2008).

[122] B. A. Daniel, D. N. Maywar, and G. P. Agrawal, "Dynamic mode theory of optical resonators undergoing refractive index changes," J. Opt. Soc. Am. B **28**, 2207-2215 (2011).

[123] Y. Xu, Y. Li, R. K. Lee, and A. Yariv, "Scattering-theory analysis of waveguide-resonator coupling," Phys. Rev. E **62**, 7389-7404 (2000).

[124] P. A. M. Dirac, *The Principles of Quantum Mechanics* (Clarendon, 1992).

[125] H. A. Haus, *Waves and Fields in Optoelectronics* (Prentice-Hall, 1984).

[126] M. F. Yanik and S. Fan, "Dynamic photonic structures: stopping, storage, and time reversal of light," Stud. Appl. Math. **115**, 233-253 (2005).

[127] M. Notomi and S. Mitsugi, "Wavelength conversion via dynamic refractive index tuning of a cavity," Phys. Rev. A **73**, 051803 (2006).

[128] S. F. Preble, Q. Xu, and M. Lipson, "Changing the colour of light in a silicon resonator," Nat. Photon. **1**, 293-296 (2007).

[129] M. W. McCutcheon, A. G. Pattantyus-Abraham, G. W. Rieger, and J. F. Young, "Emission spectrum of electromagnetic energy stored in a dynamically perturbed optical microcavity," Opt. Express **15**, 11472-11480 (2007).

[130] T. Tanabe, M. Notomi, H. Taniyama, and E. Kuramochi, "Dynamic release of trapped light from an ultrahigh-Q nanocavity via adiabatic frequency tuning," Phys. Rev. Lett. **102**, 043907 (2009).

[131] T. Kampfrath, D. M. Beggs, T. P. White, A. Melloni, T. F. Krauss, and L. Kuipers, "Ultrafast adiabatic manipulation of slow light in a photonic crystal," Phys. Rev. A **81**, 043837 (2010).

[132] T. Tanabe, E. Kuramochi, H. Taniyama, and M. Notomi, "Electro-optic adiabatic wavelength shifting and Q switching demonstrated using a p-i-n integrated photonic crystal nanocavity," Opt. Lett. **35**, 3895-3897 (2010).

[133] S. F. Preble and M. Lipson, "Conversion of a signal wavelength in a dynamically tuned resonator," in *Integrated Photonics Research and Applications/Nanophotonics*, Technical Digest (CD) (Optical Society of America, 2006), paper IMC5.

[134] Z. Gaburro, M. Ghulinyan, F. Riboli, L. Pavesi, A. Recati, and I. Carusotto, "Photon energy lifter," Opt. Express **14**, 7270-7278 (2006).

[135] J. N. Winn, S. Fan, J. D. Joannopoulos, and E. P. Ippen, "Interband transitions in photonic crystals," Phys. Rev. B **59**, 1551-1554 (1999).

[136] N. Malkova, S. Kim, and V. Gopalan, "Jahn-Teller effect in two-dimensional photonic crystals," Phys. Rev. B **68**, 045105 (2003).

[137] Y. Xiao, G. P. Agrawal, and D. N. Maywar, "Spectral and temporal changes of optical pulses propagating through time-varying linear media," Opt. Lett. **36**, 505-507 (2011).

[138] Y. Xiao, D. N. Maywar, and G. P. Agrawal, "Optical pulse propagation in dynamic Fabry-Perot resonators," J. Opt. Soc. Am. B **28**, 1685-1692 (2011).

[139] B. A. Daniel, D. N. Maywar, and G. P. Agrawal, "Efficient adiabatic wavelength conversion in Gires–Tournois resonators," Opt. Lett. **36**, 4155-4157 (2011).

[140] T. P. White, L. O'Faolain, J. Li, L. C. Andreani, and T. F. Krauss, "Silica-embedded silicon photonic crystal waveguides," Opt. Express **16**, 17076-17081 (2008).

[141] V. R. Almeida and M. Lipson, "Optical bistability on a silicon chip," Opt. Lett. **29**, 2387-2389 (2004).

[142] K. Ikeda, R. E. Saperstein, N. Alic, and Y. Fainman, "Thermal and Kerr nonlinear properties of plasma-deposited silicon nitride/ silicon dioxide waveguides," Opt. Express **16**, 12987-12994 (2008).

[143] G. P. Agrawal and C. Flytzanis, "Two-photon double-beam optical bistability," Phys. Rev. Lett. **44**, 1058-1061 (1980).

[144] G. P. Agrawal, "Effect of mode coupling on optical bistability in a bidirectional ring cavity," Appl. Phys. Lett. **38**, 505-507 (1981).

[145] A. E. Kaplan and P. Meystre, "Enhancement of the Sagnac effect due to nonlinearly induced nonreciprocity," Opt. Lett. **6**, 590-592 (1981).

[146] A. E. Kaplan and P. Meystre, "Directionally asymmetrical bistability in a symmetrically pumped nonlinear ring interferometer," Opt. Commun. **40**, 229-232 (1982).

[147] M. Haelterman, P. Mandel, J. Danckaert, H. Thienpont, and I. Veretennicoff, "Two-beam nonlinear Fabry–Perot transmission characteristics," Opt. Commun. **74**, 238-244 (1989).

[148] M. Haelterman and P. Mandel, "Pitchfork bifurcation using a two-beam nonlinear Fabry–Perot interferometer: an analytical study," Opt. Lett. **15**, 1412-1414 (1990).

[149] M. Haelterman, "All-optical set-reset flip-flop operation in the nonlinear Fabry–Perot interferometer," Opt. Commun. **86**, 189-191 (1991).

[150] F. A. Hopf and P. Meystre, "Anomalous switching in dispersive optical bistability," Opt. Commun. **31**, 245-250 (1979).

[151] H. Kawashima, Y. Tanaka, N. Ikeda, Y. Sugimoto, T. Hasama, and H. Ishikawa, "Numerical study of impulsive switching of bistable states in nonlinear etalons," IEEE Photon. Technol. Lett. **19**, 913-915 (2007).

[152] S. Sandhu, M. L. Povinelli, and S. Fan, "Enhancing optical switching with coherent control," Appl. Phys. Lett. **96**, 231108 (2010).

[153] Jared F. Bauters, Martijn J. R. Heck, Demis John, Daoxin Dai, Ming-Chun Tien, Jonathon S. Barton, Arne Leinse, René G. Heideman, Daniel J. Blumenthal, and John E. Bowers, "Ultra-low-loss high-aspect-ratio Si_3N_4 waveguides," Opt. Express **19**, 3163-3174 (2011).

[154] R. Amatya, C. W. Holzwarth, H. I. Smith, R. J. Ram, "Efficient thermal tuning for second-order silicon nitride microring resonators," *Photonics in switching*, pp. 149-150, 19-22 Aug. 2007, doi: 10.1109/PS.2007.4300788

[155] *CRC Materials Science and Engineering Handbook* (CRC, 2001).

[156] *CRC Handbook of Chemistry and Physics* (CRC, 2009).

[157] C. Monat, B. Corcoran, M. Ebnali-Heidari, C. Grillet, B. J. Eggleton, T. P. White, L. OFaolain, and T. F. Krauss, "Slow light enhancement of nonlinear effects in silicon engineered photonic crystal waveguides," Opt. Express **17**, 2944-2953 (2009).

[158] J. F. McMillan, M. Yu, D. Kwong, and C. W. Wong, "Observation of four-wave mixing in slow-light silicon photonic crystal waveguides," Opt. Express **18**, 15484-15497 (2010).

[159] K. Suzuki and T. Baba, "Nonlinear light propagation in chalcogenide photonic crystal slow light waveguides," Opt. Express **18**, 26675-26685 (2010).

[160] M. Roussey, M. Bernal, N. Courjal, D. Van Labeke, F. I. Baida, and R. Salut, "Electro-optic effect exaltation on lithium niobate photonic crystals due to slow photons," Appl. Phys. Lett. **89**, 241110 (2006).

[161] D. Yeom, E. C. Mägi, M. R. E. Lamont, M. A. F. Roelens, L. Fu, and B. J. Eggleton, "Low-threshold supercontinuum generation in highly nonlinear chalcogenide nanowires," Opt. Lett. **33**, 660-662 (2008).

[162] B. Kuyken, X. Liu, R. M. Osgood Jr., R. Baets, G. Roelkens, and W. M. J. Green, "Mid-infrared to telecom-band supercontinuum generation in highly nonlinear silicon-on-insulator wire waveguides," Opt. Express **19**, 20172-20181 (2011).

[163] M. A. Foster, A. C. Turner, M. Lipson, and A. L. Gaeta, "Nonlinear optics in photonic nanowires," Opt. Express **16**, 1300-1320 (2008).